

# Fracture detection using seismic anisotropy at the Weyburn CO<sub>2</sub> storage site, Saskatchewan

Alexander Duxbury

A thesis submitted to the Faculty of Science in  
partial fulfillment of the requirements for the degree of  
Master of Science

Department of Earth Science  
Carleton University  
Ottawa, Ontario  
July, 2010

The undersigned hereby recommend to the Faculty of Science acceptance of this thesis submitted by Alexander Duxbury, in partial fulfillment of the requirements for the degree of Master of Science.

---

Dr. Claire Samson, Thesis Co-Supervisor

---

Dr. Don White, Thesis Co-Supervisor

---

Dr. Claire Samson, Chair Department of Earth Science

# Acknowledgements

I've been fortunate to have received advice and assistance from many people for this study. I'm particularly grateful for the excellent supervision of Don White and Claire Samson who provided a challenging project opportunity and ensured its success.

My thanks to Barbara Dietiker for her advice and assistance with software and for always answering unexpected drop in questions. Thanks also to Steve Hall, for his assistance with AVOA analysis and recommendations for methodology. This study benefits greatly from his expertise and input. I enjoyed my stay in Bristol and am grateful to Mike Kendall and James Wookey for providing modeling software and their insight. Modeling would not have been possible without their contribution. Thanks also to James Verdon for his help with CO<sub>2</sub> properties for modeling.

I've spent much of this project taxing the resources of the GSC which made the seismic processing and inversion portion of this study possible. I'd like to thank Gilles Bellefleur for answering many questions and for his advice on true amplitude processing. My thanks to Jun-Wei Huang for his input on uncertainty analysis. Thanks to Brian Roberts for his help with ProMAX and for dropping Don off the license server for me.

I'd like to thank Cenovus for providing the Weyburn field data and David Cooper for his insight and processing recommendations. Thanks to the PTRC for providing funding and the opportunity to present at the PRISM CCS meetings. I'd also like to thank the Ontario Graduate Scholarship, Natural Resources Canada, Society of Exploration Geophysicists, Canadian Society of Exploration Geophysicists (CSEG) and Canadian Exploration Geophysics Society for their support (KEGS).

# Abstract

Geological storage of CO<sub>2</sub> maybe an effective means of mitigating CO<sub>2</sub> emissions to the atmosphere. Cap rock integrity is an essential characteristic of any reservoir to be used for long term CO<sub>2</sub> storage. Focusing on the Midale reservoir within the Weyburn field in southeast Saskatchewan, this study aims to assess the cap rock for the presence of fractures which may provide migration pathways for CO<sub>2</sub> out of the containment interval. Seismic AVOA (amplitude variation with offset and azimuth) techniques have been applied to provide maps of seismic anisotropy at the cap rock horizon. These maps aid in identifying areas of potential fracturing; although, the source of anisotropy is non-unique and could also result from differences in the horizontal stress field, aligned mineral fabrics or faults.

Modeling is conducted to determine if the effects of anisotropy in the overburden and layers immediately above the cap rock will introduce unacceptable levels of uncertainty in AVOA analysis. Of particular interest are the effects of known underlying fracture induced anisotropy from the reservoir and whether its response can be separated from that of the overlying layers.

Seismic anisotropy analysis shows multiple isolated areas of increased anisotropy which may be fracture-related. AVOA inversion results correlate well with geomechanical modeling predictions, microseismic observations and previous fracture studies on well log and core samples from the reservoir. Anisotropy anomalies are observed to correspond with salt dissolution structures in the cap rock and overlying horizons as interpreted from 3D seismic cross sections.

# Contents

<b>CHAPTER 1. INTRODUCTION .....</b>	<b>1</b>
1.1. BACKGROUND GEOLOGY .....	2
1.1.1. <i>Reservoir and sealing units</i> .....	3
1.2. LITERATURE REVIEW .....	6
<b>CHAPTER 2. THEORY .....</b>	<b>9</b>
2.1. ELASTICITY .....	10
2.2. SYMMETRY SYSTEMS .....	13
2.2.1. <i>VTI and HTI models</i> .....	13
2.2.2. <i>Orthorhombic models</i> .....	15
2.3. WAVE PROPAGATION IN ANISOTROPIC MEDIA .....	17
2.4. FRACTURED MEDIUM MODELS .....	21
2.4.1. <i>Hudson's theory</i> .....	24
2.4.2. <i>Thomsen's parameters</i> .....	26
2.5. P-WAVE AVOA FOR VERTICAL FRACTURE SYSTEMS .....	28
2.6. UNCERTAINTY IN AVOA ANALYSIS .....	31
2.6.1. <i>Orientation ambiguity</i> .....	32
2.6.2. <i>Attenuation</i> .....	33
2.7. TRANSMISSION EFFECTS.....	34
2.7.1. <i>Geometric spreading</i> .....	35
2.7.2. <i>Multiple fracture sets</i> .....	35
<b>CHAPTER 3. METHODOLOGY .....</b>	<b>37</b>
3.1. SEISMIC DATA .....	37
3.2. ACQUISITION GEOMETRY .....	39
3.3. PROCESSING .....	42
3.4. AVOA INVERSION .....	46
3.5. UNCERTAINTY.....	49
<b>CHAPTER 4. MODELING.....</b>	<b>52</b>
4.1. GEOLOGIC MODEL.....	52
4.2. SINGLE INTERFACE MODELING.....	55
4.2.1. <i>Crack fill material</i> .....	57
4.2.2. <i>Crack density</i> .....	58
4.3. MULTI-LAYER THICKNESS AND INTERFERENCE.....	59
4.4. MODELING CONCLUSIONS.....	62
<b>CHAPTER 5. RESULTS.....</b>	<b>63</b>
5.1. WATROUS.....	63
5.2. CAP ROCK.....	68
<b>CHAPTER 6. DISCUSSION.....</b>	<b>72</b>
6.1. WATROUS ANISOTROPY .....	72
6.1.1. <i>Summary of Watrous anisotropy anomalies</i> .....	75
6.2. CAP ROCK ANISOTROPY .....	81
6.2.1. <i>Summary of cap rock anisotropy anomalies</i> .....	85
6.3. SIGNIFICANCE OF CAP ROCK ANISOTROPY .....	86
6.4. SOURCES OF ANISOTROPY .....	87
6.5. ANISOTROPY AND AN INDICATION OF FRACTURING.....	89
6.6. RECOMMENDATIONS FOR FUTURE CO <sub>2</sub> MONITORING.....	90

<b>CHAPTER 7. CONCLUSION .....</b>	<b>97</b>
<b>CHAPTER 8. REFERENCES .....</b>	<b>100</b>
<b>APPENDIX A .....</b>	<b>107</b>

## List of Figures

Figure 1.1 Weyburn Field, southeast Saskatchewan. The Phase 1A monitoring area (grey shading) is being considered for this study. Image source: modified (White, 2009). .....	3
Figure 1.2. Schematic diagram of the Weyburn-Midale reservoir and cap rock. The Midale Evaporite forms the immediate cap rock to the reservoir; however, it is similar in geophysical logs and seismic response to the overlying Ratcliffe Beds, for the purpose of this study the Midale Evaporite and Ratcliffe beds form the cap rock interval. Image source: IEA GHG Weyburn CO <sub>2</sub> monitoring and storage project summary report 2000-2004 (Whittaker, 2004). .....	6
Figure 2.1 Diagram of a medium with fracture induced anisotropy and a HTI (Horizontal Transverse Isotropy) symmetry in the $X_1$ direction. The isotropy plane is the $[X_2, X_3]$ plane parallel to the fracture surfaces. For propagation in this plane, P- and S-waves travel with velocities of the isotropic host rock. The symmetry-axis lies in the $[X_1, X_3]$ plane orthogonal to the fracture surfaces where P- and S-wave velocities are reduced due to the increased compliance of the fractures. Source, modified (Rüger, 1998). .....	15
Figure 2.2 Horizontal layered strata and parallel vertical cracks forming orthorhombic symmetry. Adapted from (Rüger, 1998). .....	16
Figure 2.3 Diagram showing the relationship between the group velocity, polarization and phase velocity. The phase velocity is constant and propagates in the direction normal to the wavefront. The group velocity is the velocity along the ray path. The particle motion, or polarization, travels at an angle between the phase velocity and group velocity. Where $\theta$ is the angle between the vertical and the phase velocity and $\psi$ is the angle between the group velocity and vertical. Image adapted from (Hall, 2000a; Tsvankin, 2001) .....	21
Figure 3.1. Fold coverage and data availability for the Weyburn-Midale Phase 1A field area. (a) Fold coverage map; fold range 1-80, average fold 45 (green). (b) Offset and azimuth distribution. The majority of azimuths are well sampled in the 500-1500m offset range with longer offsets available in the 20-80° and 200-260° azimuth ranges. ....	38
Figure 3.2. Example of offset and azimuth distribution for a sample CMP and CMP supegathers. a) Location of CMP point, CDP# 88712 b) Offset and azimuth distribution for single CMP, fold 41. c) Histogram of azimuth distribution for 3x3 supergather, 2° bins. d) Offset and azimuth distribution for 3x3 supergather. e) Histogram of azimuth distribution for 5x5 supergather, 2° bins. f) Offset and azimuth distribution for 5x5	

- supergather. The majority of  $2^\circ$  azimuth bins contain 5 traces or more in the  $5 \times 5$  supergather, whereas the  $3 \times 3$  supergather contains gaps with 5 traces or less over a  $10^\circ$  azimuth range. .... 40
- Figure 3.3. Sensitivity of the orientation of anisotropy to the field geometry. In each figure a sub-set of the field geometry from the center of the study area is used. a) A constant AVO gradient with up to  $\pm 10\%$  variation in the synthetic amplitudes produces a scatter of orientations without bias towards the acquisition geometry orientation. b) Anisotropy orientations using a constant synthetic AVOA trend oriented at  $20^\circ$  with synthetic amplitudes varying by up to  $\pm 10\%$ . .... 42
- Figure 3.4 True amplitude processing sequence applied for each horizon of interest. Horizon time picks ( $t_0$ ), NMO and stacking were performed to obtain database parameters and are omitted from the final processing sequence. .... 43
- Figure 3.5 Surface consistent source-receiver amplitude balancing. a) Mean source and receiver amplitudes pre-balancing are highly variable indicating differing ground conditions (wet vs. dry) or possible coupling issues. .... 44
- Figure 3.6 Stack comparison between, a) the provided Sensor Geophysical un-migrated image processed dataset and b) true amplitude processed dataset for this study. The isotropic NMO correction applied for stacking was not applied during amplitude analysis. Watrous horizon, blue line, cap rock horizon red line. A good match between the true amplitude processed stack and image processed stack is observed. .... 45
- Figure 3.7. Sample CMP gathers after processing showing the cap rock horizon with extracted RMS and peak amplitudes plotted above. Longer offsets ( $>1450\text{m}$ ) are often muted out due to higher levels of noise and inconsistencies in the reflection horizons. The horizon has been flattened using the equivalent time shift for a NMO correction to avoid NMO stretch. .... 46
- Figure 3.8 The methods of azimuthal sectoring, a) and b), and surface fitting, c), for AVOA. Synthetic amplitudes with up to  $10\%$  deviation in input amplitude are used for demonstration. a) The AVO gradient (red line) is calculated for each azimuth bin. b) The gradient from each azimuth bin is plotted at the bin center and the anisotropy magnitude and orientation are determined. c) A linear least squares regression of amplitudes is performed to determine the magnitude and orientation of anisotropy. .... 51
- Figure 4.1 Diagram of the 7 layer earth model used to produce synthetic AVOA response at the Watrous, cap rock and reservoir horizons. Physical properties for the layers are listed in Table 3. Note the non-linear depth scale. .... 54
- Figure 4.2 Relative magnitudes of the near-offset AVO gradient for model layers of interest. Dashed lines represent anisotropy in multiple layers, e.g the reservoir and cap rock. All cases are for crack density of 0.1 a) Watrous, brine crack fill. b) Watrous, gas fill. c) cap rock, brine fill. The red line represents anisotropy in both the Watrous and cap rock d) cap rock, gas fill. The red line represents anisotropy in both the Watrous and cap rock e) reservoir, brine fill. f) reservoir, gas fill. .... 56

Figure 4.3 Near-offset AVO gradient response for the top of the cap rock. Curves are shown for anisotropy in a given layer, cap rock (blue), Watrous (green), overburden (magenta), both cap rock and watrous layers anisotropic (red). a) Response for crack density 0.1 equivalent to the lower Vuggy reservoir. b) Response for crack density 0.03 equivalent to the upper Marly reservoir. The higher crack density is seen to produce a larger magnitude of anisotropy for all case. .... 58

Figure 4.4 Near-offset AVO gradient response at the cap rock horizon for several model layer thicknesses. Cap rock thickness varies from 10m (red), 15m (black), 20m (blue) to 30m (green). Reservoir thickness varies between 5m (dashed line) and 10m (solid lines). a) Isotropic cap rock with underlying anisotropic reservoir layers. b) Anisotropic cap rock with underlying anisotropic reservoir. c) Isotropic cap rock with underlying anisotropic reservoir, filtered to 95% correlation between amplitudes and near-offset HTI model response. d) Anisotropic cap rock with underlying anisotropic reservoir, filtered to 95% correlation between amplitudes and near-offset HTI model response. .... 61

Figure 5.1 Normalized near-offset AVOA anisotropy magnitude from amplitude inversion of the Watrous horizon. Anisotropy magnitude is low over the majority of the study area with few isolated anomalies near the peripheries. Anomalies on the peripheries are unreliable due to reduced azimuth and offset coverage. .... 65

Figure 5.2 Attribute maps from AVOA inversion for the Watrous horizon. Attribute maps aid in assessing horizon properties and stability of the inversion. Masked portions in the center of the study area and along the peripheries result from reduced azimuth and offset coverage due to infrastructure and survey geometry. .... 66

Figure 5.3 a) The percent uncertainty in the magnitude of anisotropy is obtained through a propagation of error using the standard errors of the regression coefficients. A measure of uncertainty is necessary to gain confidence when interpreting anisotropy anomalies. b) The residual anomalies after masking represent points with the highest correlation, lowest uncertainty and above average anisotropy. .... 67

Figure 5.4 Anisotropy orientation distribution for a) all points within the study area and b) the residual anisotropy anomalies after masking. Orientations in b) correspond to vectors in Figure 5.3b. .... 67

Figure 5.5 Normalized near-offset AVOA anisotropy magnitude from amplitude inversion of the cap rock horizon. Anisotropy magnitude varies from low to high over the study area. Points of low anisotropy represent a model fit to scatter in the data. Points of higher anisotropy which aren't associated with large uncertainties are of interest. .... 69

Figure 5.6 Attribute maps from AVOA inversion for the cap rock horizon. Attribute maps aid in assessing horizon properties and stability of the inversion. Masked portions in the center of the study area and along the peripheries result from reduced azimuth and offset coverage due to infrastructure and survey geometry. .... 70

Figure 5.7 a) The percent uncertainty in the magnitude of anisotropy is obtained through a propagation of error using the standard errors of the regression coefficients. A measure of uncertainty is necessary to gain confidence when interpreting anisotropy anomalies. b) Residual anomalies after masking represent points with the highest correlation, lowest uncertainty and above average anisotropy. ....	71
Figure 5.8 Anisotropy orientation distribution for a) all points within the study area regardless of uncertainty and b) the residual anisotropy anomalies after masking. Orientations in b) correspond to vectors in Figure 5.7b. ....	71
Figure 6.1. Watrous isopach thickness map. Thickness ranges from roughly 50m to 65m throughout the phase 1A area, outlined in white. Source data: true vertical depth well tops. Picks provided by PTRC Phase 1 (Whitaker, 2004). ....	76
Figure 6.2. Combined Ratcliffe and Midale Evaporite isopach thickness map. Thickness ranges from roughly 25m in the south to 8m in the north. Source data: true vertical depth well tops. Picks provided by PTRC Phase 1 (Whitaker, 2004). ....	76
Figure 6.3. Watrous horizon residual anisotropy anomalies. Anomalies are highlighted which show greater consistency in magnitude, orientation and spatial extent. Isolated anisotropy vectors are considered less reliable. Anomalies ‘C’ and ‘D’ represent valid amplitude anisotropy. ....	77
Figure 6.4. Offset and azimuth distribution for a sample point within the ‘A’ anomaly in Figure 6.3. Azimuthal coverage is consistent with the exception of the 35-80° range. Offset coverage is fairly even across all azimuths. ....	78
Figure 6.5. AVOA surface displayed in the amplitude – azimuth plane. Color shading corresponds to amplitude value. A strong azimuthal anisotropy is observed, however, this may be exaggerated due to an under-sampling of the 40-80° azimuth range. Red dots represent the AVOA surface fit to the data (blue dots) ....	78
Figure 6.6. Offset and azimuth distribution for a sample point within the ‘D’ anomaly in Figure 6.3. Azimuthal coverage is consistent with the exception of the 35-55° range. Offset coverage is fairly even across all azimuths. ....	79
Figure 6.7. AVOA surface displayed in the amplitude – azimuth plane. Color shading corresponds to amplitude value. A strong azimuthal anisotropy is observed. Red dots represent the AVOA surface fit to the data (blue dots). ....	79
Figure 6.8. Stack image with arrows denoting the location of anomalies ‘C’ (right) and ‘D’ (left), Figure 6.3 and Figure 6.9. Slight dome features are observed in the Watrous and Lower Gravelbourg horizons. These structures result from salt dissolution below the reservoir. A high magnitude of anisotropy with north west orientation corresponds to these features. Anisotropy corresponding with the location of these anomalies is also observed at the cap rock, however, it may originate from the Watrous horizon or overlying layers. ....	80

- Figure 6.9. Cap rock residual anisotropy anomalies. Anomalies are highlighted which show greater consistency in magnitude, orientation and spatial extent. Isolated anisotropy vectors, 'A' and 'B' are considered less reliable. Anomalies 'E', 'F' and 'G' show valid amplitude anisotropy at the cap rock horizon. 'C' and 'D' also appear in the Watrous horizon. .... 91
- Figure 6.10. Offset and azimuth distribution for a sample point within the 'E' anomaly, Figure 6.9. Azimuthal coverage is consistent with the exception of the 35-55° range. Offset coverage is fairly even across all azimuths. .... 92
- Figure 6.11. AVOA surface displayed in the amplitude – azimuth plane. Color shading corresponds to amplitude value. A strong azimuthal anisotropy is observed for the 'E' anomaly, Figure 6.9. Red dots represent the AVOA surface fit to the data (blue dots).. 92
- Figure 6.12. Stack image with arrows denoting the location of anomaly 'E', Figure 6.9. Salt dissolution structures are observed in the cap rock (Mississippian) horizon which extend upwards through the Watrous and Lower Gravelbourg horizons. A high magnitude of anisotropy with north east orientation corresponds to this feature, which extends from the southern edge of the survey area roughly 1km north. Anisotropy is also observed in the Watrous horizon at this location; however, its magnitude is greatly reduced in comparison to the cap rock..... 93
- Figure 6.13. Stack image with arrows denoting the location of anomaly 'F', Figure 6.9. Salt dissolution structures are observed in the cap rock (Mississippian) horizon which extend upwards through the Watrous and Lower Gravelbourg horizons. A high magnitude of anisotropy corresponds to the flanks of this feature. Anisotropy is oriented to the north east. .... 94
- Figure 6.14. Offset and azimuth distribution for a sample point within the 'G' anomaly, Figure 6.9. Azimuthal coverage is consistent with the exception of the 35-55° range. Offset coverage is fairly even across all azimuths. .... 95
- Figure 6.15. AVOA surface displayed in the amplitude – azimuth plane. Color shading corresponds to amplitude value. A strong azimuthal anisotropy is observed for the 'G' anomaly, Figure 6.9. Red dots represent the AVOA surface fit to the data (blue dots).. 95
- Figure 6.16. Comparison between a) Bunge, 2000 oriented core fracture orientations and b) AVOA inversion orientation of anisotropy. Bunge, 2000 notes that in a) open fracture directions are roughly 30°, 315° and 285° while the healed fracture directions are 80°. AVOA inversion appears to be sensitive to similar open fracture orientations..... 96
- Figure 6.17. Anisotropy vectors with well trajectories overlain. Horizontal producers, black, horizontal injectors, red and anisotropy magnitude and orientations are shown as blue vectors. .... 96

## List of Tables

Table 2.1. Relation between the Thomsen's 1986 anisotropic parameters for VTI models and the rotated Thomsen (1986) and Rüger (1997) parameters for HTI models (Rüger, 1998). .....	27
Table 3.1. Data acquisition parameters for the Weyburn 2001 land 3D seismic survey..	38
Table 3. Earth model used to model the synthetic AVOA response. Modeling layers were used to study the influence of possible anisotropy in the overburden. The Watrous layer was made anisotropic to test for the effects of anisotropy immediately above the cap rock. ....	53

## Abbreviation Summary

AVO	Amplitude variation with offset
AVOA	Amplitude variation with offset and azimuth
CMP	Common mid-point
EOR	Enhanced Oil Recovery
$G_{\text{aniso}}$	Anisotropic component of the AVO gradient
$G_{\text{iso}}$	Isotropic component of the AVO gradient
HTI	Transverse isotropy with a horizontal axis of symmetry
NMO	Normal moveout
RMS	Root mean square
VTI	Transverse isotropy with a vertical axis of symmetry

## Chapter 1. Introduction

---

Ensuring cap rock integrity of geologic reservoirs is an essential part in determining the feasibility of long term CO<sub>2</sub> storage in geological formations. This study aims to assess the cap rock of the Weyburn-Midale reservoir in south-east Saskatchewan for the presence of fractures using seismic techniques. Currently, there are few practical means outside of extensive and costly core sampling to detect the presence of fractures within the sealing unit(s) of potential geological storage sites. Fracture analysis using AVOA (amplitude versus offset and azimuth) techniques provides maps of seismic anisotropy, at the cap rock horizon, over large areas using existing 3D seismic datasets. Anisotropy maps identify areas of potential fracturing, however, the source of anisotropy is non-unique and may also result from differences in the horizontal stress field, aligned mineral fabrics or faults.

This study uses vertical component seismic data from a 2001 land based 3D seismic survey which contains sufficient offset and azimuth coverage required for AVOA analysis. The observed amplitude anisotropy is inverted to determine the magnitude and orientation of the anisotropic contribution to the near-offset AVO gradient. The magnitude and orientation are then plotted to provide anisotropy maps at the cap rock and overlying horizon. Modeling is conducted to determine if the effect of anisotropy in the overburden and layers immediately above the cap rock will introduce unacceptable levels of uncertainty in AVOA analysis. Of particular interest is the effect of known underlying fracture induced anisotropy from the reservoir and whether its response can be separated

from that of the overlying layers. Constraints on the orientation and magnitude of the AVOA response are also addressed.

## **1.1. Background geology**

The Weyburn-Midale field is located in the north-central Williston Basin south east of the town of Weyburn, Saskatchewan. The naturally fractured reservoir is composed of an upper dolostone (Midale Marly) and lower limestone (Midale Vuggy). The immediate Midale Evaporite cap rock (4-6m) is similar in velocity and density to the overlying Ratcliffe evaporite beds (15-30m), which produce a combined Ratcliffe-Midale Evaporite seismic response. Regional dip at the cap rock level is negligible at 1-2°. Core samples from the cap rock level show little evidence of fractures; however, there are concerns that fluid injection associated with EOR operations may have caused pressure induced fracturing above the reservoir level.

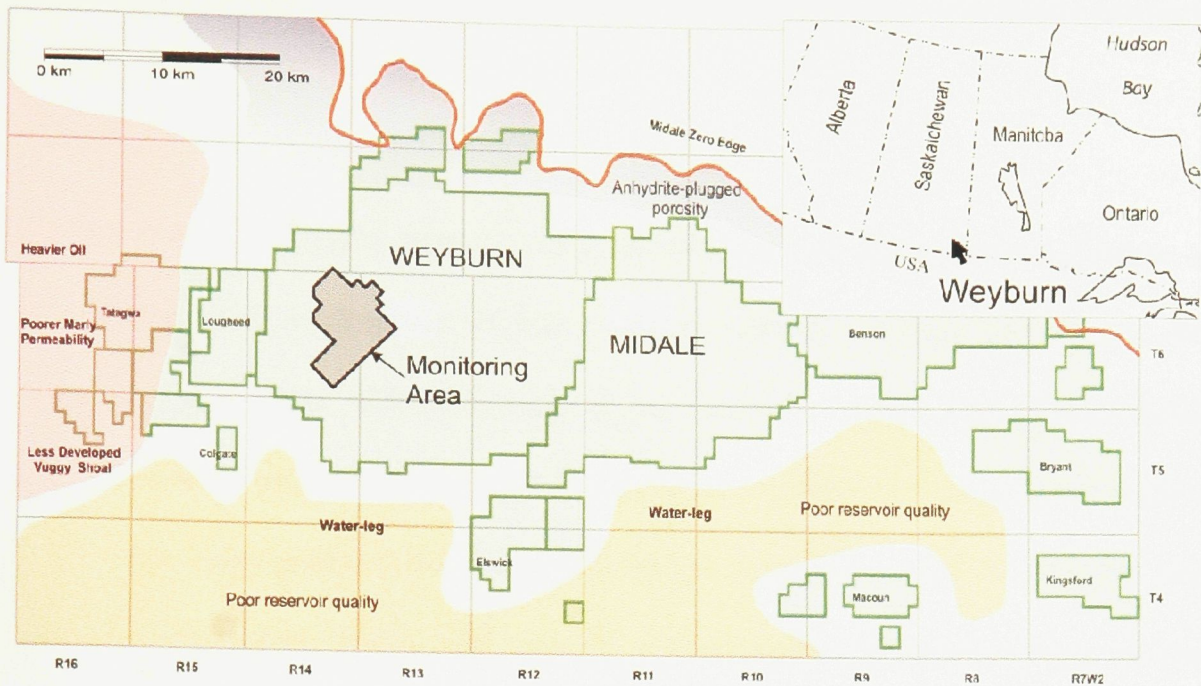


Figure 1.1 Weyburn Field, southeast Saskatchewan. The Phase 1A monitoring area (grey shading) is being considered for this study. Image source: modified (White, 2009).

### 1.1.1. Reservoir and sealing units

The Mississippian Midale reservoir is part of the Charles Formation which contains the Midale Beds, Ratcliffe Beds and Poplar Beds as part of the upper Madison Group. The Madison group unconformably overlies the Bakken Formation on the Devonian-Mississippian boundary. The upper Charles Formation is truncated by the sub-Mesozoic unconformity. The unconformity represents an erosional episode lasting roughly 150 million years. The depositional environment is interpreted as being either a broad carbonate shelf or as part of a carbonate ramp (Kent, 1984). Deposition patterns changed with sea level. Increased sedimentation rates during sea level highstand contributed to the formation of grain shoals which are semi-continuous. During lowstand periods, the

shoals acted as barriers allowing dolomitization and the formation of platform evaporites (Pendrigh, 2005).

The lower reservoir formed primarily in a marine lagoonal setting, with carbonate and shoal development resulting in higher reservoir quality. Grain size ranges from wackestone to grainstone with thickness varying between 10 and 20m. Permeabilities range from 1 to 500md averaging 20md and porosity averages 15%. The upper reservoir unit is a more homogeneous dolostone with higher average porosity of 26% and lower permeability (Burrowes, 2001). The majority of past production has been from the lower Vuggy unit, current CO<sub>2</sub> injection occurs in the upper Marly.

The Frobisher evaporite immediately overlies the upper Midale Marly reservoir, however it is not present in the southern regions of the field area. The unit is characterized as having a nodular texture with dolomicrite or argillaceous dolostone between the nodules. The Frobisher beds are generally not fractured; however, the nodular texture is noted to be prone to smaller fractures on the order of millimeter to centimeter scale (Kent, 2004).

The Midale Evaporite conformably overlies the upper Midale Beds forming a relatively impermeable seal for the Midale reservoir. The unit is composed mainly of anhydrite with higher density than surrounding units and thickness ranging from 2 to 11m. The succession is characterized by lower laminated to massive anhydrite grading upward into nodular anhydrite with dolostone interbeds (Nickel and Qing, 2004). Immediately above the Midale Evaporite is a sharp transition into the Ratcliffe Beds, a two to 11m thick

dolostone unit. The geophysical log and seismic signatures of the Ratcliffe and Midale Evaporite are similar. This study considers these units as a combined cap rock interval. Fractures are observed to be rare within the Midale Evaporite and are interpreted as having developed contemporaneously with deposition or shortly after. Sulphur isotope ratios observed at the Midale Evaporite are similar to Mississippian seawater which suggests a lack of post depositional fluid interaction. Additionally, no evidence of fluid transport, such as oil staining or cement precipitation is observed (Qing, 2004).

The Watrous Formation (Triassic to Middle Jurassic) overlies the sub-Mesozoic unconformity. The Watrous is further divided into a lower and upper unit. The lower unit is composed of mostly mud and silt red beds ranging from 0 to 63m in thickness with effective porosities around 1% (Whittaker, 2004). The upper Watrous is formed of organic rich mudstone with pervasive anhydrite (White et al., 2004). The lower Watrous forms an extensive primary seal to the Weyburn system. No significant fractures are observed within this unit; however, microfractures are observed in muddier layers (Whittaker, 2004).

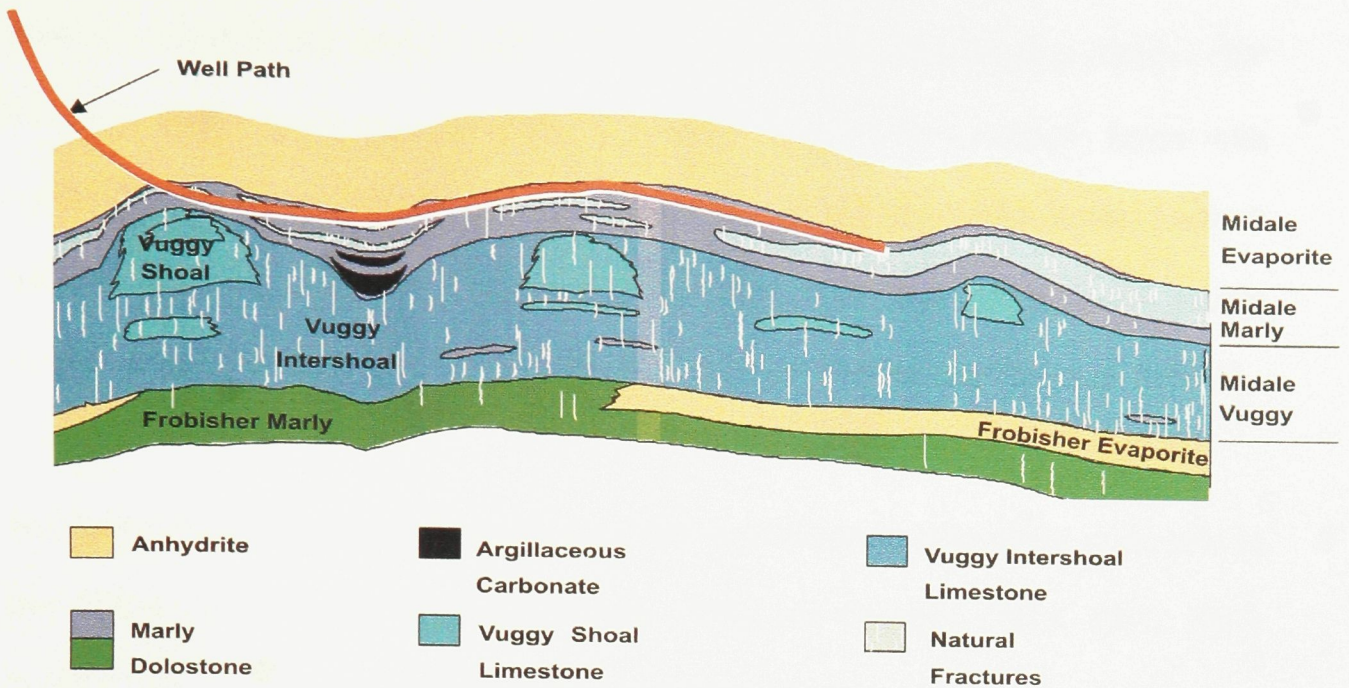


Figure 1.2. Schematic diagram of the Weyburn-Midale reservoir and cap rock. The Midale Evaporite forms the immediate cap rock to the reservoir; however, it is similar in geophysical logs and seismic response to the overlying Ratcliffe Beds, for the purpose of this study the Midale Evaporite and Ratcliffe beds form the cap rock interval. Image source: IEA GHG Weyburn CO<sub>2</sub> monitoring and storage project summary report 2000-2004 (Whittaker, 2004).

## 1.2. Literature review

This section provides a brief summary of developments in the use of anisotropy in exploration seismology. The following is a summary of Helbig and Thomsen (2005) a historical review of anisotropy in exploration seismology.

Anisotropy was often neglected in the early years of exploration seismology. Helbig in 1954 observed velocities parallel to the foliation in schist were 20% higher than those across the foliation. This led to the publication of Helbig's thesis in 1958 which examines layer induced anisotropy. Layer induced anisotropy is the behaviour of multiple thin (relative to the seismic wavelength) isotropic layers with varying elastic parameters responding as a long-wavelength transversely isotropic (TI) medium.

However, conventional seismic surveys of that time recorded only the near offsets ( $<30^\circ$  incidence angle), for which the anisotropy introduced from thin isotropic layers with similar  $V_p/V_s$  ratio has little effect. This resulted in reduced demand for further research into the effects of anisotropy in seismic exploration. Less than one technical journal article was published on anisotropy, on average, per year (Helbig and Thomsen, 2005).

Anisotropy became increasingly more important in exploration seismology in the mid to late 1980s. In particular Gupta (1973a,b, 1974) and Crampin (1978, 1981, 1987) describe the azimuthal anisotropy introduced from aligned fractures in an otherwise isotropic rock (Helbig and Thomsen, 2005). Early theoretical studies of azimuthal anisotropy in P-wave amplitude variation with offset (AVO) were published by Mallick and Frazer (1991), Rüger and Tasvankin, (1995), Strahilevits and Gardner (1995), Sayers and Rickett (1997), and Pérez (1999). The exploration community now had the opportunity to invert seismic data to determine the alignment and intensity of fractures, particularly at the reservoir level. Field studies by Lefeuvre (1994) and Lynn et al. (1995) showed the azimuthal dependence of the P-wave AVO response from fractured reservoirs (Perez, 1999).

In the late 1990's and early 2000's a few key studies provided the necessary equations and methodology to allow the use of P-wave azimuthal anisotropy in the presence of fractured media to be exploited. Rüger and Tsvankin (1997) and Rüger (1998) adapt the simplified equation for the variation of reflection coefficient with offset from Shuey (1985) to account for the azimuthal variation introduced by a single set of aligned vertical fractures. These equations use the contrast in medium properties (P- and S-wave velocities, density and Thomsen's anisotropy parameters) at an interface along with incidence angle and source-receiver azimuth. While the equation describes the variation of reflection coefficient with offset and azimuth, in practice reflection amplitudes are used in place of the reflection coefficient. The equation may then be solved for the anisotropic contribution to the AVO gradient and the orientation of the symmetry axes from which the anisotropy (fracture) orientation is determined. This was often done using azimuth binning to determine the AVO gradient for several azimuths and then to determine the AVO gradient variation with azimuth. Since the equation is non-linear, reflection amplitudes could not be directly inverted for these parameters using linear least squares regression. This problem was solved by adapting the (Grechka and Tsvankin, 1998) solution for anisotropic reflection moveout (Jenner, 2001; Hall and Kendall 2003). This allows the use of all trace amplitudes at their correct offset and azimuth without any of the drawbacks of azimuth binning (Jenner, 2001). The error can then be determined using the propagation of error on each of the regression coefficients. This method is now widely used in field studies to determine the orientation of fracturing (*e.g.* Jenner, 2001; Gray, 2002; Hall & Kendall, 2003; Minsley, 2004; Al-Marzoug, 2006; Al-Shuhail, 2007; Sinha, 2008)

While these studies use the simplest physical model, that of aligned vertical fractures in an otherwise isotropic medium, the equations which describe more complicated and realistic models have been known for some time. Vertical fractures in layered strata or multiple vertical fracture sets will form an orthorhombic symmetry. Solutions of the reflection coefficient under these conditions have been provided by Rüger (1998) and Bakulin (2000) with solutions to the anisotropic parameters provided by Tsvankin (1997) and Grechka (1999). A field study using 3-D moveout inversion to determine the anisotropic parameters has been performed by Grechka and Tsvankin (1999).

## **Chapter 2. Theory**

---

Exploration seismology has considered the propagation of elastic waves under the assumptions of isotropy with great success for many years. Within the last decade, methods for extracting additional information from anisotropic models have become increasingly more common. AVOA is a technique which provides parameters such as the orientation and magnitude of anisotropy, which is proportional to the crack density and the shear wave splitting parameter for fractured mediums. Determining the intensity and orientation of fracture-induced anisotropy in a medium has traditionally aided in reservoir management and production. This section covers the basic theory necessary for the use of AVOA to measure anisotropy at the cap rock and other horizons of interest.

## 2.1. Elasticity

An elastic material, when deformed under an applied stress, will return to its previously unstrained state when the stress is removed. In the case of linearly elastic materials, each stress ( $\sigma_{ij}$ ) will produce a strain ( $\epsilon_{kl}$ ) such that the total strain is the sum of all applied stress. Under small strains, the linear relationship between stress and strain is governed by Hooke's law. The generalized form of which can be expressed in tensor notation as:

$$\sigma_{ij} = C_{ijkl} \epsilon_{kl} \quad (2.1)$$

Each index of stress and strain may take on values  $x_1, x_2, x_3$  representing the three orthogonal directions (x,y,z) of the Cartesian coordinate system. Stress and strain are expressed as second-order (3x3) matrices with Hooke's constant of proportionality ( $C_{ijkl}$ ) relating them using a fourth-order (3x3x3x3) tensor, the components of which are elastic constants. The tensor  $\mathbf{C}$  is referred to as the stiffness tensor and its inverse, ( $\mathbf{S} = \mathbf{C}^{-1}$ ), is the compliance tensor (Sheriff & Geldart, 1995; Tsvankin, 2001). The symmetry of the stress and strain matrices allows the 81 components of the stiffness tensor to be reduced to 36 and from the law of conservation of energy a further reduction to 21 independent elastic constants is possible (Hudson, 1980).

The relationship between the elastic properties of a medium and seismic wave propagation is described by the Christoffel equation:

$$\begin{bmatrix} G_{11} - \rho V^2 & G_{12} & G_{13} \\ G_{21} & G_{22} - \rho V^2 & G_{23} \\ G_{31} & G_{32} & G_{33} - \rho V^2 \end{bmatrix} \begin{bmatrix} U_1 \\ U_2 \\ U_3 \end{bmatrix} = 0 \quad (2.2)$$

Where  $V$  is the phase velocity,  $\rho$  is the density and  $\mathbf{U}$  is the polarization direction. The Christoffel matrix,

$$G_{ik} = C_{ijkl} n_j n_l \quad (2.3)$$

where  $\mathbf{n}$ , the phase direction, is symmetric as follows from the intrinsic symmetries of the stiffness tensor.

$$C_{ijkl} = C_{jikl} = C_{ijlk} = C_{klij} \quad (2.4)$$

$$G_{ik} = G_{ki} \quad (2.5)$$

The Christoffel equation depends on the stiffness of the medium and the direction of wave propagation. Solutions of the 3x3 eigenvalue – eigenvector problem are found from

$$\det[G_{ik} - \rho V^2 \delta_{ik}] = 0 \quad (2.6)$$

where  $\delta$  is the Kronecker delta ( $\delta \equiv 1$  for  $i = k$  and  $\delta_{ik} \equiv 0$  for  $i \neq k$ ). For any direction, the equation yields three values for the phase velocity which correspond to the P-wave and two S-wave velocities (Hall, 2000a; Tsvankin, 2001).

If the properties of a medium are invariant with direction then, the medium is isotropic. In this case, only two independent elastic constants,  $\lambda$  and  $\mu$ , are necessary to describe the elasticity. Hooke's law can be reduced to:

$$\sigma_{ii} = \lambda\Delta + 2\mu\varepsilon_{ii} \quad (i = x, y, z) \quad (2.7)$$

$$\sigma_{ij} = 2\mu\varepsilon_{ij} \quad (i, j = x, y, z; i \neq j) \quad (2.8)$$

where  $\Delta$  is the change in volume per unit volume or expressed in matrix form,  $\sigma = C_{iso}\varepsilon$ ,

where:

$$C^{iso} = \begin{bmatrix} \lambda + 2\mu & \lambda & \lambda & 0 & 0 & 0 \\ \lambda & \lambda + 2\mu & \lambda & 0 & 0 & 0 \\ \lambda & \lambda & \lambda + 2\mu & 0 & 0 & 0 \\ 0 & 0 & 0 & \mu & 0 & 0 \\ 0 & 0 & 0 & 0 & \mu & 0 \\ 0 & 0 & 0 & 0 & 0 & \mu \end{bmatrix} \quad (2.9)$$

and where  $\lambda$  and  $\mu$  are Lamé's constants which determine the P-wave and S-wave velocities (Sheriff & Geldart, 1995).

$$v_P = \sqrt{\frac{\lambda + 2\mu}{\rho}}, \quad v_S = \sqrt{\frac{\mu}{\rho}} \quad (2.10)$$

Isotropic media may be considered a degenerate form of anisotropic media in which the two S-wave velocities are identical (Tsvankin, 2001).

## 2.2. Symmetry systems

The structure of the stiffness tensor  $C_{ijkl}$  is governed by the symmetry of the medium. Higher symmetry systems require fewer independent elements to describe the stiffness of the medium and reduce the problem from 21 components to 5. For practical seismological applications, there are a few symmetries of particular interest (Tsvankin, 2001).

### 2.2.1. VTI and HTI models

Hexagonal symmetry has a single rotational axis of symmetry and 5 independent stiffness coefficients. The seismic properties for such a medium depend only on the angle between the propagation direction and symmetry axis. The isotropy plane is perpendicular to the symmetry axis. Velocities of the three wave modes in this plane are independent of propagation direction as the angle between the phase velocity and symmetry axis remains a constant  $90^\circ$ . Examples of hexagonal symmetry are the TI (transverse isotropy) symmetries, for which two orientations are most common in applied

studies: vertical transverse isotropy (VTI) and horizontal transverse isotropy (HTI) symmetries. A TI medium has a single axis of rotational symmetry. Geologically, VTI can be produced by aligned plate-shaped clay particles, such as those found in shales which comprise a large percentage of clastic fill in sedimentary basins (Tsvankin, 2001). HTI, of particular interest in this thesis, can be produced in media with parallel vertical fractures (Figure 2.1). The stiffness tensor for HTI media takes the form:

$$C^{HTI} = \begin{bmatrix} c_{11} & c_{13} & c_{13} & 0 & 0 & 0 \\ c_{13} & c_{33} & c_{33} - 2c_{44} & 0 & 0 & 0 \\ c_{13} & c_{33} - 2c_{44} & c_{33} & 0 & 0 & 0 \\ 0 & 0 & 0 & c_{44} & 0 & 0 \\ 0 & 0 & 0 & 0 & c_{55} & 0 \\ 0 & 0 & 0 & 0 & 0 & c_{55} \end{bmatrix} \quad (2.11)$$

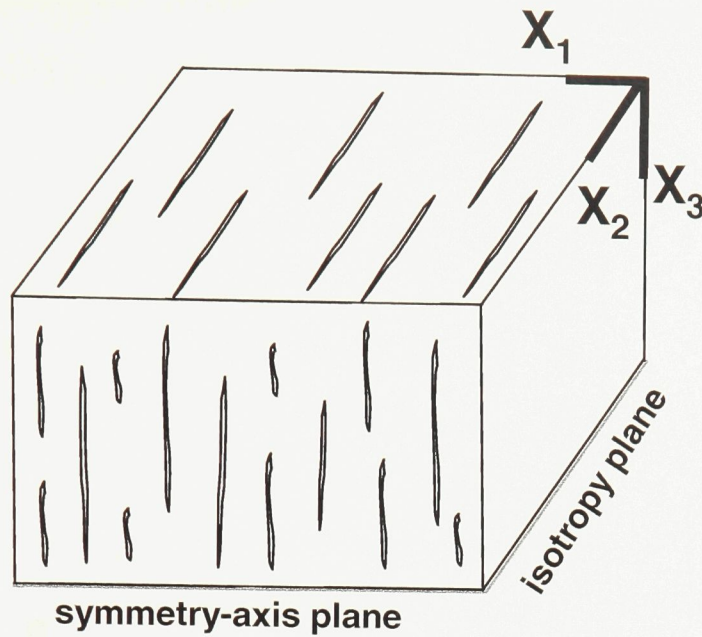


Figure 2.1 Diagram of a medium with fracture induced anisotropy and a HTI (Horizontal Transverse Isotropy) symmetry in the  $X_1$  direction. The isotropy plane is the  $[X_2, X_3]$  plane parallel to the fracture surfaces. For propagation in this plane, P- and S-waves travel with velocities of the isotropic host rock. The symmetry-axis lies in the  $[X_1, X_3]$  plane orthogonal to the fracture surfaces where P- and S-wave velocities are reduced due to the increased compliance of the fractures. Source, modified (Rüger, 1998).

In HTI media, the two symmetry planes are vertical. The symmetry-axis plane  $[X_1, X_3]$  is formed by the symmetry axis (horizontal) and the vertical.

### 2.2.2. Orthorhombic models

Orthorhombic media is characterized by three mutually orthogonal planes of symmetry and 9 independent elastic coefficients. Common examples of orthorhombic media include a single set of vertical parallel fractures in finely layered media (that is, vertical fractures in a VTI medium) and two orthogonal sets of vertical fractures in an isotropic

host rock. Orthorhombic symmetry presents one of the simplest practical models of anisotropy for geophysical applications.

$$C^{ORT} = \begin{bmatrix} c_{11} & c_{12} & c_{13} & 0 & 0 & 0 \\ c_{12} & c_{22} & c_{23} & 0 & 0 & 0 \\ c_{13} & c_{23} & c_{33} & 0 & 0 & 0 \\ 0 & 0 & 0 & c_{44} & 0 & 0 \\ 0 & 0 & 0 & 0 & c_{55} & 0 \\ 0 & 0 & 0 & 0 & 0 & c_{66} \end{bmatrix} \quad (2.12)$$

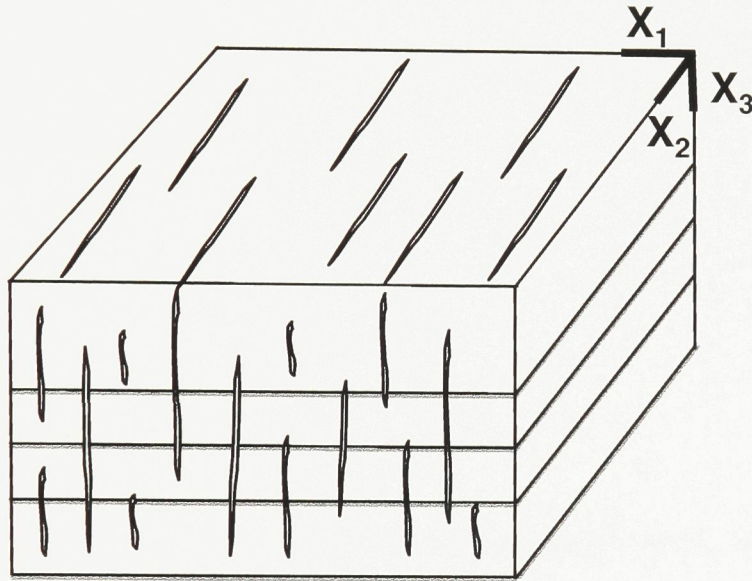


Figure 2.2 Horizontal layered strata and parallel vertical cracks forming orthorhombic symmetry. Adapted from (Rüger, 1998).

Lower forms of symmetry include monoclinic and triclinic. A formation containing two different sets of vertical fractures which are not orthogonal will have a monoclinic symmetry with 13 independent coefficients and a horizontal axis of symmetry. Triclinic

symmetry is the most general anisotropic model with 21 independent stiffness coefficients. Its complexity limits the practical application of this model in seismology.

### 2.3. Wave propagation in anisotropic media

Below the basic theory of wave propagation in anisotropic media is provided following Aki and Richards (1980), Sheriff and Geldart (1995), Hall et al. (2000) and Tsvankin (2001).

Wave propagation in anisotropic media can be described using a homogenous solution of the plane wave equation. The tractions acting across a surface of some volume in terms of the stress tensor  $\sigma_{ij}$  yields:

$$\rho \frac{\partial^2 \mu_i}{\partial t^2} = \frac{\partial \sigma_{ij}}{\partial x_j}, \quad (2.13)$$

where  $\rho$  is the density,  $t$  is time and  $u$  is the displacement vector. Substituting the generalized Hooke's law, equation (2.1), and the strain tensor defined as:

$$\varepsilon_{kl} = \frac{1}{2} \left( \frac{\partial \mu_k}{\partial x_l} + \frac{\partial \mu_l}{\partial x_k} \right) \quad (2.14)$$

the wave equation for homogenous anisotropic media becomes

$$c_{ijkl} \frac{\partial^2 \mu_l}{\partial x_j \partial x_k} = \rho \frac{\partial^2 \mu_i}{\partial t^2}. \quad (2.15)$$

A harmonic plane wave solution of the equation is represented by

$$\mu_i = A_i e^{i\omega(t \pm x_i n_i / v_n)} \quad (2.16)$$

Where  $A$  is the amplitude and  $\omega$  is the angular frequency of a plane wave with unit normal,  $n_i$ , and phase velocity  $v_n$ . Substituting the plane wave solution into the wave equation yields

$$(c_{ijkl} n_i n_l - \rho v_n^2 \delta_{jk}) = 0 \quad (2.17)$$

for non-zero amplitudes. The eigenvalues determined from

$$\det[(c_{ijkl} n_i n_l - \rho v_n^2 \delta_{jk})] = 0 \quad (2.18)$$

correspond to three phase velocities (quasi-P and two quasi-S) of the wavefronts propagating through an anisotropic medium. Although the eigenvectors of the symmetric Christoffel equation are mutually orthogonal, none of them are necessarily parallel to the

wavefront normal. Therefore, in anisotropic media, the modes of wave propagation are referred to as quasi-P and quasi-S waves (Hall, 2000a; Tsvankin, 2001).

In isotropic media, relative to the phase velocity vector (wavefront normal) the direction of particle motion is parallel for P-waves and orthogonal for S-waves. In the presence of anisotropy, the direction of particle motion is then determined by the wavefront normal in addition to the elastic constants of the media.

In order to provide a solution of the three phase velocities, a stiffness tensor symmetry must first be selected as the polarization is dependant on the elastic constants of the medium. The most common anisotropic model in exploration seismology is transverse isotropy. The following solutions are given in Thomsen (1986) for a TI medium with a vertical axis of symmetry (VTI).

$$C^{VTI} = \begin{bmatrix} c_{11} & c_{11} - 2c_{66} & c_{13} & 0 & 0 & 0 \\ c_{11} - 2c_{66} & c_{11} & c_{13} & 0 & 0 & 0 \\ c_{13} & c_{13} & c_{33} & 0 & 0 & 0 \\ 0 & 0 & 0 & c_{55} & 0 & 0 \\ 0 & 0 & 0 & 0 & c_{55} & 0 \\ 0 & 0 & 0 & 0 & 0 & c_{66} \end{bmatrix} \quad (2.19)$$

$$\rho v_P^2(\theta) = \frac{1}{2} [C_{11} + C_{66} + (C_{33} - C_{11}) \sin^2 \theta + D(\theta)] \quad (2.20)$$

$$\rho v_{SH}^2(\theta) = \frac{1}{2} [C_{11} + C_{66} + (C_{33} - C_{11}) \sin^2 \theta - D(\theta)] \quad (2.21)$$

$$\rho v_{SV}^2(\theta) = C_{44} \sin^2 \theta + C_{66} \cos^2 \theta \quad (2.22)$$

$$D \equiv \left[ \frac{(C_{11} - C_{66})^2 + 2[2(C_{13} - C_{66})^2 - (C_{11} - C_{66})(C_{33} + C_{11} - 2C_{66})]\sin^2 \theta}{+ [(C_{33} + C_{11} - 2C_{66})^2 - 4(C_{13} + C_{66})^2]\sin^4 \theta} \right]^{\frac{1}{2}} \quad (2.23)$$

For horizontally propagating waves the solutions for the three velocities become

$$v_P(\theta = 90^\circ) = \sqrt{\frac{c_{11}}{\rho}}, \text{ vertical P-wave} \quad (2.24)$$

$$v_{SH}(\theta = 90^\circ) = \sqrt{\frac{c_{66}}{\rho}}, \text{ shear wave with horizontal polarization} \quad (2.25)$$

$$v_{SV}(\theta = 90^\circ) = \sqrt{\frac{c_{55}}{\rho}}, \text{ shear wave with vertical polarization} \quad (2.26)$$

Since  $c_{55} \neq c_{66}$ , the orthogonally polarized shear waves travel with different velocities which results in shear wave splitting. Although these solutions offer few insights into the elastic properties of the medium, the equations indicate that for TI media the velocity anisotropy will have a combination of  $\cos 2\theta$  and  $\cos 4\theta$  variation (Hall 2000; Tsvankin 2001).

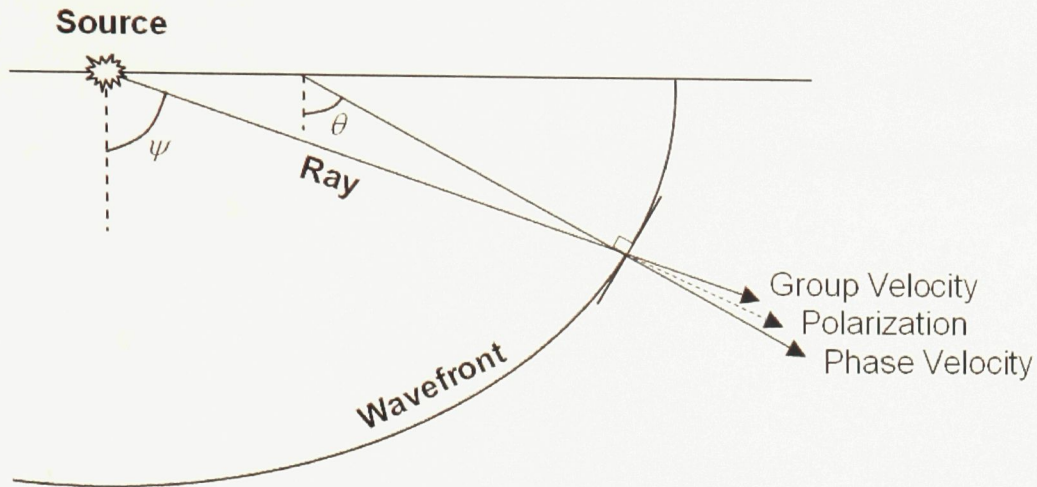


Figure 2.3 Diagram showing the relationship between the group velocity, polarization and phase velocity. The phase velocity is constant and propagates in the direction normal to the wavefront. The group velocity is the velocity along the ray path. The particle motion, or polarization, travels at an angle between the phase velocity and group velocity. Where  $\theta$  is the angle between the vertical and the phase velocity and  $\psi$  is the angle between the group velocity and vertical. Image adapted from (Hall, 2000a; Tsvankin, 2001)

## 2.4. Fractured medium models

Geologists often describe fracturing in terms of the fracture intensity, the number of fractures per metre and by the aperture, the opening width of the fracture. These properties typically range from 1-20 fractures  $\text{m}^{-1}$  and 0.001-0.1 m for carbonate reservoirs (Bakulin, 2000). On the order of the seismic wavelength, fractured rock can be considered an “effective anisotropic media” (Hall, 2000). There are several models of effective anisotropic media from which the fracture parameters can be determined. The most common models consider the excess compliance introduced by fractures through a displacement discontinuity as in the linear slip model after Schoenberg (1980), Schoenberg and Sayers (1995) or, alternatively as aligned penny shaped cracks after Hudson (1980).

The excess compliance for a general fracture system containing  $m$  differently aligned fracture sets, each set with a different alignment, embedded in an otherwise isotropic host rock can be expressed as:

$$s_{ijkl} = s_{ijklb} + \sum_m^{(m)} s_{ijklf} \quad (2.27)$$

Where  $s_{ijklb}$  is the compliance of the background and  $s_{ijklf}$  is the additional compliance of the fractures. The additional compliance is expressed through the fracture system compliance tensor,  $Z_{ij}$ ,

$$s_{ijklf} = \frac{1}{4} \sum_m \left( Z_{ik}^{(m)} n_l^{(m)} n_j^{(m)} + Z_{jk}^{(m)} n_l^{(m)} n_i^{(m)} + Z_{il}^{(m)} n_k^{(m)} n_j^{(m)} + Z_{jl}^{(m)} n_k^{(m)} n_i^{(m)} \right), \quad (2.28)$$

Where,

$$\frac{1}{V} \sum_q \int_{S_q} [u_i] dS \equiv Z_{ij} \bar{\sigma}_{ij} n_k \quad (2.29)$$

The displacement vector  $[u_i]$  is the difference in displacements of the fracture surfaces,  $S_q$ , within a volume  $V$  under the average applied stress. For a single vertical fracture set, with fractures parallel to the  $x_2$  axis, the compliance tensor is given by

$$s_f = \begin{bmatrix} Z_N & 0 & 0 & 0 & Z_{NV} & Z_{NH} \\ 0 & 0 & 0 & 0 & 0 & 0 \\ 0 & 0 & 0 & 0 & 0 & 0 \\ 0 & 0 & 0 & 0 & 0 & 0 \\ Z_{NV} & 0 & 0 & 0 & Z_V & Z_{VH} \\ Z_{NH} & 0 & 0 & 0 & Z_{VH} & Z_H \end{bmatrix} \quad (2.30)$$

The tensor is often simplified by letting the normal compliance of the fractures be given by  $Z_N$  and the tangential compliance by  $Z_T$  (Grechka 2003). Provided the fractures are invariant with rotation about their normal axis; then the number of independent coefficients is reduced to two.

$$Z_{ij} = Z_N n_i n_j + Z_T (\delta_{jk} - n_i n_j) \quad (2.31)$$

$$s_f = \begin{bmatrix} Z_N & 0 & 0 & 0 & 0 & 0 \\ 0 & 0 & 0 & 0 & 0 & 0 \\ 0 & 0 & 0 & 0 & 0 & 0 \\ 0 & 0 & 0 & 0 & 0 & 0 \\ 0 & 0 & 0 & 0 & Z_T & 0 \\ 0 & 0 & 0 & 0 & 0 & Z_T \end{bmatrix} \quad (2.32)$$

The determination of  $Z_N$  and  $Z_T$  in terms of host rock and fracture properties depends on the assumptions of a specific model. If the elastic properties of the isotropic background

rock are known, then it is theoretically feasible to determine the additional compliance from aligned vertical fractures through seismic data. For HTI symmetry, four independent stiffness coefficients may be determined: the two Lamé parameters of the host rock and the compliance coefficients,  $Z_N$  and  $Z_T$ . The compliance coefficients represent the minimum fracture weakness information that may be determined uniquely (Bakulin, 2000; Hall, 2000a).

### 2.4.1. Hudson's theory

Hudson's (1980, 1981, 1986) "penny-shaped" cracks medium theory describes the perturbation of the displacement field due to progressive scattering of a wave from a series of ellipsoidal micro-cracks. The perturbation is described through a power series expression of the stiffness tensor. The series is truncated after three terms with the first term describing the scattering of a seismic wave by a single crack and the second term by a second crack and so on. The scattering across a fracture is determined by the displacement discontinuity across the fracture surface which is expressed as,

$$\int_S [u_i] dS = \frac{a^3}{\mu} \bar{U}_{ij} \bar{\sigma}_{ij} n_k \quad (2.33)$$

Where  $\bar{U}_{ij} = \frac{\mu Z_{ij}}{n_c}$ ,  $n_c = \frac{Na^3}{V}$  the crack density,  $a$  is the crack radius,  $V$  is the volume of the medium and  $N$  is the number of cracks. Considering rotationally invariant fractures, the equation for  $U_{ij}$  simplifies to two terms:-

$$\bar{U}_{11} = \frac{4 (\lambda_b + 2\mu_b)}{3 (\lambda_b + \mu_b)} \frac{1}{(1+K)} \quad (2.34)$$

$$\bar{U}_{33} = \frac{16 (\lambda_b + 2\mu_b)}{3 (3\lambda_b + 4\mu_b)} \frac{1}{(1+M)} \quad (2.35)$$

$$K = \frac{\left(K_f + \frac{4}{3}\mu_f\right) (\lambda_b + 2\mu_b)}{\pi d \mu_b (\lambda_b + \mu_b)}, \quad M = \frac{u_f (\lambda_b + 2\mu_b)}{\pi d \mu_b (3\lambda_b + 4\mu_b)} \quad (2.36)$$

Where  $K_f$  is the bulk modulus of the crack fill material,  $K_f = \lambda_f + \frac{2}{3}\mu_f$  and  $d$  is the aspect ratio of the crack, defined as half the crack thickness divided by the crack radius.

Substituting  $\nu_p$  and  $\nu_s$ , equation (2.10), into  $\frac{(\lambda_b + 2\mu_b)}{(\lambda_b + \mu_b)}$  and  $\frac{(\lambda_b + 2\mu_b)}{(3\lambda_b + 4\mu_b)}$ ,  $U_{11}$  and  $U_{33}$

can be expressed in terms of the host rock velocities.

$$\frac{(\lambda_b + 2\mu_b)}{(\lambda_b + \mu_b)} = \left(1 - \frac{\nu_s^2}{\nu_p^2}\right)^{-1} \quad (2.37)$$

$$\frac{(\lambda_b + 2\mu_b)}{(3\lambda_b + 4\mu_b)} = \left(3 - 2\frac{\nu_s^2}{\nu_p^2}\right)^{-1} \quad (2.38)$$

Where  $\alpha$  and  $\beta$  are the P- and S-wave velocities respectively. The fracture weakness coefficients,  $Z_N$  and  $Z_T$ , can be related to  $U_{11}$  and  $U_{33}$  as follows,

$$\frac{(\lambda + 2u) Z_N}{1 + (\lambda + 2u) Z_N} = \frac{(\lambda + 2u)}{\mu} U_{11} e \quad (2.39)$$

$$\frac{uZ_T}{1 + uZ_T} = U_{33} e \quad (2.40)$$

Where  $e$  is the crack density.

### 2.4.2. Thomsen's parameters

The elastic stiffness coefficients expressed in tensor notation,  $C_{ij}$ , or matrix form have traditionally been useful for inversion and forward modeling problems involving specific symmetries. The elastic constants are less suited to the task of understanding the effective parameters which govern the relationship between medium parameters and seismic signatures (Tsvankin, 2001). Thomsen's (1986, 1995) notation improves on the conventional  $C_{ij}$  notation by expressing specific combinations of elastic constants which represent the strength of anisotropy in the medium. Thomsen's parameters for a HTI medium (1995) are expressed as rotated Thomsen VTI parameters (1986).

Rüger (1997) notes that in the  $[x_1, x_3]$  plane the equations describing the kinematic properties and polarizations are identical for HTI and VTI. Notation relating the HTI symmetry parameters to the original Thomsen (1986) parameters for VTI media is listed in Table 2.1.

Table 2.1. Relation between the Thomsen's 1986 anisotropic parameters for VTI models and the rotated Thomsen (1986) and Rüger (1997) parameters for HTI models (Rüger, 1998).

Thomsen (1986) VTI Parameters	Thomsen (1995) HTI (Rotated VTI) Parameters	Rüger (1997) HTI Parameters
$V_{P0} = \sqrt{\frac{c_{33}}{\rho}}, \alpha = V_{P0}(1 + \varepsilon)$	$\alpha = V_{P0} = \sqrt{\frac{c_{33}}{\rho}}$	$\alpha = V_{P0} = \sqrt{\frac{c_{33}}{\rho}}$
$\beta = V_{S_{90}^{\parallel}} = \sqrt{\frac{c_{66}}{\rho}}$	$\beta = V_{S_0^{\parallel}} = \sqrt{\frac{c_{44}}{\rho}}$	$\beta = V_{S_0^{\parallel}} = \sqrt{\frac{c_{44}}{\rho}}$
$\beta^{\perp} = V_{S_{90}^{\perp}} = \sqrt{\frac{c_{44}}{\rho}} = V_{S0}$	$\beta^{\perp} = V_{S_0^{\perp}} = \sqrt{\frac{c_{66}}{\rho}} = V_{S0}$	$\beta^{\perp} = V_{S_0^{\perp}} = \sqrt{\frac{c_{66}}{\rho}} = V_{S0}$
$\delta = \frac{(c_{13} + c_{44})^2 - (c_{33} - c_{44})^2}{2c_{33}(c_{33} - c_{44})}$	$\delta^r = \frac{(c_{13} + c_{66})^2 - (c_{11} - c_{66})^2}{2c_{11}(c_{11} - c_{66})}$	$\delta^{(v)} = \frac{(c_{13} + c_{55})^2 - (c_{33} - c_{55})^2}{2c_{33}(c_{33} - c_{55})} = \delta - 2\varepsilon$
$\varepsilon = \frac{c_{11} - c_{33}}{2c_{33}}$	$\varepsilon^r = \frac{c_{33} - c_{11}}{2c_{11}}$	$\varepsilon^{(v)} = \frac{c_{11} - c_{33}}{2c_{33}} = -\varepsilon$
$\gamma = \frac{c_{66} - c_{44}}{2c_{44}}$	$\gamma^r = \frac{c_{44} - c_{66}}{2c_{66}}$	$\gamma^{(v)} = \frac{c_{66} - c_{44}}{2c_{44}} = -\gamma$

The elastic constants can now be represented as a combination of the vertical velocities  $v_{P(\theta=0^\circ)}$ ,  $v_{S(\theta=0^\circ)}$  and the three dimensionless Thomsen parameters  $\delta, \varepsilon$  and  $\gamma$ .

The parameter  $\varepsilon$  is related to the P-wave anisotropy using a fractional difference between the fast and slow horizontal P-wave velocities. Similarly,  $\gamma$ , represents the fractional difference in S-wave velocities. The parameter  $\delta$  determines the second derivative of the P-wave phase velocity function at vertical incidence (Tsvankin, 2001). In addition, this parameter affects the anisotropic normal moveout velocity and the magnitude of anisotropic AVO gradient. In isotropic media, the parameters  $\delta, \varepsilon$  and  $\gamma$  are zero. If there is no equant porosity, then the excess compliance from low-aspect ratio cracks may be related to normal and tangential weaknesses by (Hall, 2000a):

$$Z_N = \frac{2\varepsilon^r (1 - \nu_b)^2}{1 - 2\nu_b} \frac{1}{\lambda_b + 2\mu_b} \quad (2.41)$$

$$Z_T = \frac{2\gamma^r}{\mu_b} \quad (2.42)$$

## 2.5. P-wave AVOA for vertical fracture systems

A complete plane wave solution for reflection and transmission at an isotropic interface is provided by Aki and Richards (1980). This study considers P-P reflection amplitudes for which the most practical approximation of the reflection coefficient between two isotropic interfaces is given by Shuey (1985):

$$R_{pp}(\theta) = A + B \sin^2 \theta + C (\sin^2 \theta \tan^2 \theta) \quad (2.43)$$

$$A = \frac{1}{2} \frac{\Delta Z}{\bar{Z}} \quad (2.44)$$

$$B = \frac{1}{2} \left[ \frac{\Delta \alpha}{\bar{\alpha}} - \left( \frac{2\bar{\beta}}{\bar{\alpha}} \right)^2 \frac{\Delta G}{\bar{G}} \right] \quad (2.45)$$

$$C = \frac{1}{2} \frac{\Delta \alpha}{\bar{\alpha}} \quad (2.46)$$

$Z = \rho\alpha$ , The vertical P-wave impedance.

$G = \rho\beta^2$ , The vertical shear modulus.

$\bar{x}$  is the mean value and  $\Delta$  is the difference

The  $R_{pp}$  term is the reflection coefficient as a function of incidence angle  $\theta$ . The terms A, B and C are defined by Chapman (1976). The parameters  $\alpha, \beta, \rho$  are the vertical P-wave velocity and the S-wave velocity polarized parallel to the fracture plane (strike), and the density. In practice, seismic amplitudes are used in place of  $R_{pp}$  to solve for the A, B and

C terms. This can be done using a plot of equation (2.43) as a function of  $\sin^2(\theta)$  (dropping the C term). The plot will be a straight line with intercept A and slope B. In this case, A represents the zero offset reflection amplitude or AVO intercept and B is the AVO gradient. The 3<sup>rd</sup> term in the simplified  $R_{pp}(\theta)$  equation describes the behaviour of the reflection amplitude as the incidence angle approaches the critical angle (Shuey, 1985). This term is small at near offsets ( $<30^\circ$  incidence) and may be discarded. The 3<sup>rd</sup> term may also be used when data is available, and of good quality, to help constrain the solution of A and B (Hall 2003).

For the case of azimuthal anisotropy, equation (2.43) is modified by Rüger (1998) to include the modified Thomsen parameters.

$$R_{pp}(\theta, \phi) = A + (B + D \cos^2 \phi) \sin^2 \theta + (C + E \cos 2\phi + F \cos 4\phi) (\sin^2 \theta \tan^2 \theta) \quad (2.47)$$

$$\begin{aligned} A &= \frac{1}{2} \frac{\Delta Z}{\bar{Z}} \\ B &= \frac{1}{2} \frac{\Delta Z}{\bar{Z}} \left[ \frac{\Delta \alpha}{\bar{\alpha}} - \left( \frac{2\bar{\beta}}{\bar{\alpha}} \right)^2 \frac{\Delta G}{\bar{G}} + \Delta \delta^{(v)} + 2 \left( \frac{2\bar{\beta}}{\bar{\alpha}} \right)^2 \Delta \gamma \right] \\ C &= \frac{1}{2} \frac{\Delta \alpha}{\bar{\alpha}} + \frac{1}{8} (3\Delta \epsilon^{(v)} + 2\Delta \delta^{(v)}) \\ D &= \frac{1}{2} \left[ \Delta \delta^{(v)} + 2 \left( \frac{2\bar{\beta}}{\bar{\alpha}} \right)^2 \Delta \gamma \right] \\ E &= \frac{1}{2} \Delta \epsilon^{(v)} \\ F &= \frac{1}{8} [\Delta \epsilon^{(v)} - 2\Delta \delta^{(v)}] \end{aligned} \quad (2.48)$$

Where  $f = 1 - v_{S_0} / v_{P_0}$ , and where  $v_{S_0}$  and  $v_{P_0}$  are the S and P-wave velocities, perpendicular to the fracture plane, respectively.  $\phi$  is the azimuth angle from the reference frame to the isotropy plane. Solutions for the isotropic and anisotropic contribution to the B term and the symmetry axis angle are given in Hall (2000) and Jenner (2001). The azimuthal dependence of the AVO gradient term can be considered the magnitude of anisotropy. The orientation of the anisotropy or fractures is determined by identifying the symmetry plane angle.

Using the near offset approximation, equation (2.47) simplifies to:

$$R_{pp}(\theta, \phi) = A + (G_{iso} + G_{aniso} \cos^2 \phi) \sin^2 \theta \quad (2.49)$$

However, the  $\phi$  term refers to angle relative to the isotropy plane, which is unknown, so the angle between the  $i$ th azimuth and either symmetry plane (unknown),  $\phi_{sym}$ , is used and the equation becomes:

$$R_{pp}(\theta, \phi) = A + (G_{iso} + G_{aniso} \cos^2(\phi - \phi_{sym})) \sin^2 \theta \quad (2.50)$$

In order to determine the unknown symmetry plane angle,  $\phi_{sym}$ , equation (2.50) is re-written using only the source-receiver azimuth,  $\phi$ :

$$R_{pp}(\theta, \phi) = A + [w_{11} \cos^2 \phi + 2w_{12} \cos \phi \sin \phi + w_{22} \sin^2 \phi] \sin^2 \theta \quad (2.51)$$

The coefficients  $w_{ij}$  are solved for using a linear least squares regression. The isotropic and anisotropic contributions to the AVO gradient are then expressed in terms of the  $w_{ij}$  coefficients and the symmetry plane angle ( $\phi_{sym}$ ) is expressed as  $\beta$ .

$$G_{iso} = \frac{1}{2} \left( w_{11} + w_{22} - \sqrt{(w_{11} - w_{22})^2 + 4w_{12}^2} \right) \quad (2.52)$$

$$G_{aniso} = \sqrt{(w_{11} - w_{22})^2 + 4w_{12}^2} \quad (2.53)$$

$$\beta = \tan^{-1} \left[ \frac{w_{11} - w_{22} + \sqrt{(w_{11} - w_{22})^2 + 4w_{12}^2}}{2w_{12}} \right] \quad (2.54)$$

The determination for  $\beta$  is non-unique in that it may represent either the isotropy plane or the symmetry plane which are orthogonal to each other (Hall, 2000a; Jenner, 2001).

## 2.6. Uncertainty in AVOA analysis

The previous sections have shown the basis for an azimuthal dependence of velocity and amplitude in anisotropic media, particularly for the HTI model being considered in this study. This section covers the basic challenges and limitations of the practical application of the AVOA analysis.

### 2.6.1. Orientation ambiguity

The orientation of anisotropy is obtained from equation (2.47) for azimuthally varying reflection coefficient. Only the  $\sin^2$  term will be significant at near offsets as the  $\sin^2 \tan^2$  term is small. This gives the near offset variation of the AVO a  $\cos^2 \phi$  dependence. For longer offset data, the  $\sin^2 \tan^2$  term becomes significant and the variation of the AVO is no longer strictly elliptical (Rüger, 1998; Hall, 2000b).

In order to determine the orientation of anisotropy uniquely, both the sign of the isotropic and anisotropic contributions to the AVO gradient must be known. The difficulty in determining the sign of the anisotropic contribution to the near-offset AVO gradient arises from the non-unique solution to equation (2.50). The solutions yield two orthogonal directions for the symmetry planes (Rüger, 1998). The orientation can be resolved unambiguously by estimating the sign of the anisotropic contribution to the near-offset AVO gradient or through a prior knowledge of the symmetry planes (known fracture orientation) (Rüger, 2002). Additionally, Chichinina et al. (2003) have shown that the sign of the anisotropic contribution to the AVO gradient will be positive provided  $V_S / V_P > 0.56$  (Sabinin, 2008).

The following is a summary of results from Hall, 2000; on constraining the interpretation of AVOA. The  $\cos^2 \phi$  trend may be either positive or negative. Brine filled cracks with a high crack density, very low aspect ratio and low matrix porosity, will show a positive  $\cos 2\phi$  trend (Hall 2000). The  $\cos^2 \phi$  trend is more likely to be negative at near offsets

with increasing medium compliance (gas fill, higher aspect ratio, greater levels of matrix porosity). Crack density is generally observed to affect only the magnitude of anisotropy while preserving the orientation. In the presence of matrix porosity, this effect is increased for gas filled cracks and reduced for brine filled cracks (Hall 2000).

The assumption has traditionally been that the most positive AVO gradient corresponds to the fracture strike. For horizons in which medium properties vary throughout the study area, particularly transitions between gas and brine saturation, the sign of the  $\cos^2 \phi$  term may change. Uncertainty in the sign of the anisotropic contribution to the AVO gradient and non-uniqueness of the least squares solution hinder direct inversion for the orientation of anisotropy. The ambiguity can be resolved through integration with known geology in form of estimated symmetry plane orientations and through modeling the sign of the anisotropic AVO gradient.

### **2.6.2. Attenuation**

Anisotropic attenuation due to fluid flow is described by Hudson (1996) by three relaxation processes: isolated partially saturated cracks, interconnected cracks and communication between cracks and the surrounding matrix porosity. The influence of partially saturated isolated cracks on the azimuthal amplitude response has been found to be negligible at seismic frequencies (Maultzsch et al., 2003). Attenuation from interconnected cracks is seen to increase with decreasing aspect ratio, viscosity and increasing permeability. When these effects are unaccounted for in AVOA analysis, the

orientation of anisotropy will be unaffected but the magnitude will be erroneous. In the case of communication between the cracks and surrounding matrix porosity, for a thick fractured layer, a wide range of porosity and permeability values may produce significant amplitude variations. Amplitude anomalies from fluid flow between cracks and the matrix have been shown, synthetically, to potentially cancel those of the reflection coefficient. If the attenuation from communication between interconnected cracks and matrix porosity is large enough, it may inhibit determination of the symmetry plane orientations and magnitude of anisotropy (Maultzsch et al. 2003).

## **2.7. Transmission effects**

The effects of anisotropy on transmission coefficients are observed to be small in comparison with those of the reflection coefficient. Synthetics studies have shown that for a thick layer the amplitude anomalies are on the order of 2% between the isotropy orientation (fracture strike) and the symmetry axis. For practical application this would indicate that the effect on amplitude analysis will be negligible (Maultzsch et. al. 2003). Modeling for this study has shown that transmission through an anisotropic layer in the overburden produces a small but measurable synthetic AVOA response in the underlying layers (Figure 4.3). However, the magnitude of the anisotropic AVOA gradient term would likely be indistinguishable using field data. The effects of transmission through an overlying anisotropic layer will be more pronounced the more proximal the layer is to the target reflector.

### **2.7.1. Geometric spreading**

Geometric spreading may become problematic for reflection amplitude analysis in the presence of thick anisotropic layers in the overburden with high crack densities and fluid saturation (Maultzsch et al. 2003). Deviation from an isotropic spreading correction is largely model dependent and will increase with crack density and the thickness of the anisotropic layers in the overburden. Error can be minimized by using the velocities of fracture strike direction in the standard isotropic approach or by accounting for the anisotropy in the overburden following Xu (2005, 2008).

### **2.7.2. Multiple fracture sets**

The assumption of a single vertical fracture set (HTI model) greatly reduces the complexity of the AVOA problem by simplifying the stiffness tensor to five terms instead of 9 for orthorhombic symmetry. In reality, orthorhombic symmetry is far more likely to be encountered as fractures often occur in conjugate pairs. The other likely scenario is vertical fractures in horizontally layered media, the combination of HTI and VTI symmetry systems. In either case, orthorhombic symmetry contains two vertical symmetry planes. Analysis of the reflection coefficients in each of the vertical symmetry planes shows a similar solution to that of the symmetry axis (fracture normal) plane in the HTI media. Rüger (1998) expresses the near offset reflection coefficient in terms of modified Thomsen parameters using the solution by Corrigan (1990) for an arbitrary azimuth:

$$R_{pp}(\theta, \phi) = \frac{1}{2} \frac{\Delta Z}{\bar{Z}} + \frac{1}{2} \left\{ \begin{aligned} & \left[ \frac{\Delta \alpha}{\bar{\alpha}} - \left( \frac{\Delta \bar{\beta}}{\bar{\alpha}} \right)^2 \frac{\Delta G}{\bar{G}} \right. \\ & \left. + \left[ \Delta \delta^{(2)} + 2 \left( \frac{2\bar{\beta}}{\bar{\alpha}} \right)^2 \Delta \gamma \right] \cos^2 \phi + \Delta \delta^{(1)} \sin^2 \phi \right] \end{aligned} \right\} \sin^2 \theta, \quad (2.55)$$

$$\delta^{(1)} = \frac{(c_{23} + c_{44})^2 - (c_{33} - c_{44})^2}{2c_{33}(c_{33} - c_{44})},$$

$$\delta^{(2)} = \frac{(c_{13} + c_{55})^2 - (c_{33} - c_{55})^2}{2c_{33}(c_{33} - c_{55})}$$

The reflection coefficient for orthorhombic media is very similar to that of HTI symmetry with the addition of the  $\Delta \delta^{(1)} \sin^2 \phi$  term and differing definitions of  $\delta$  term. Synthetic modeling of the amplitude response from two vertical fracture sets shows a similar azimuthal variation as a single fracture set (Hall 2000). The apparent fracture orientation bisects the acute angle between the fracture sets in the case where the sets are identical. If one set is more compliant, due to the regional stress field, then the AVOA response will appear similar but the apparent orientation will be biased towards the more compliant fracture set. If the inter fracture angle is less than  $40^\circ$  for brine saturation and  $70^\circ$  for gas saturation then it will be difficult to distinguish between a single versus multiple fracture sets (Sayers, 1998; Hall, 2000).

## Chapter 3. Methodology

---

The following chapter provides details of the Weyburn-Midale Phase 1A 2001 3D seismic survey, data processing and AVOA inversion. The survey geometry is assessed to determine the data distribution, select the appropriate bin size and to confirm the absence of bias in the AVOA results. Amplitudes were extracted from the Watrous and cap rock horizons after amplitude preserving pre-processing steps were applied. AVOA inversion is used to determine the magnitude and orientation of anisotropy followed by calculation of uncertainty measures. Anisotropy anomalies are investigated further within the result and discussion chapters.

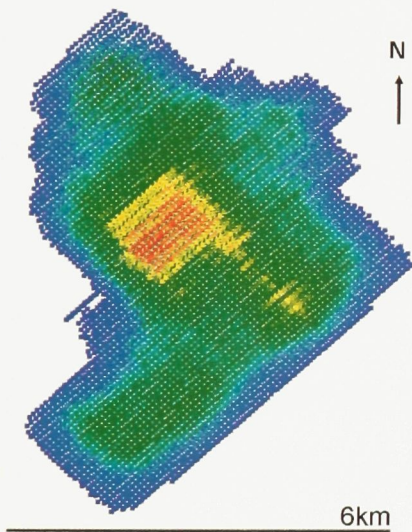
### 3.1. Seismic data

This study uses vertical component seismic data acquired by Tesla during the Weyburn 2001 land 3D seismic survey (Table 3). The dataset contains approximately 155,000 traces acquired over a 6km x 7km area. The survey provides an average fold of 45 in 80x80m bins with higher fold of 60-70 near the center of the study area (Figure 3.1). Fold along the peripheries of the study area ranges from 1-30, often providing insufficient data availability for accurate AVOA inversion. Frequency content ranges from 15-150Hz with dominant frequency of roughly 40hz. Data quality is good out to 1400-1500m offset, after which many of the long offset traces have been muted due to noise.

Table 3.1. Data acquisition parameters for the Weyburn 2001 land 3D seismic survey.

Company	Tesla
Recording instr.	Sn388/ Sercel Eagle 88
Geophones	Oyo UM2
Source	Dynamite, 1kg, depth 12m
Source spacing	160m
Receiver spacing	80m
Source line spacing	160m
Receiver line spacing	160m
Record length	7s
Sample rate	2ms
Number of shots	882
Number of traces	155069
Maximum fold	81

a) 2001 Fold coverage map



b) Offset and azimuth distribution

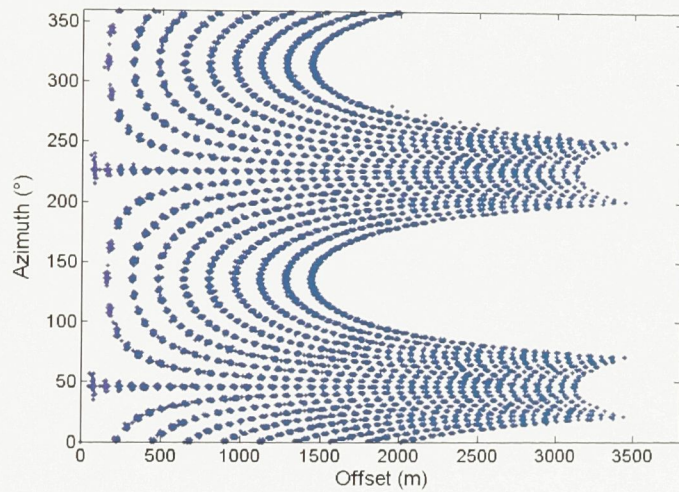


Figure 3.1. Fold coverage and data availability for the Weyburn-Midale Phase 1A field area. (a) Fold coverage map; fold range 1-80, average fold 45 (green). (b) Offset and azimuth distribution. The majority of azimuths are well sampled in the 500-1500m offset range with longer offsets available in the 20-80° and 200-260° azimuth ranges.

### 3.2. Acquisition geometry

AVOA is best performed using a wide distribution of offsets and azimuths. Single 80x80m CMP bins do not provide adequate offset and azimuth sampling (Figure 3.2b). To compensate for this, supergathers are formed centering on the point of interest. In Figure 3.2c,d and e,f, the improved azimuth and offset coverage is shown using 3x3 and 5x5 CMP supergathers, respectively. Previous studies (Luo & Evans, 2004) have shown that supergather bin size on the order of the first Fresnel zone radius are acceptable. The Fresnel-zone radius is approximated by

$$r = \sqrt{\frac{z_0 \lambda}{2}}, \quad (3.1)$$

where  $r$  is the radius,  $z_0$  is the depth of the reflector and  $\lambda$  is the dominant wavelength of the wavefront. For RMS velocities between 3000m/s and 3500m/s and dominant frequencies between 50Hz and 70Hz, the Fresnel-zone radius varies between 170m and 220m. The larger 5x5 supergather half width is 200m while the smaller 3x3 supergather width is 120m. Using the larger 5x5 CMP supergather provides significantly improved offset and azimuth coverage at the expense of reduced horizontal resolution.

The acquisition geometry using the 5x5 supergather provides sufficient azimuthal coverage in the 500-1500m offset range. Given a target depth of  $\sim 1400$ m, this offset range is suitable for the near-offset AVO approximation. Longer offset data are available in the 20-80° azimuth range, however, the data quality was too poor to include in the inversion.

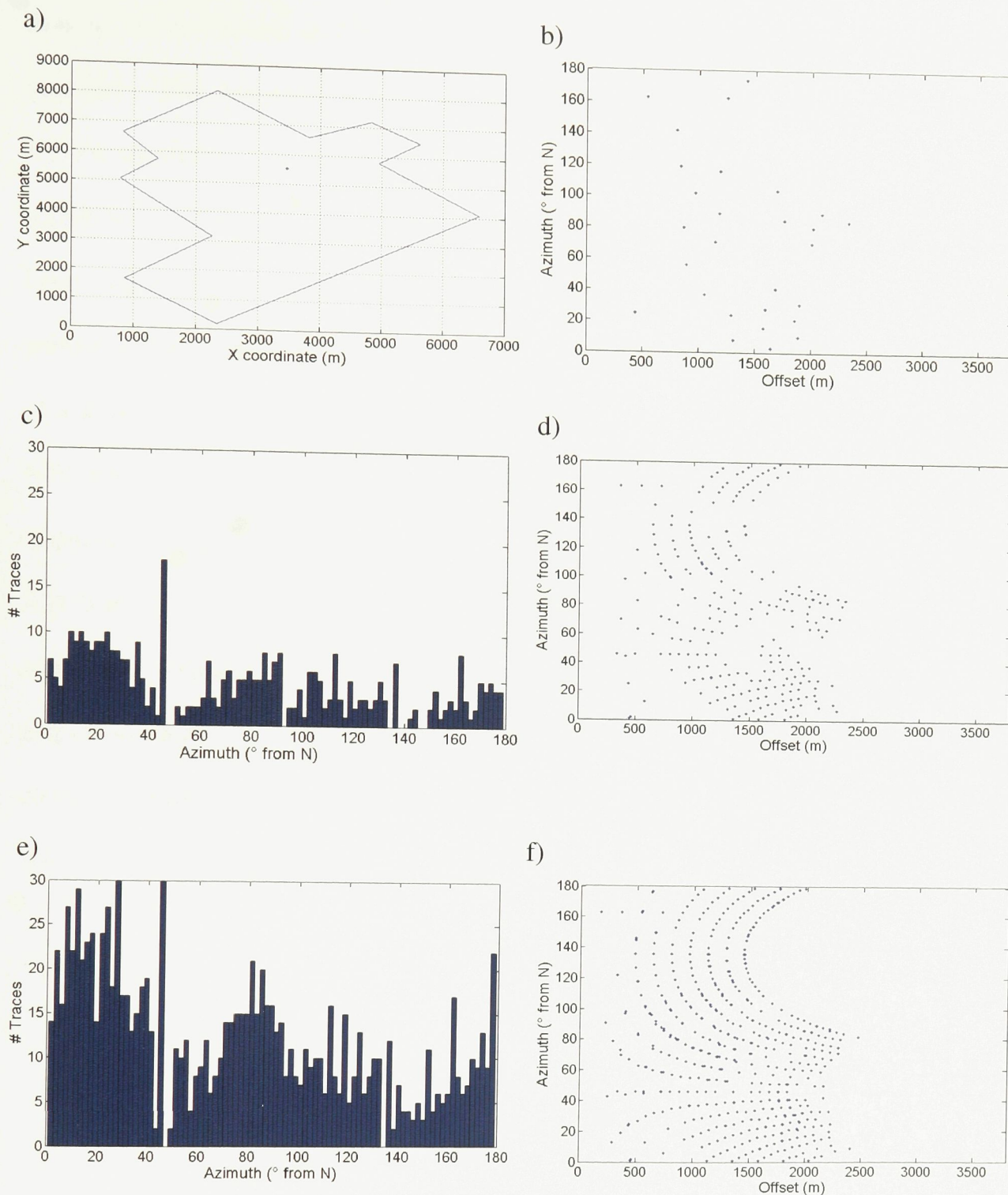
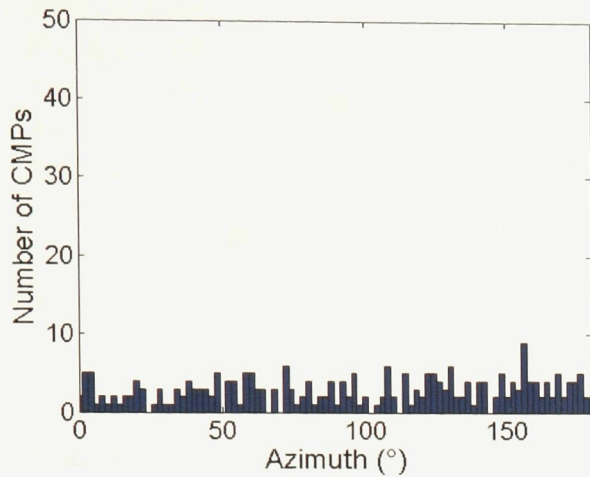


Figure 3.2. Example of offset and azimuth distribution for a sample CMP and CMP supergather. a) Location of CMP point, CDP# 88712 b) Offset and azimuth distribution for single CMP, fold 41. c) Histogram of azimuth distribution for 3x3 supergather,  $2^{\circ}$  bins. d) Offset and azimuth distribution for 3x3 supergather. e) Histogram of azimuth distribution for 5x5 supergather,  $2^{\circ}$  bins. f) Offset and azimuth distribution for 5x5 supergather. The majority of  $2^{\circ}$  azimuth bins contain 5 traces or more in the 5x5 supergather, whereas the 3x3 supergather contains gaps with 5 traces or less over a  $10^{\circ}$  azimuth range.

Bias in the orientation of the AVOA response can be introduced from the acquisition geometry. The potential for biasing is assessed by loading the field geometry into the AVOA algorithm and simulating a series of amplitude trends. Both isotropic and anisotropic AVO trends were tested with and without up to 20% random variation in input amplitudes. For an isotropic AVO curve with added noise, there should be no preferred alignment of the AVO. The orientations which are determined through fitting of a sinusoid to the noise should appear random over the field area. For an anisotropic AVO curve with a preferred orientation, the acquisition geometry should not introduce magnitude anomalies or bias the orientation of the anisotropy. Tests have shown (Figure 3.3) that the surface fitting approach to the AVOA inversion is not biased by the acquisition geometry. When a preferred AVO orientation is used with up to  $\pm 10\%$  amplitude variation, both the sectoring and surface fitting approaches picked out the correct azimuth. Surface fitting provided a higher degree of accuracy in determining the orientation and appeared less prone to outliers.

a) Synthetic AVO, no anisotropy



b) Synthetic AVO with anisotropy oriented at 20°

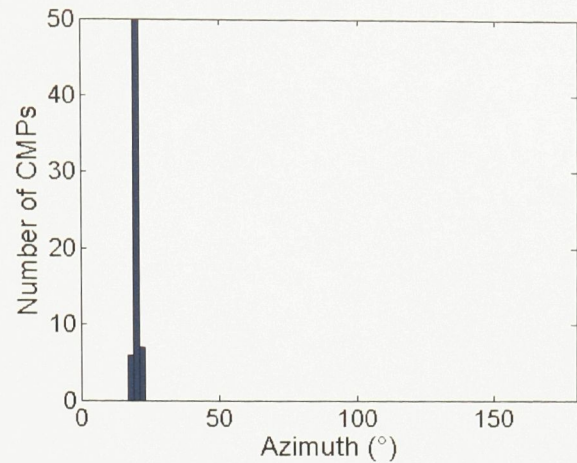


Figure 3.3. Sensitivity of the orientation of anisotropy to the field geometry. In each figure a sub-set of the field geometry from the center of the study area is used. a) A constant AVO gradient with up to  $\pm 10\%$  variation in the synthetic amplitudes produces a scatter of orientations without bias towards the acquisition geometry orientation. b) Anisotropy orientations using a constant synthetic AVOA trend oriented at  $20^\circ$  with synthetic amplitudes varying by up to  $\pm 10\%$ .

### 3.3. Processing

Amplitude preserving pre-processing steps were applied to the field data (e.g., Jenner, 2001; Yilmaz, 2001; Hall & Kendall, 2003). Mutes were applied between 1500-1700m offset at the target time of roughly 1150ms. A  $t^2$  correction was applied to correct for geometric spreading. Surface-consistent source-receiver amplitude balancing (Figure 3.5) and deconvolution were applied, followed by a bandpass filter. Both muted and unmuted datasets were produced, the short offset amplitudes were found to be more stable in comparison with the un-muted, long-offset dataset. A schematic of the processing flow is shown in Figure 3.4.

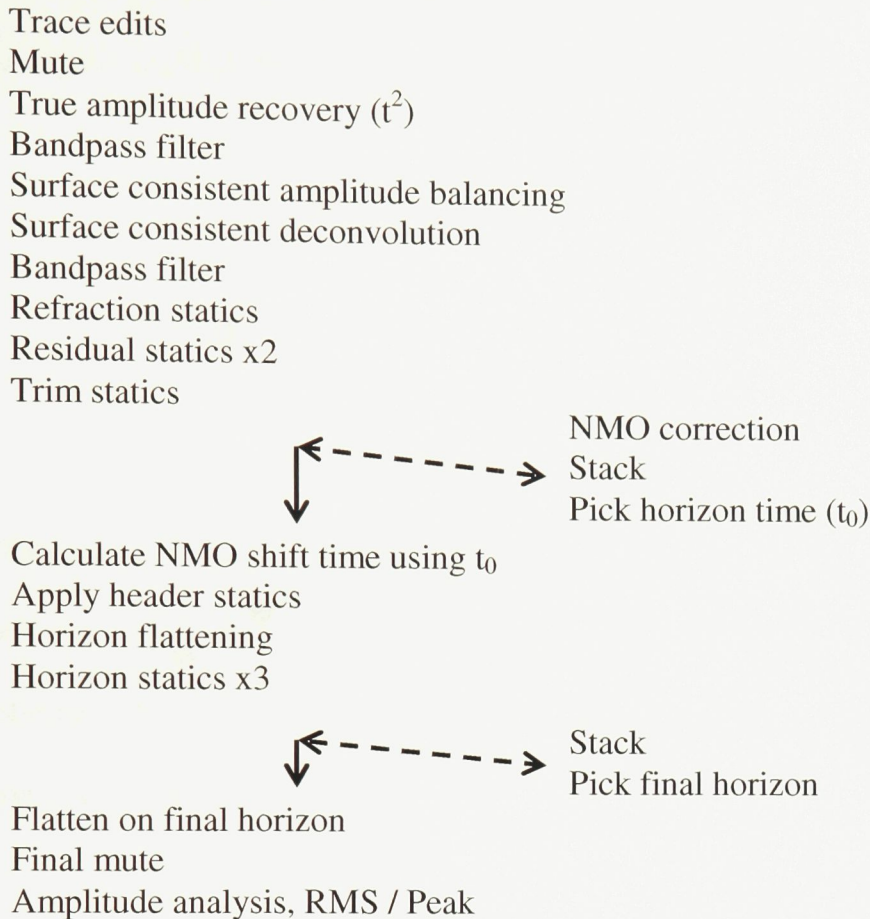


Figure 3.4 True amplitude processing sequence applied for each horizon of interest. Horizon time picks ( $t_0$ ), NMO and stacking were performed to obtain database parameters and are omitted from the final processing sequence.

The instantaneous peak amplitude and the RMS amplitude within a narrow (15ms) window over the target horizon were extracted. The RMS amplitude was found to provide more stable results when compared with the peak amplitude.

Prior to amplitude extraction, the horizons are flattened without NMO stretch. This process is performed by calculating the difference between the two-way travel time and the zero-offset time,  $t_0$ , and applying a time shift. The  $t_0$  time is obtained by flattening the horizon using an isotropic NMO correction and picking the horizon in the stacked

seismic section. The two-way travel time is then calculated using Eqn. (3.2). The incidence angle at the target horizon is approximated (Yilmaz, 2001):

$$t^2 = t_o^2 + \frac{x^2}{v_{rms}^2} \quad (3.2)$$

$$\frac{d_t}{d_x} = \frac{1}{v_{rms}^2} \frac{x}{t} \quad (3.3)$$

$$\sin \theta = \frac{v_{int}}{v_{rms}} \frac{x}{t} \quad (3.4)$$

Where  $x$  is the source-receiver offset,  $t$  is the two-way traveltime,  $t_0$  is the zero-offset two-way travel time,  $v_{int}$  is the interval velocity and  $v_{rms}$  is the RMS velocity down to the reflection horizon. An approximate RMS velocity of 2700m/s was used based on previous studies (Jenner, 2001).

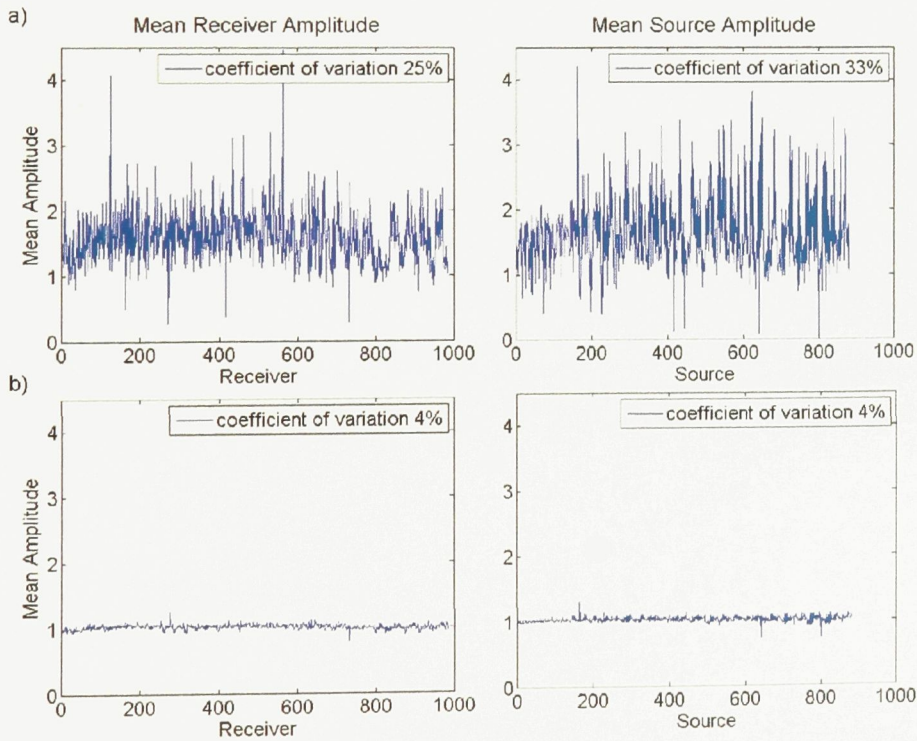


Figure 3.5 Surface consistent source-receiver amplitude balancing. a) Mean source and receiver amplitudes pre-balancing are highly variable indicating differing ground conditions (wet vs. dry) or possible coupling issues.

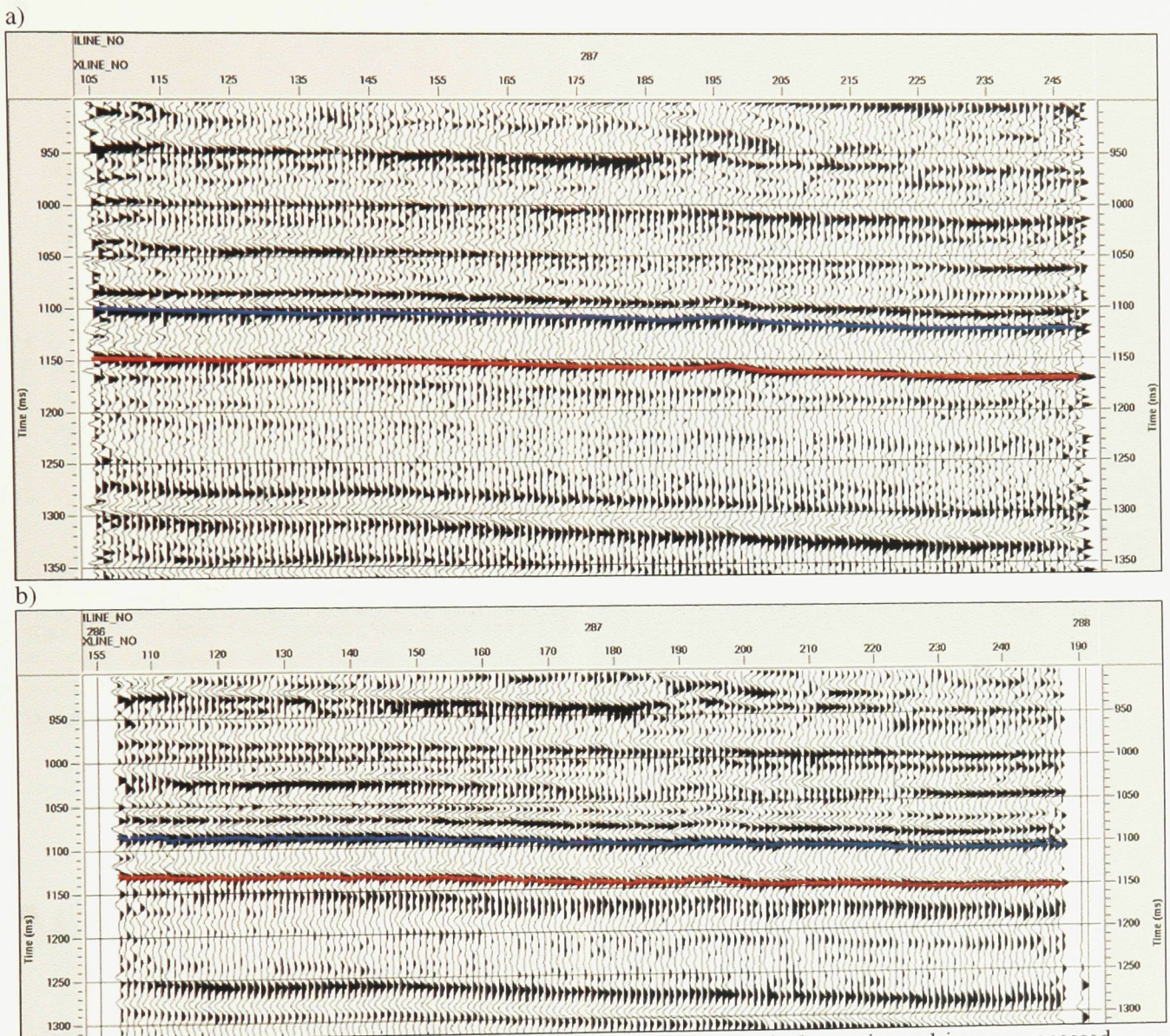


Figure 3.6 Stack comparison between, a) the provided Sensor Geophysical un-migrated image processed dataset and b) true amplitude processed dataset for this study. The isotropic NMO correction applied for stacking was not applied during amplitude analysis. Watrous horizon, blue line, cap rock horizon red line. A good match between the true amplitude processed stack and image processed stack is observed.

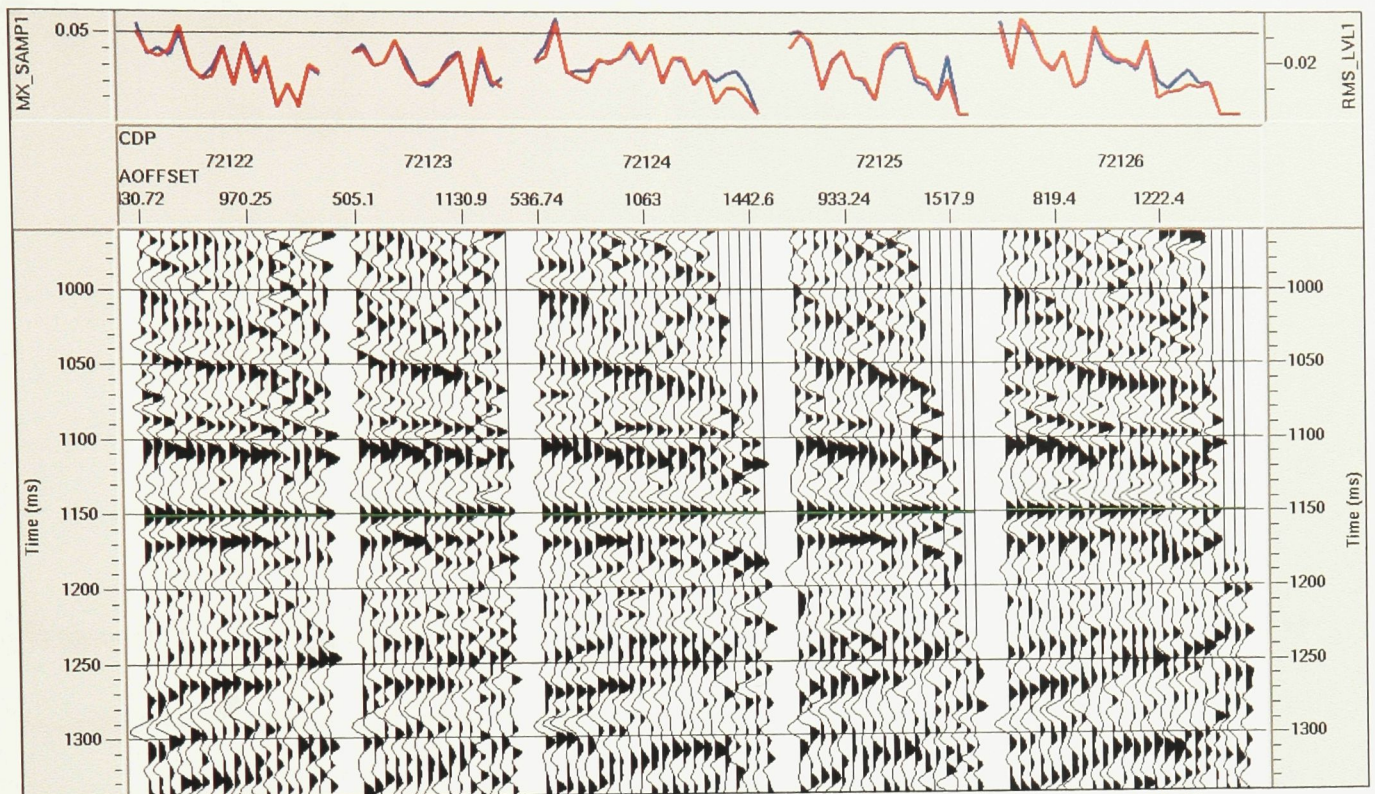


Figure 3.7. Sample CMP gathers after processing showing the cap rock horizon with extracted RMS and peak amplitudes plotted above. Longer offsets (>1450m) are often muted out due to higher levels of noise and inconsistencies in the reflection horizons. The horizon has been flattened using the equivalent time shift for a NMO correction to avoid NMO stretch.

### 3.4. AVOA inversion

AVOA was performed on 5x5 CMP supergathers at every second CMP position (160m spacing). A linear regression of amplitudes was fit to the near-offset approximation for the P-P reflection coefficient,  $R_{pp}$ , using a horizontal transverse isotropy (HTI) model (Rüger, 1998; Hall, 2000; Jenner, 2001; Hall and Kendall, 2003):

$$R_{pp}(\theta, \phi) = A + (G_{iso} + G_{aniso} \cos^2(\phi - \phi_{sym})) \sin^2 \theta \quad (3.5)$$

$$R_{pp}(\theta, \phi) = A + (w_{11} \cos^2 \phi + 2w_{12} \cos \phi \sin \phi + w_{22} \sin^2 \phi) \sin^2 \theta \quad (3.6)$$

$$\begin{aligned} G_{iso} &= \frac{1}{2} \left( w_{11} + w_{22} - \sqrt{(w_{11} - w_{22})^2 + 4w_{12}^2} \right) \\ G_{aniso} &= \sqrt{(w_{11} - w_{22})^2 + 4w_{12}^2} \\ \beta &= \tan^{-1} \left[ \frac{w_{11} - w_{22} + \sqrt{(w_{11} - w_{22})^2 + 4w_{12}^2}}{2w_{12}} \right] \end{aligned} \quad (3.7)$$

Where  $\theta$  is the incidence angle,  $\phi$  is the azimuth and  $\beta$  is the angle between the coordinate system and either symmetry axis. The  $w_{ij}$  coefficients are used to recover the isotropic and anisotropic contributions to the near-offset AVO gradient, denoted  $G_{iso}$  and  $G_{aniso}$ , respectively. The orientation of the maximum AVO gradient is determined by  $\beta$ , which is not necessarily the fracture strike direction.

Both azimuthal sectoring and surface fitting inversions were performed. The method of azimuthal sectoring is performed using a two step inversion process. The first step calculates the AVO gradient within each azimuth bin and the second step determines the azimuthal variation of the AVO gradient (Figure 3.8a,b). Since the intercept, 'A' equation (3.6), does not depend on azimuth, it should be similar for each azimuth bin. In practice, solving for the intercept at each azimuth bin will produce a range of values depending on the scatter in the extracted amplitudes. The variation in intercept values between azimuth bins was removed by calculating the intercept using amplitudes from the whole CMP gather. Checks were performed on each AVO fit to ensure a minimum of 8 traces were used. The standard error of the estimate (RMSE) is also calculated and

used as the error value on each gradient point when calculating the gradient variation with azimuth. The RMSE and goodness of fit are then determined for the gradient variation with azimuth. Inversion by azimuthal sectoring was found to be sensitive to azimuth bin size and the limited number of sample points used in the calculation.

Surface fitting (Figure 3.8c) allows the determination of the AVOA coefficients using all amplitudes at their correct offset and incidence angle without binning (Jenner, 2001). Each trace amplitude is equally weighted in this approach, however, the traces are not evenly distributed in offset and azimuth due to the survey geometry. The RMS error and goodness of fit can be determined for the surface fit similar to the azimuthal sectoring approach. Determining the uncertainty of the AVO gradient uses the uncertainty in the  $w_{ij}$  coefficients from equation (3.6) and the propagation of uncertainty through equation (3.7).

Azimuthal sectoring was found to be more sensitive to regions of lower data availability. Surface fitting provided smoother transitions between CMP positions in terms of anisotropy orientation and was less prone to outliers. Attempts were made to stabilize and improve the inversion by using longer offset data, these data were found to be noisy and offered no significant improvement. The orientation and magnitude of anisotropy in the near-offset AVOA were then plotted as vectors to identify and interpret any possible trends at the cap rock level. A similar procedure was followed for the Watrous horizon, immediately above the cap rock.

### 3.5. Uncertainty

Mapping the distribution and magnitude of uncertainty aids in interpreting the validity of anisotropy anomalies and provides a spatial measure of data quality. Uncertainty in the magnitude of anisotropy is determined using the propagation of error of the standard errors of the  $w_{ij}$  coefficients through equation (3.7). The standard error of the  $w_{ij}$  coefficients is determined as follows.

$$Y = \begin{bmatrix} R_{pp_1} \\ \vdots \\ R_{pp_n} \end{bmatrix}, X = \begin{bmatrix} 1 & \cos^2 \phi_1 \sin^2 \theta_1 & 2 \cos \phi_1 \sin \phi_1 \sin^2 \theta_1 & \sin^2 \phi_1 \sin^2 \theta_1 \\ & & \vdots & \\ 1 & \cos^2 \phi_n \sin^2 \theta_n & 2 \cos \phi_n \sin \phi_n \sin^2 \theta_n & \sin^2 \phi_n \sin^2 \theta_n \end{bmatrix} \quad (3.8)$$

The least squares estimators are determined by:

$$v = \begin{bmatrix} \hat{A}_0 \\ \hat{w}_{11} \\ \hat{w}_{12} \\ \hat{w}_{22} \end{bmatrix} = (X^T X)^{-1} (X^T Y) \quad (3.9)$$

Where T is the transpose. First we need to determine the variance,  $s^2$ :

$$s^2 = \frac{1}{n-k-1} \hat{\epsilon}^T \hat{\epsilon} \quad (3.10)$$

where  $n$  is the length of  $Y$  and  $k$  is 3.

$$\hat{\epsilon} = Y - \hat{Y} \quad (3.11)$$

where,

$$\hat{Y} = Xv = \begin{bmatrix} 1 & \cos^2 \phi_1 \sin^2 \theta_1 & 2 \cos \phi_1 \sin \phi_1 \sin^2 \theta_1 & \sin^2 \phi_1 \sin^2 \theta_1 \\ & & \vdots & \\ 1 & \cos^2 \phi_n \sin^2 \theta_n & 2 \cos \phi_n \sin \phi_n \sin^2 \theta_n & \sin^2 \phi_n \sin^2 \theta_n \end{bmatrix} * \begin{bmatrix} \hat{A}_0 \\ \hat{w}_{11} \\ \hat{w}_{12} \\ \hat{w}_{22} \end{bmatrix} \quad (3.12)$$

To determine the standard error of the first regression coefficient:

$$s_{\hat{a}} = \sqrt{s^2 * [1 \ 0 \ 0 \ 0] * (X^T X)^{-1} * \begin{bmatrix} 1 \\ 0 \\ 0 \\ 0 \end{bmatrix}} \quad (3.13)$$

Similarly for the second,  $w_{11}$  and so on:

$$s_{\hat{w}_{11}} = \sqrt{s^2 * [0 \ 1 \ 0 \ 0] * (X^T X)^{-1} * \begin{bmatrix} 0 \\ 1 \\ 0 \\ 0 \end{bmatrix}} \quad (3.14)$$

Once the standard errors are determined, a propagation of error through equation (3.7) is performed to determine the uncertainty of the magnitude of anisotropy.

$$\delta G_{aniso} = \sqrt{\left( \frac{\partial G_{aniso}}{\partial w_{11}} \delta w_{11} \right)^2 + \left( \frac{\partial G_{aniso}}{\partial w_{12}} \delta w_{12} \right)^2 + \left( \frac{\partial G_{aniso}}{\partial w_{22}} \delta w_{22} \right)^2} \quad (3.15)$$

$$\begin{aligned} \frac{\partial G_{aniso}}{\partial w_{11}} &= \frac{w_{11} - w_{22}}{\sqrt{(w_{11} - w_{22})^2 + 4w_{12}^2}} \\ \frac{\partial G_{aniso}}{\partial w_{12}} &= \frac{4w_{12}}{\sqrt{(w_{11} - w_{22})^2 + 4w_{12}^2}} \\ \frac{\partial G_{aniso}}{\partial w_{22}} &= -\frac{w_{11} - w_{22}}{\sqrt{(w_{11} - w_{22})^2 + 4w_{12}^2}} \end{aligned} \quad (3.16)$$

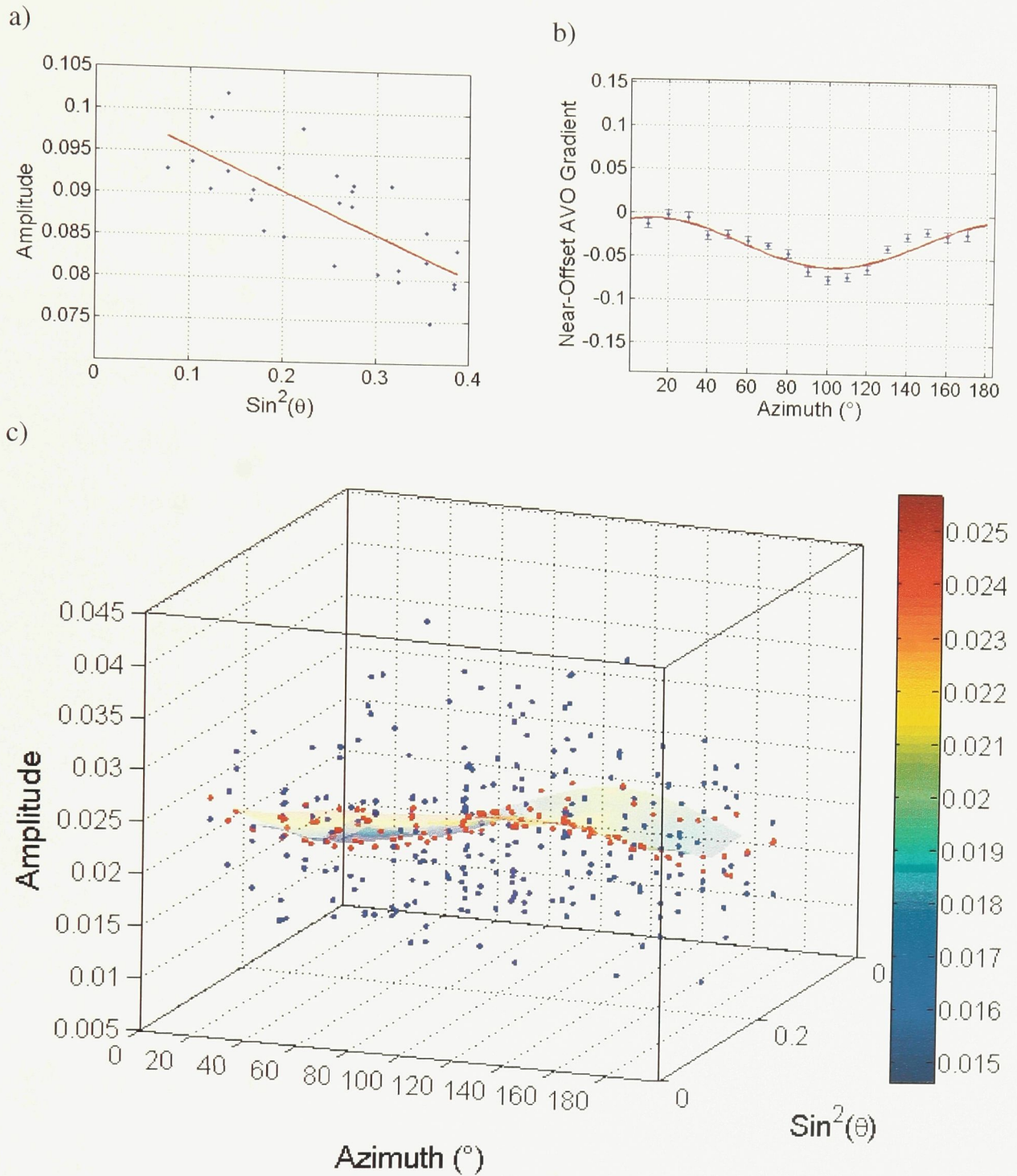


Figure 3.8 The methods of azimuthal sectoring, a) and b), and surface fitting, c), for AVOA. Synthetic amplitudes with up to 10% deviation in input amplitude are used for demonstration. a) The AVO gradient (red line) is calculated for each azimuth bin. b) The gradient from each azimuth bin is plotted at the bin center and the anisotropy magnitude and orientation are determined. c) A linear least squares regression of amplitudes is performed to determine the magnitude and orientation of anisotropy.

## Chapter 4. Modeling

---

Modeling of the synthetic seismic reflection amplitude response is conducted to better constrain the interpretation of anisotropy observed in the Weyburn-Midale field data. Previous studies (e.g., Hall and Kendall, 1997, 2003; Mallick et al., 1998; Rüger, 1998; Hall, 2000) have shown that the interpretation of the orientation of anisotropy depends on properties of the medium at the reflection interface. Ambiguity between the directions of fracture strike and fracture normal can be resolved through modeling of the anisotropic AVO response. Modeling studies are performed on synthetic 3D CMP gathers to determine the expected magnitude of anisotropy from the cap rock and to assess the feasibility of differentiating anisotropy from the cap rock from that of surrounding layers. The cap rock layer is thin (10-30m), which introduces the possibility that interference of reflections from the underlying reservoir (known to be fractured) may contribute to observed anisotropy at the cap rock horizon. This possibility is explored through modeling of the interference between reflections from the top of the cap rock, upper and lower reservoir layers.

### 4.1. Geologic model

A simplified earth model was constructed based on a combination of well logs and previous thesis studies from the Colorado School of Mines Reservoir Characterisation Project (Bunge, 2000; Jenner, 2001; Brown, 2002). The isotropic values used for thickness, density, P-wave velocity and S-wave velocity are listed in Table 1. The anisotropic parameters used are from Bunge (2000) and Brown (2002), and include the

crack density and aspect ratio from a combination of core samples and EMI logs. The average crack density values for the reservoir have been determined by Brown (2002) to be 0.03 for the Marly and 0.1 for the Vuggy. These values were used for the range of potential crack densities in the overlying cap rock, Watrous and overburden layers. The overburden is considered to be the column of strata overlying the Watrous horizon. For modeling purposes a 50m thick modeling layer (isotropic / anisotropic) (Table 3), is introduced in the overburden with similar isotropic properties to the Watrous. This layer is made anisotropic in order to test for the effects of anisotropy in an overlying layer.

Table 3. Earth model used to model the synthetic AVOA response. Modeling layers were used to study the influence of possible anisotropy in the overburden. The Watrous layer was made anisotropic to test for the effects of anisotropy immediately above the cap rock.

Model Layer	Depth (m)	Vp (m/s)	Vs (m/s)	$\rho$ (kg/m <sup>3</sup> )
Overburden	0	3125	1840	2300
Modeling Layer (iso/aniso)	750	3920	2170	2560
Modeling Layer	800	3125	1840	2300
Watrous	1325	3920	2170	2560
Cap rock	1400	5400	3375	2780
Marly	1420	4000	2200	2420
Vuggy	1430	5130	2800	2480



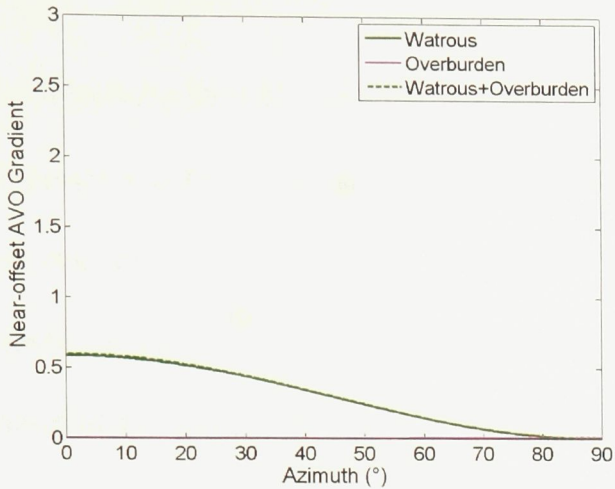
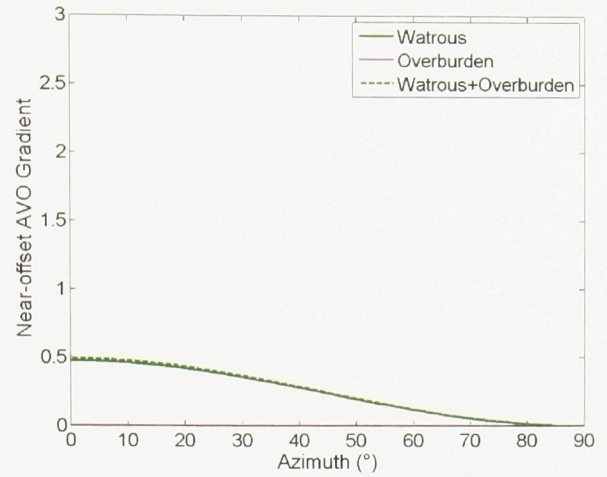
Figure 4.1 Diagram of the 7 layer earth model used to produce synthetic AVOA response at the Watrous, cap rock and reservoir horizons. Physical properties for the layers are listed in Table 3. Note the non-linear depth scale.

The anisotropic medium parameters are entered into the ray tracing software as stiffness tensor components using the HTI symmetry system and the Hudson (1981) “penny-shaped cracks” model. The  $C_{ij}$  tensor components are calculated using the CIJStan program by Hall (2000). Ray tracing software ATRAK (Guest and Kendall, 1993) was used with a 50Hz Ricker wavelet source to produce synthetic CMP gathers at 30° azimuth intervals. Basic pre-processing steps were applied (*e.g.*, spreading correction) and the AVOA algorithm was used to calculate the orientation and magnitude of the near-offset AVO gradient for several model scenarios.

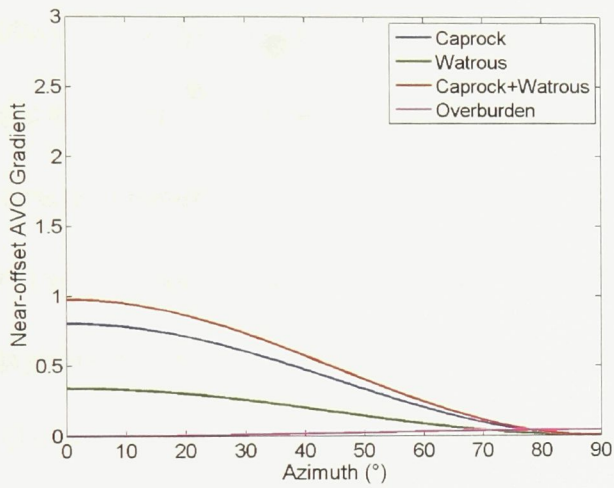
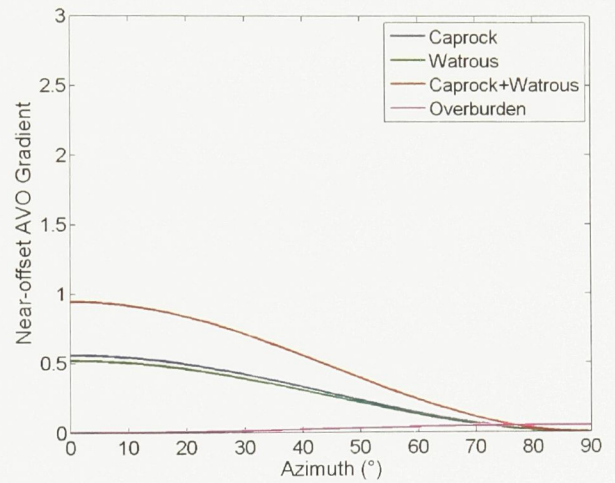
## 4.2. Single interface modeling

Single interface modeling is performed to assess the relative magnitudes of anisotropy in the near-offset AVO gradient and to determine the orientation of anisotropy for each layer. The effects of anisotropy in overlying layers are also considered. The RMS amplitude within a 15ms window from the top of the cap rock, reservoir and Watrous layers are extracted from synthetic traces. The amplitudes and their corresponding incidence and azimuth angles are used to solve for the magnitude and orientation of anisotropy at each interface. The results for each interface are summarized in Figure 4.2. Anisotropy in the Watrous is observed to produce a measurable AVOA response at the Watrous, cap rock and reservoir horizons. Anisotropy in the cap rock produces the largest AVOA response in each of the single layer, single interface tests. Multiple aligned anisotropic layers produce a larger anisotropic response, however the magnitude increase is not linear. Without prior knowledge, inversion provides the direction of maximum AVO gradient as the orientation of anisotropy or the fracture strike. The maximum AVO gradient is observed to occur along the fracture strike for the cap rock and Watrous layers and along the fracture normal for the reservoir. If observed anisotropy is from the reservoir, the orientation of the fracture strike will vary by  $90^\circ$ . Anisotropy resulting from the cap rock will have the correct orientation. Ambiguity in the origin of anisotropy introduces an additional level of uncertainty in the orientation of anisotropy.

a) Top of the Watrous, brine fill

b) Top of the Watrous, CO<sub>2</sub> fill

c) Top of the cap rock, brine fill

d) Top of the cap rock, CO<sub>2</sub> fill

e) Top of the reservoir, brine fill

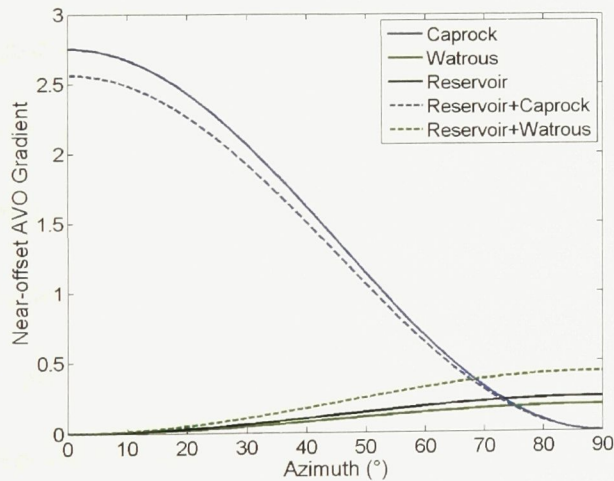
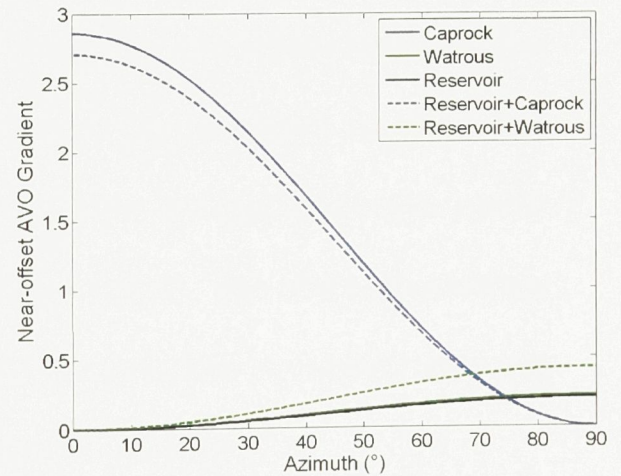
f) Top of the reservoir, CO<sub>2</sub> fill

Figure 4.2 Relative magnitudes of the near-offset AVO gradient for model layers of interest. Dashed lines represent anisotropy in multiple layers, e.g the reservoir and cap rock. All cases are for crack density of 0.1 a) Watrous, brine crack fill. b) Watrous, gas fill. c) cap rock, brine fill. The red line represents anisotropy in both the Watrous and cap rock d) cap rock, gas fill. The red line represents anisotropy in both the Watrous and cap rock e) reservoir, brine fill. f) reservoir, gas fill.

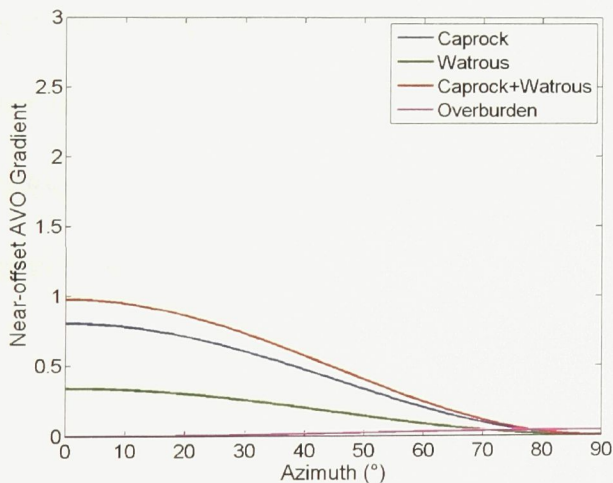
### 4.2.1. Crack fill material

The Weyburn-Midale field has undergone both water flood and CO<sub>2</sub> injection. These processes create a range of possible crack fill materials which will affect the magnitude and potentially orientation of the AVOA response. Stiffness tensor components are dependent on the properties of the material filling the fractures. Modeling considers two possibilities, gas (CO<sub>2</sub>) and brine fill material. Gas fill is considered pure CO<sub>2</sub> at reservoir pore pressure and temperature of 15MPa and 62°C respectively (Whittaker, 2004). Gas fill, for the cap rock horizon, results in similar synthetic magnitudes of anisotropy for an anisotropic cap rock and an anisotropic Watrous, using identical fracture properties (Figure 4.2d). These results suggest it will not be possible to distinguish anisotropy in the cap rock from the overlying Watrous based on the magnitude from a single horizon, for the case of gas fill. Brine fill provides considerably different values of anisotropy for the cap rock and Watrous horizons. These values suggest it may be possible to differentiate between anisotropy in the two horizons by filtering points of higher and lower magnitude and comparing with results from overlying horizons in the case of brine fill. If both the cap rock and Watrous layers are anisotropic with similar orientation and fracture properties, both brine and gas fill provide similar values for anisotropy measured at the cap rock (Figure 4.2c,d). The effect of anisotropy in an overburden layer for either gas or brine fill is measurable in synthetics but not expected to significantly impact the results when noise is considered.

## 4.2.2. Crack density

Crack density has the greatest impact on the magnitude of anisotropy while preserving the orientation of the maximum AVO response. Modeling studies were performed using representative values; a lower value of crack density from the Marly reservoir and an upper value from the Vuggy reservoir (0.03) and (0.1). Amplitudes are determined at the cap rock horizon and the magnitude of the near-offset AVO gradient is compared for the two crack densities. Modeling shows that higher crack density will provide larger values of anisotropy in the near-offset AVO gradient (Figure 4.3). In the case of the lower crack density, it is questionable whether the cap rock could be differentiated from the Watrous based on magnitude when noise is present. The effect of anisotropy in an overburden layer is greater for the higher crack density, but does not significantly impact the results in either case.

a) Top of the cap rock, crack density 0.1 (Vuggy)



b) Top of the cap rock, crack density 0.03 (Marly)

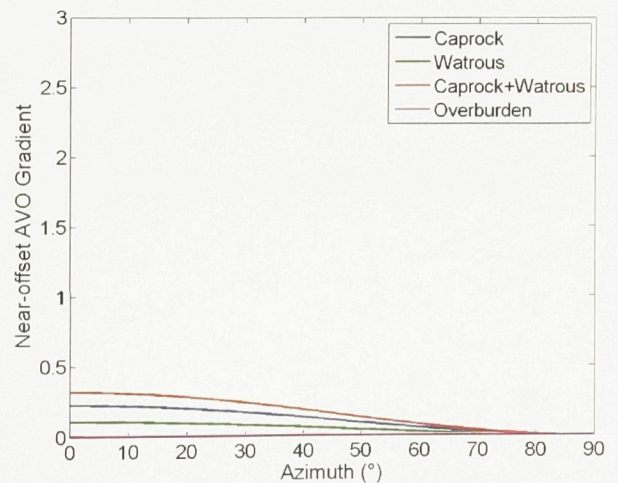


Figure 4.3 Near-offset AVO gradient response for the top of the cap rock. Curves are shown for anisotropy in a given layer, cap rock (blue), Watrous (green), overburden (magenta), both cap rock and watrous layers anisotropic (red). a) Response for crack density 0.1 equivalent to the lower Vuggy reservoir. b) Response for crack density 0.03 equivalent to the upper Marly reservoir. The higher crack density is seen to produce a larger magnitude of anisotropy for all case.

### 4.3. Multi-Layer thickness and interference

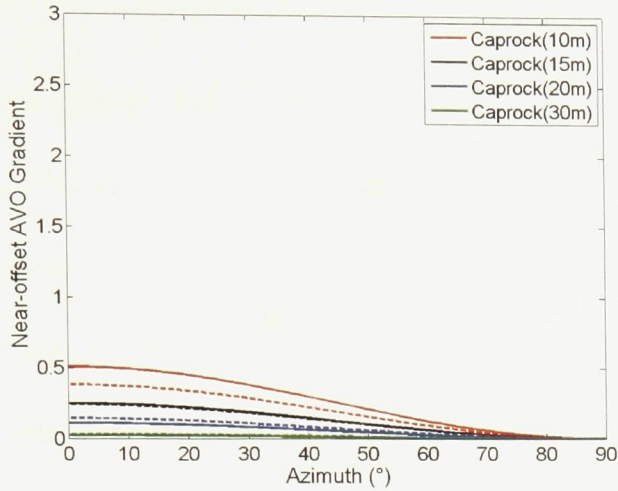
The effects of multiple thin layers and layer thickness on the near-offset AVO gradient are an important issue for the Weyburn-Midale study area. The cap rock interval produces a prominent reflection horizon, however, the thickness of both the cap rock and the underlying reservoir layers vary. Modeling is performed to assess the effects of layer thickness on the anisotropic response of the cap rock and reservoir. The effects of interference at the cap rock horizon from the underlying reservoir, known to be anisotropic, are also considered. Layer thickness is varied between the maximum and minimum observed values in the study area. Two cases are considered.

The first case models the response of an isotropic cap rock with an underlying anisotropic reservoir (Figure 4.4 a,c). The cap rock should produce an isotropic AVO response, however, we observe increasing anisotropy with a progressively thinner cap rock. The modeling suggests that we should expect to observe interference from the underlying reservoir where the combined cap rock interval is less than 20m thick. A slight anisotropy is observed at 30m thickness, however the magnitude would be negligible in the presence of noise.

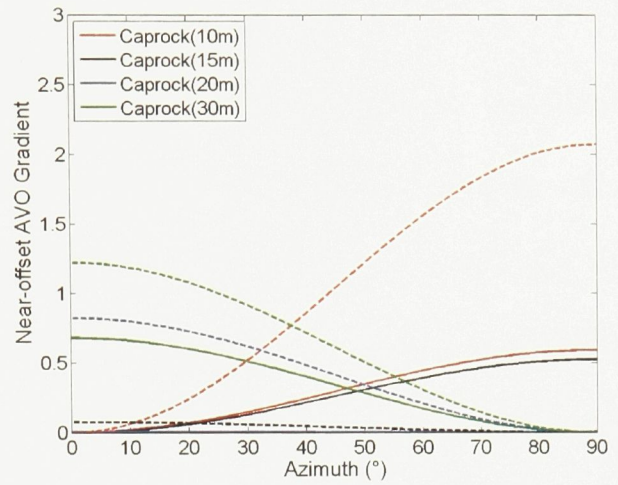
The second case considers the response of both an anisotropic cap rock and reservoir for varying layer thickness (Figure 4.4 b,d). Where the cap rock is thin, the synthetic seismic response deviates from the near-offset HTI model. Increasing RMS error and decreasing

correlation of the amplitudes to the near-offset HTI model are observed with progressively thinner cap rock and reservoir layers. These results indicate that in the presence of a thin, anisotropic cap rock and reservoir, the estimation of magnitude and orientation of anisotropy will be unreliable. Limiting the modeling results to those with 95% correlation or better, we observe that the magnitude and orientation of the cap rock response is reliable, in synthetics, for cap rock interval thickness of 20m and 30m. Comparing the response of an isotropic cap rock (Figure 4.4a) against an anisotropic cap rock (Figure 4.4b), the magnitude of anisotropy is more than double the isotropic case. This suggests it will be possible to identify anisotropy in the cap rock based on magnitude anomalies, provided the cap rock is greater than 20m thick and without interference from overlying anisotropic layers.

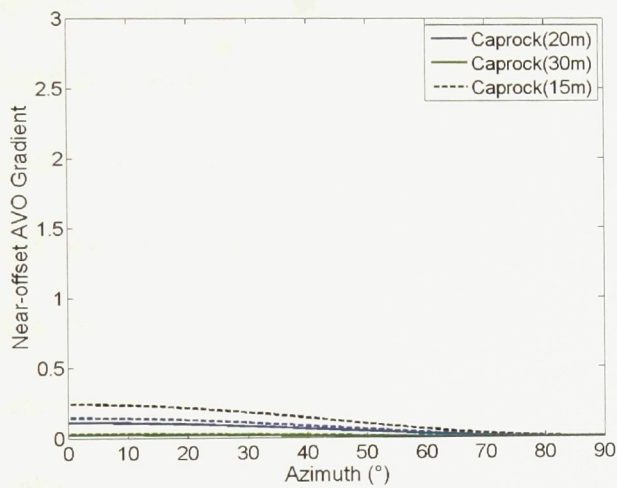
a) Multiple thin layers, isotropic cap rock



b) Multiple thin layers, anisotropic cap rock



c) Results from a) matching 95% model correlation



d) Results from b) matching 95% model correlation

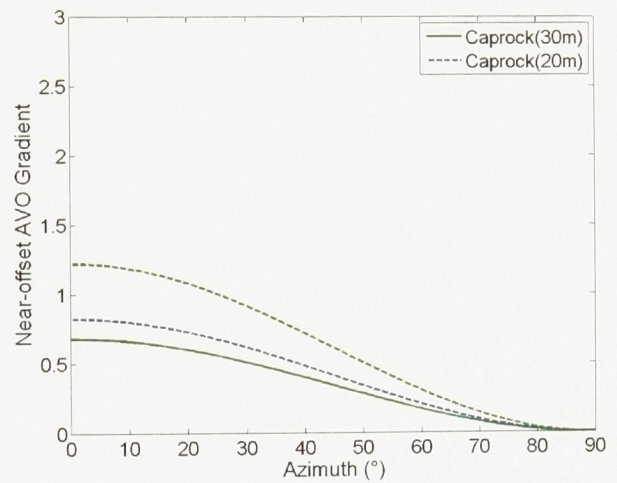


Figure 4.4 Near-offset AVO gradient response at the cap rock horizon for several model layer thicknesses. Cap rock thickness varies from 10m (red), 15m (black), 20m (blue) to 30m (green). Reservoir thickness varies between 5m (dashed line) and 10m (solid lines). a) Isotropic cap rock with underlying anisotropic reservoir layers. b) Anisotropic cap rock with underlying anisotropic reservoir. c) Isotropic cap rock with underlying anisotropic reservoir, filtered to 95% correlation between amplitudes and near-offset HTI model response. d) Anisotropic cap rock with underlying anisotropic reservoir, filtered to 95% correlation between amplitudes and near-offset HTI model response.

#### 4.4. Modeling conclusions

Modeling studies have provided synthetic magnitudes of anisotropy in the near-offset AVO gradient for the horizons of interest. The presence of anisotropy in the cap rock is observed to produce the largest synthetic AVOA response for all modeling scenarios. Anisotropy in the Watrous, when observed at the cap rock horizon, produces a significant response in all cases. In the case of gas crack fill, anisotropy in the Watrous layer produces a response comparable to the cap rock horizon. This suggests it would not be possible to differentiate, based on magnitude, anisotropy in the Watrous from the cap rock if anisotropy is present in either layer for gas crack fill. Increasing crack density is observed to increase the magnitude of the anisotropic response while preserving the orientation of the maximum near-offset AVO gradient. Higher values of crack density provide a greater separation in the response of different layers. It is questionable in the case of lower crack density if the cap rock could be differentiated from the Watrous in the presence of noise. Interference from the underlying anisotropic reservoir can be expected if the combined cap rock interval is less than 20m thick. Where the cap rock interval is greater than 20m thick, modeling suggests anisotropy anomalies in the cap rock may be differentiated from those of the reservoir based on magnitude. When considering the response of multiple thin layers of varying thickness, an anisotropic cap rock will produce the largest magnitude of anisotropy. Where the cap rock interval is less than 20m thick, deviations from the HTI model occur in the near-offset AVO gradient. This suggests that higher levels of uncertainty will be observed in the magnitude and orientation of anisotropy in the presence of multiple thin (<20m) layers.

## Chapter 5. Results

---

This chapter presents results of amplitude inversion for two sealing units, the cap rock and Watrous horizons. Interpretation and discussion of the following figures are provided in the discussion portion of this thesis. Several parameters can be extracted from the inversion, this study primarily focuses on anisotropy anomalies, their magnitude, orientation and uncertainty. The model used for the inversion process is that of a single parallel vertical fracture set, however, the observed anomalies represent anisotropy and are not necessarily fracture related. Attribute maps, such as AVO and zero offset reflection amplitude, are used in conjunction with the anisotropy maps to assess the validity of inversion results. AVOA anomalies are then filtered based on model correlation, RMS error, magnitude and percent uncertainty. Full page prints of each map are included in Appendix A.

### 5.1. Watrous

Inversion results for the Watrous horizon are shown in Figure 5.1. Anisotropy is generally low with a few exceptions occurring mostly near the peripheries of the study area. The periphery of the study area contains limited offset and azimuth distribution, which leads to greater uncertainty in the inversion. Few high magnitude anomalies are observed. The zero-offset reflection amplitude (Figure 5.2a) and isotropic AVO gradient (Figure 5.2b) are observed to be fairly consistent over the survey area. This suggests there are no major lithology changes at the Watrous horizon and that the inversion results are stable. Model correlation (Figure 5.2c) and normalized RMS difference (Figure 5.2d)

are also fairly consistent. Isolated areas of poor model fit and high RMS difference are highlighted in grey. Uncertainty in the magnitude of anisotropy, Figure 5.3a, ranges from 15% to over 100%. Higher levels of uncertainty are largely attributed to the scatter in extracted amplitudes with low anisotropic signal. Ultimately, this study looks to isolate points within the study area that show high levels of anisotropy which fit a vertical fracture model. Areas of interest are highlighted based on model correlation, magnitude, RMS difference, azimuth and offset coverage and uncertainty levels. A plot of residual anomalies was created by masking the initial inversion results and is shown in Figure 5.3b. The masked anomaly plot shows several scattered individual vectors within the study area and a few clustered areas with spatially consistent orientations. The isolated singular anomalies are likely exceptions. The clustered anomalies represent points of interest which are discussed in the following chapter. The orientations of anisotropy for all points within the study area and the residual anomalies are shown in Figure 5.4. Anisotropy orientations trend at  $45^\circ$  north east, which corresponds with the direction of maximum horizontal stress, and roughly  $315^\circ$ . The north west trend is more prominent amongst the residual anomalies.

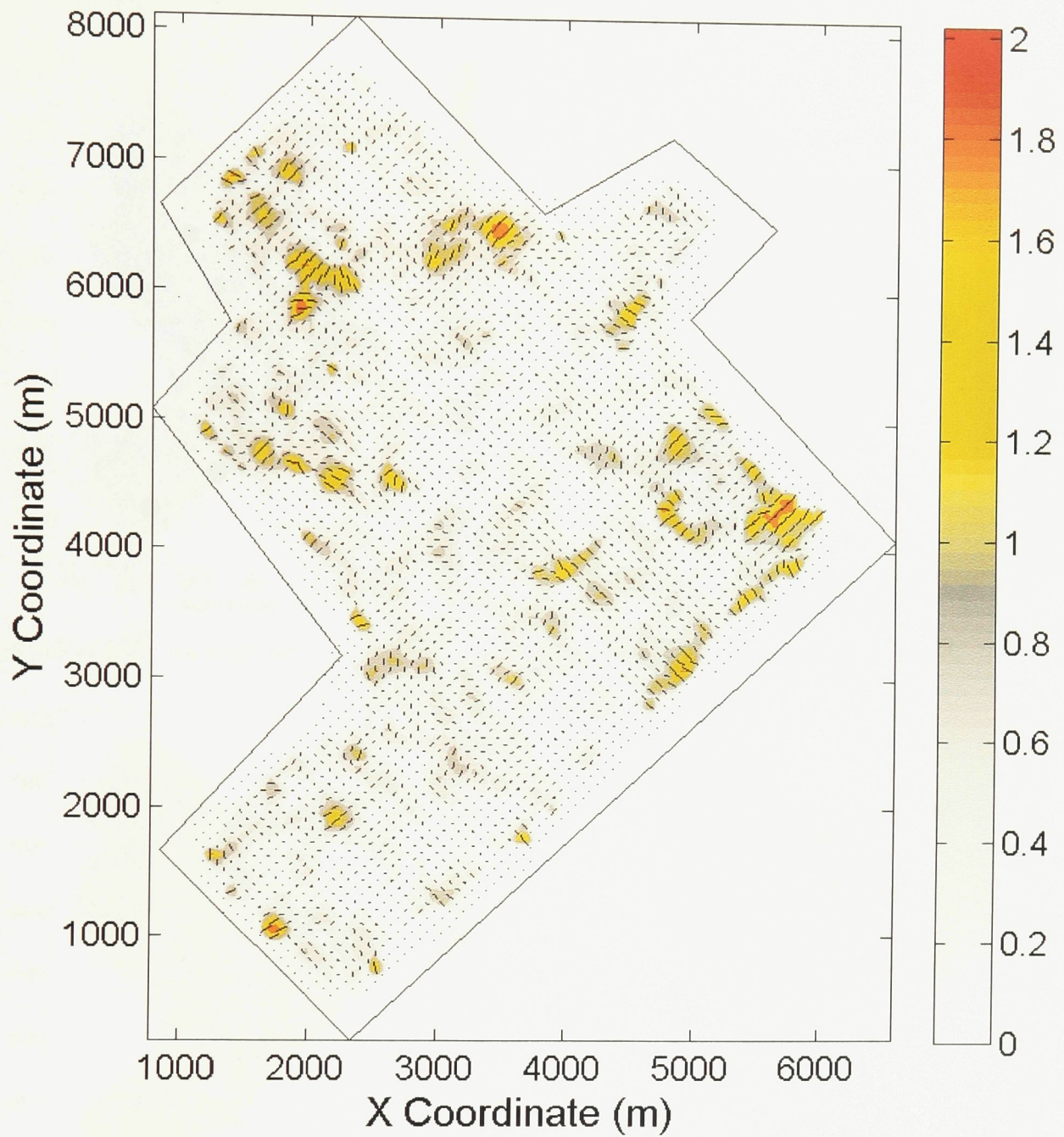
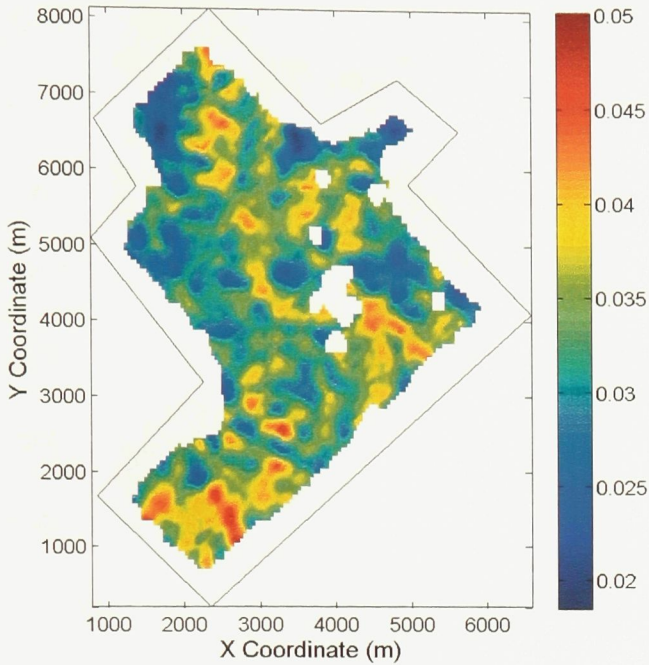
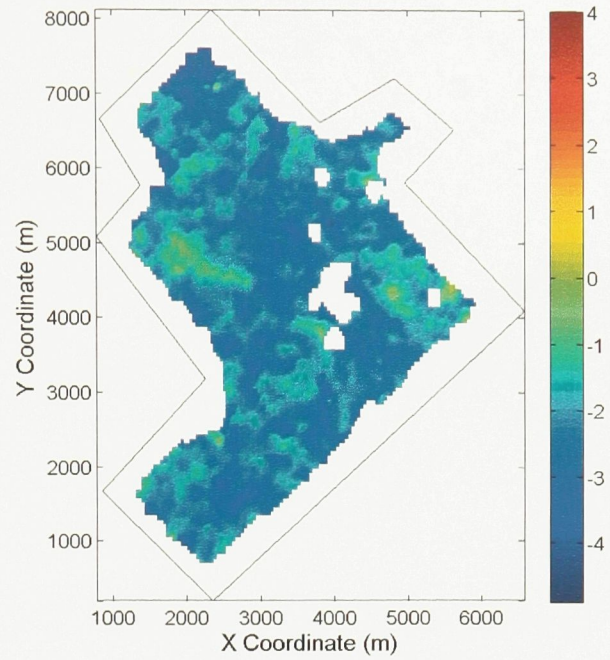


Figure 5.1 Normalized near-offset AVOA anisotropy magnitude from amplitude inversion of the Watrous horizon. Anisotropy magnitude is low over the majority of the study area with few isolated anomalies near the peripheries. Anomalies on the peripheries are unreliable due to reduced azimuth and offset coverage.

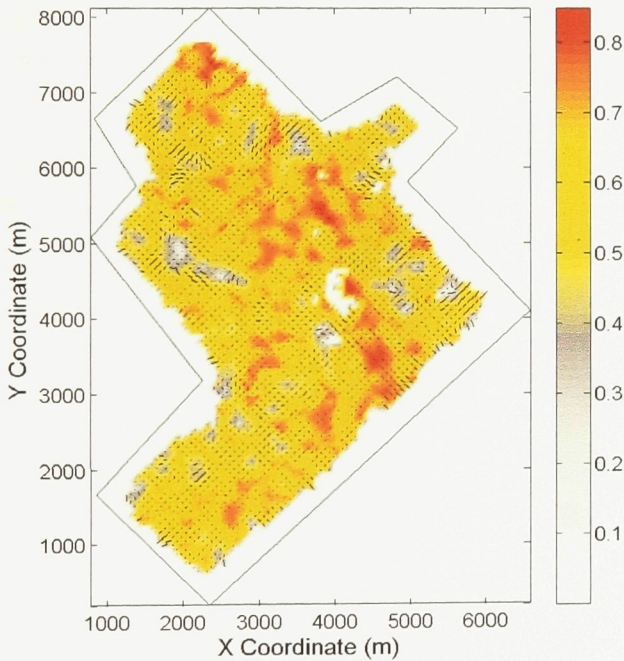
a) Zero-offset reflection amplitude



b) Normalized isotropic AVO gradient



c) Near-offset HTI model correlation



d) Normalized RMS difference

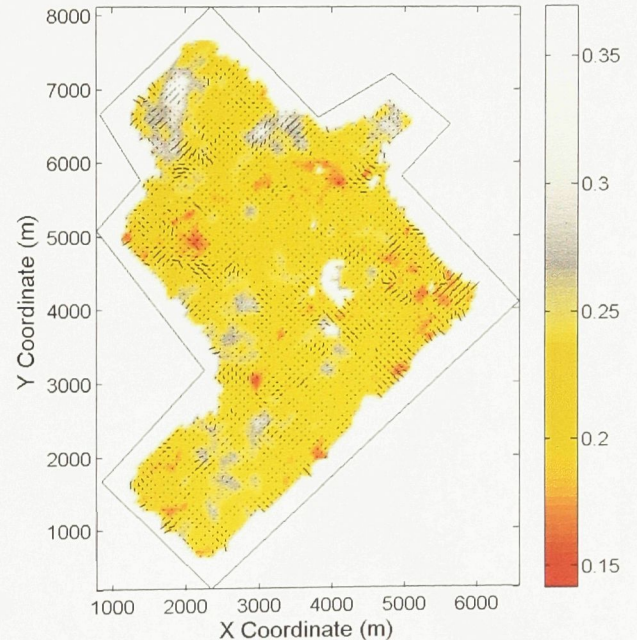
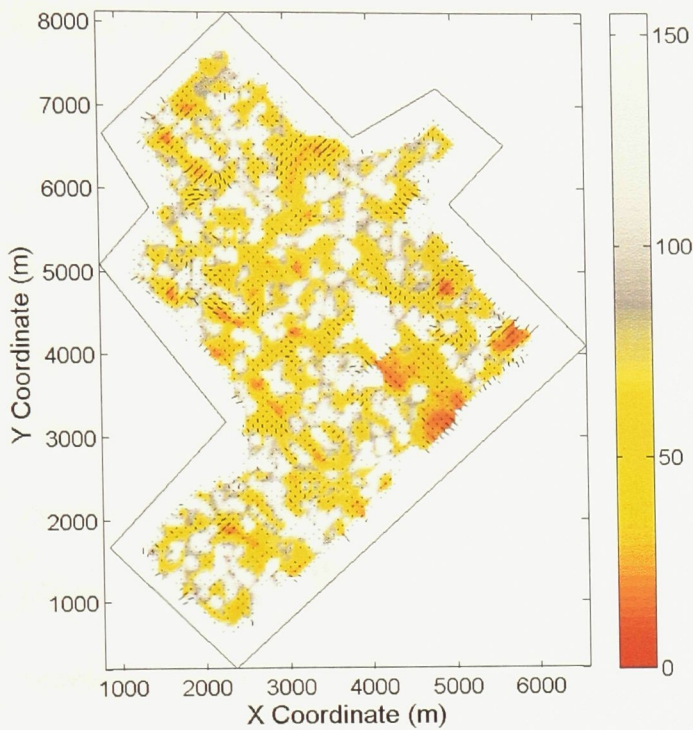


Figure 5.2 Attribute maps from AVOA inversion for the Watrous horizon. Attribute maps aid in assessing horizon properties and stability of the inversion. Masked portions in the center of the study area and along the peripheries result from reduced azimuth and offset coverage due to infrastructure and survey geometry.

a) % Uncertainty in the magnitude of anisotropy



b) Anisotropy vectors after masking

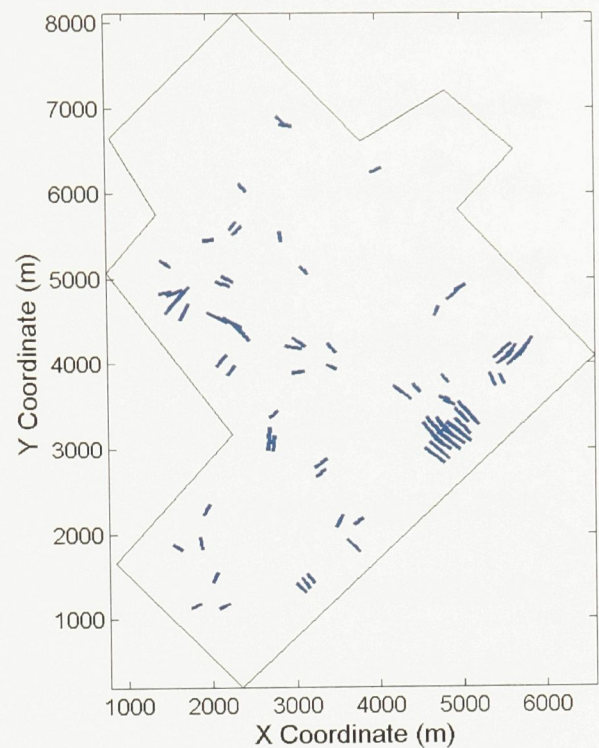
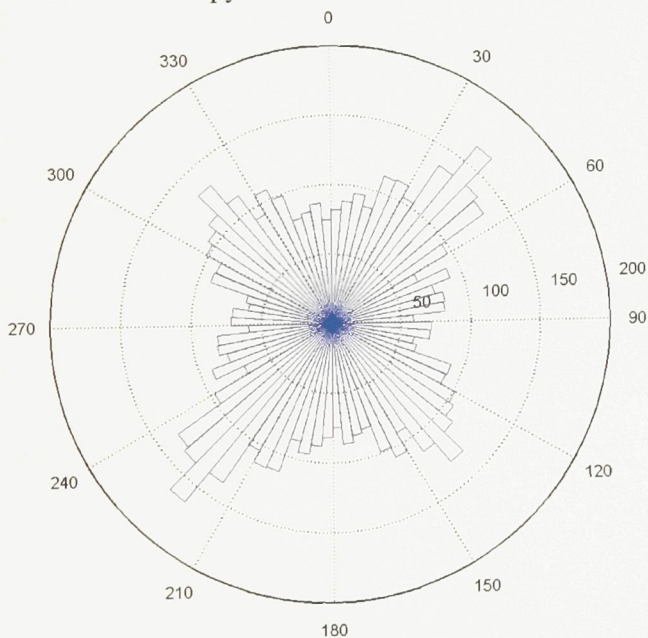


Figure 5.3 a) The percent uncertainty in the magnitude of anisotropy is obtained through a propagation of error using the standard errors of the regression coefficients. A measure of uncertainty is necessary to gain confidence when interpreting anisotropy anomalies. b) The residual anomalies after masking represent points with the highest correlation, lowest uncertainty and above average anisotropy.

a) Watrous anisotropy distribution for all data



b) Masked Watrous anisotropy distribution

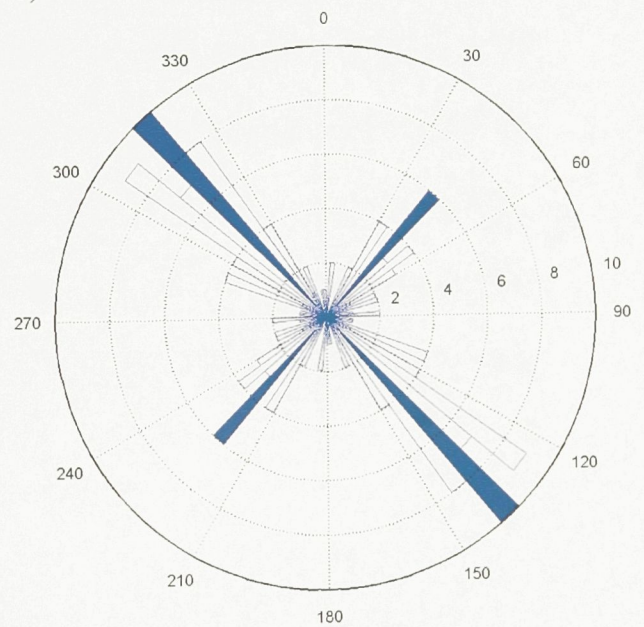


Figure 5.4 Anisotropy orientation distribution for a) all points within the study area and b) the residual anisotropy anomalies after masking. Orientations in b) correspond to vectors in Figure 5.3b.

## 5.2. Cap rock

Inversion results for the cap rock, Figure 5.5 show greater variability than the Watrous horizon with several high magnitude anomalies. Many of these anomalies are along the peripheries of the study area which are associated with greater uncertainty in the inversion. The remaining high magnitude anomalies within the interior of the study area are discussed in the following section. The zero-offset reflection amplitude (Figure 5.6a) and isotropic AVO gradient (Figure 5.6b) show greater variability when compared to results from the Watrous. The model correlation (Figure 5.6c) and normalized RMS (Figure 5.6d) show lower spatial consistency and higher variability. Generally, the southern regions of the study area show more reliable inversion results for the cap rock. Uncertainty values are higher for the northern portions of the study area (Figure 5.7a). Similarly to the Watrous horizon, areas of interest are isolated by masking the anisotropy results to create a map of residual anomalies (Figure 5.7b). The southern portions of the study area show clustered anomalies away from the survey edges which are discussed further in the following section. Finally, the orientations of anisotropy are shown for all data points Figure 5.8a, and for the residual anomalies Figure 5.8b. The cap rock shows more variation in anisotropy orientation for all data points and for residual anomalies. Prominent orientations are roughly  $30^\circ$ ,  $55^\circ$  north east and  $315^\circ$ . Similarly to results for the Watrous horizon, these orientations conform to the orientation of maximum horizontal stress.

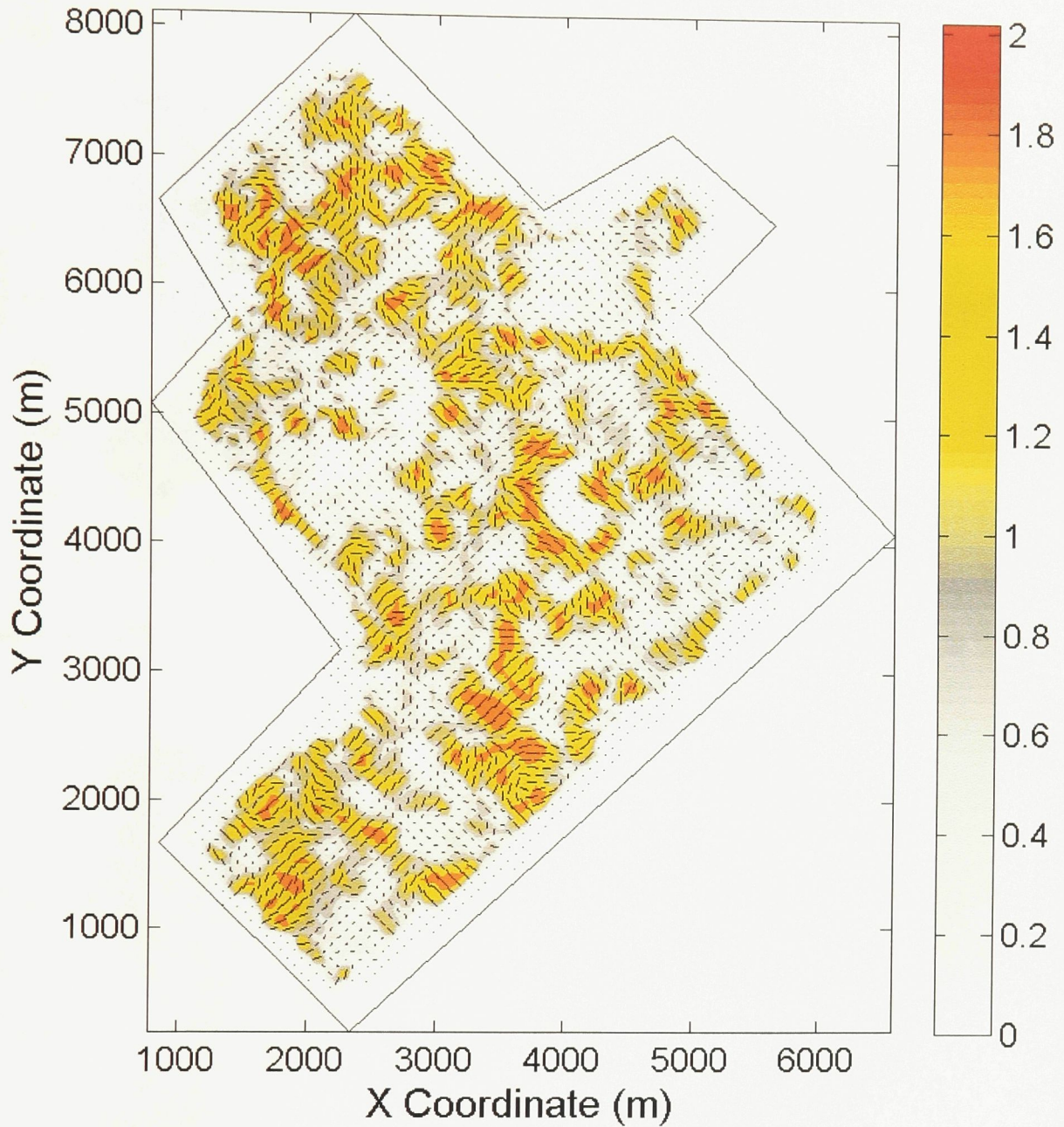
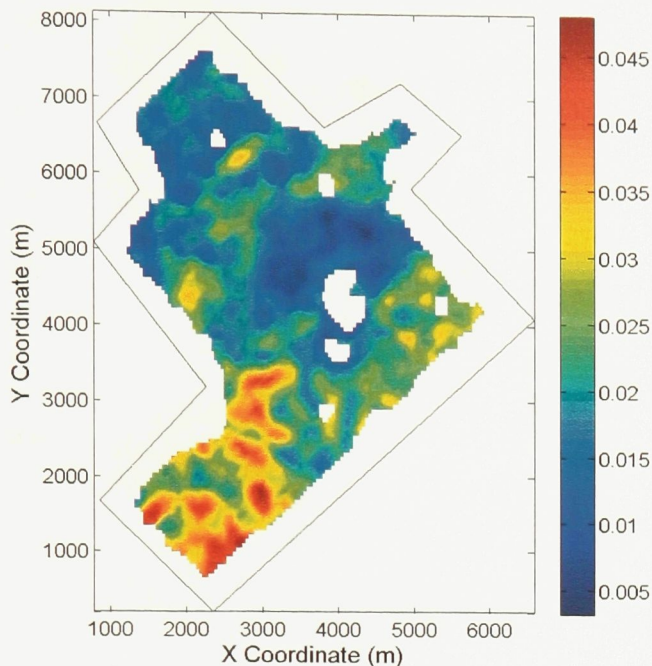
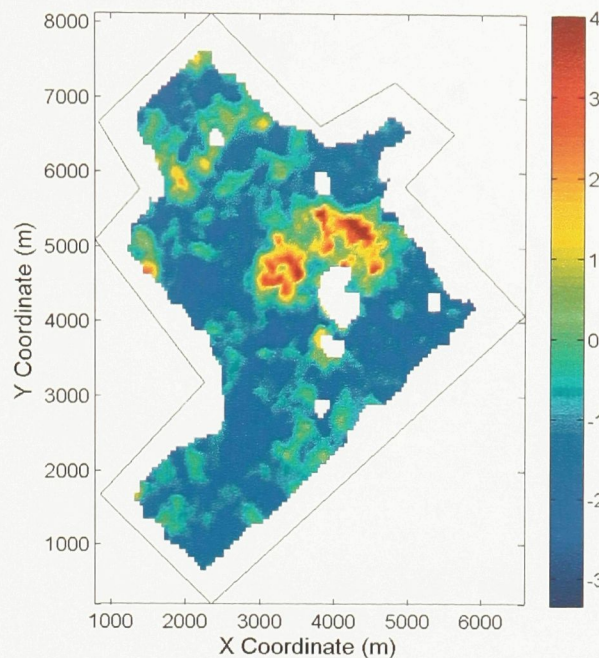


Figure 5.5 Normalized near-offset AVOA anisotropy magnitude from amplitude inversion of the cap rock horizon. Anisotropy magnitude varies from low to high over the study area. Points of low anisotropy represent a model fit to scatter in the data. Points of higher anisotropy which aren't associated with large uncertainties are of interest.

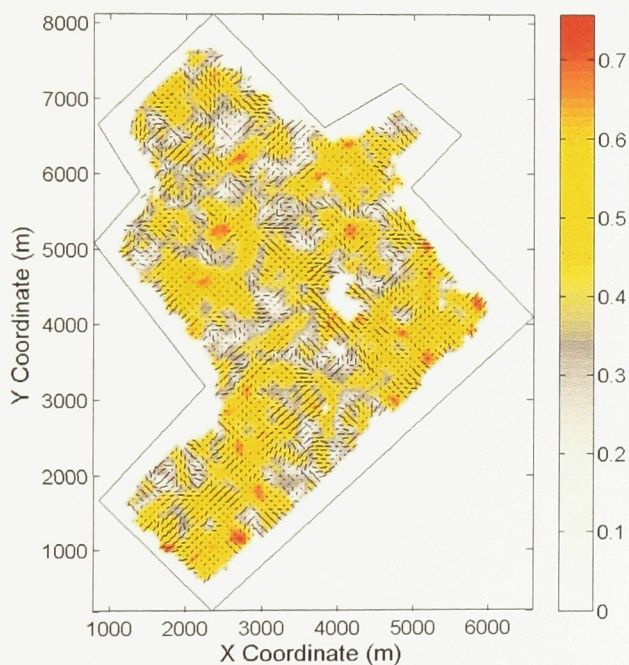
a) Zero-offset reflection amplitude



b) Normalized isotropic AVO gradient



c) Near-offset HTI model correlation



d) Normalized RMS difference

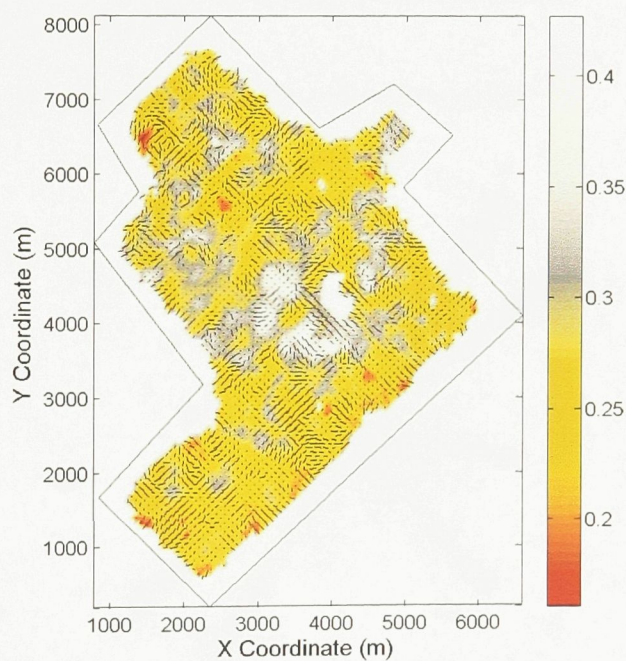
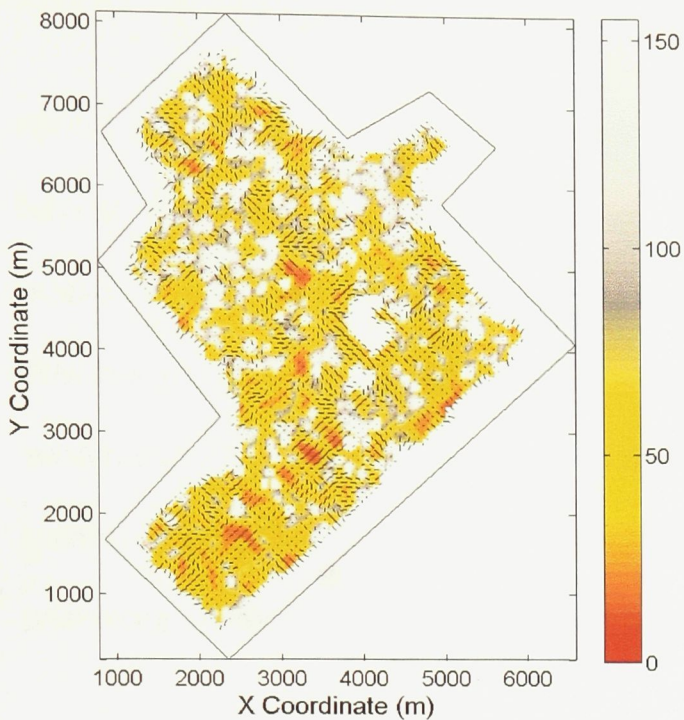


Figure 5.6 Attribute maps from AVOA inversion for the cap rock horizon. Attribute maps aid in assessing horizon properties and stability of the inversion. Masked portions in the center of the study area and along the peripheries result from reduced azimuth and offset coverage due to infrastructure and survey geometry.

a) % Uncertainty in magnitude of anisotropy



b) Anisotropy vectors after masking

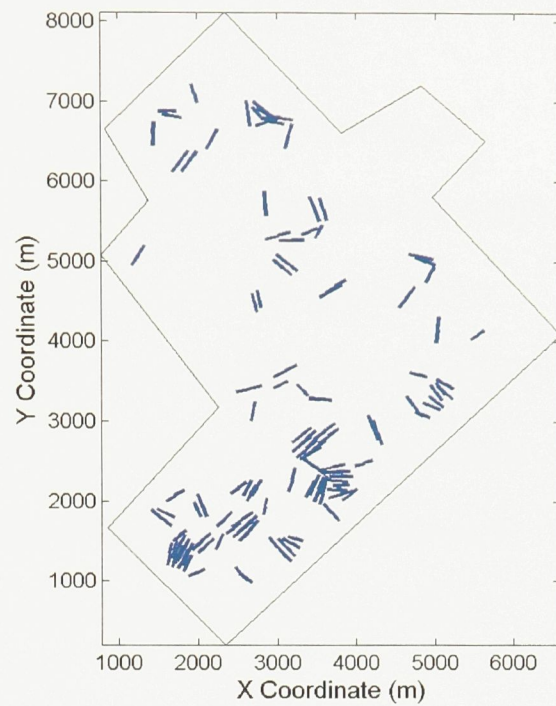
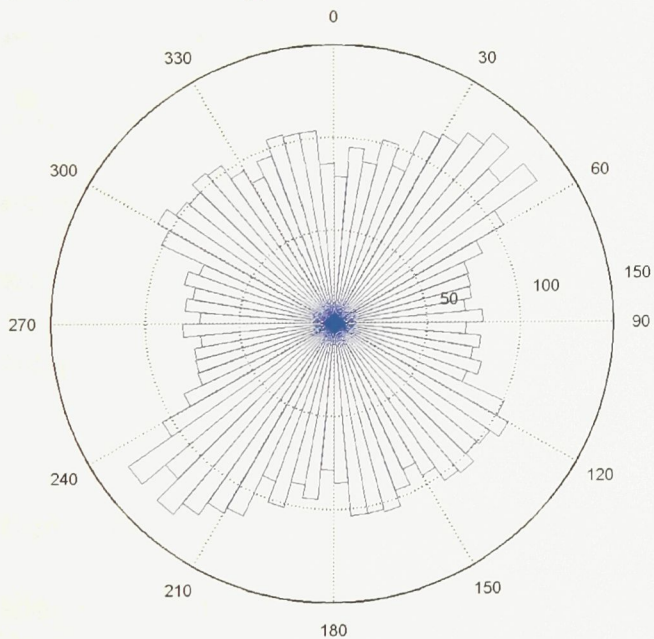


Figure 5.7 a) The percent uncertainty in the magnitude of anisotropy is obtained through a propagation of error using the standard errors of the regression coefficients. A measure of uncertainty is necessary to gain confidence when interpreting anisotropy anomalies. b) Residual anomalies after masking represent points with the highest correlation, lowest uncertainty and above average anisotropy.

a) Cap rock anisotropy distribution for all data



b) Residual cap rock anisotropy distribution

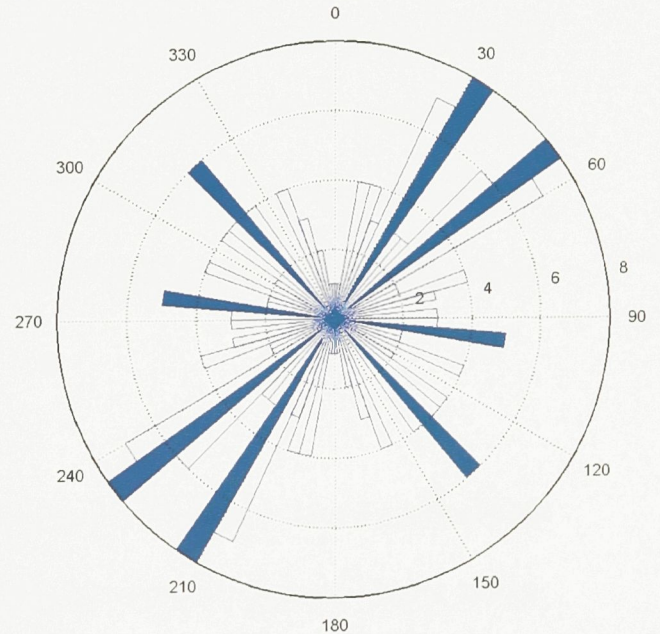


Figure 5.8 Anisotropy orientation distribution for a) all points within the study area regardless of uncertainty and b) the residual anisotropy anomalies after masking. Orientations in b) correspond to vectors in Figure 5.7b.

## Chapter 6. Discussion

---

AVOA analysis has been performed over the whole study area for two horizons of interest, the cap rock and overlying Watrous. Of the 8000 CMPs studied, few show high magnitude anomalies with lower statistical uncertainty and significant spatial extent.

This chapter discusses the observed anomalies to ensure they represent valid amplitude anisotropy for a given horizon. The areas of interest are assessed in terms of inversion stability, data quality and geologic factors affecting AVOA analysis. The interpreted anisotropy anomalies are the areas of best fit to a single vertical fracture set model.

### 6.1. Watrous anisotropy

Inversion results for the Watrous horizon are observed to be consistent over the study area for all parameters. Smooth spatial trends over a narrow range of values are observed in the zero-offset reflection amplitude and isotropic AVO gradient. This suggests there are no major lithology changes. Greater stability in the inversion results is attributed to the increased thickness of the Watrous and reduced stratigraphic complexity when compared with the cap rock interval.

High magnitude anisotropy anomalies are few in number. Those not directly associated with high uncertainty tend to be located on the peripheries of the study area. Areas with a higher magnitude of anisotropy and consistent orientation are highlighted in Figure 6.3. These anomalies are individually analyzed in order to gain confidence in their representation of anisotropy in the Watrous horizon.

A sample data distribution of offset and azimuth coverage for the anomaly denoted 'A' in Figure 6.3. is shown in Figure 6.4. Offset sampling within the super-CMP gather is fairly even. Azimuthal coverage is consistent with an exception over the 35-80° range, which has significantly fewer samples. Strong amplitude anisotropy is observed in the AVOA surface fit, Figure 6.5. However, the magnitude of anisotropy may be exaggerated due to the less constrained regression over the 35-80° azimuth range. The 'A' anomalies show linear features with consistent orientation to the north east and north west. Their lack of spatial extent suggests they are isolated features rather than representative of an anisotropic fabric in the Watrous horizon. A sharp decrease in model correlation and increase in uncertainty are observed immediately adjacent to these anomalies.

Anomaly 'B', Figure 6.3, is located in the south east corner of the survey area and is comprised of a cluster of super-CMP gathers with anisotropy oriented north east. Each of these points contains an even distribution of offsets and more limited azimuthal coverage in the 35-60° and 130-150° range. The under-sampled azimuth ranges are also the maximum and minimum values for the amplitude anisotropy. The magnitude of anisotropy is likely being exaggerated by a lack of constraint in the least squares regression over the under-sampled azimuth bins. A consistent spatial trend is observed in the 'B' anomaly; however, the proximity to the edge of the survey area and anisotropy alignment coinciding with under-sampled azimuth bins are cause for doubt in the validity of this anomaly.

Anomalies 'C' and 'D', Figure 6.3, are comprised of super-CMP gathers with consistent anisotropy orientation and magnitude over areas of roughly 720mx160m and 240mx80m respectively. Model correlation for these anomalies ranges from 0.6 to 0.8 providing some of the best model fits within the study area. The percent uncertainty in the magnitude of anisotropy for these areas is <30%. Fold for these limited offset super-CMP gathers ranges between 230-250. The anisotropy does not appear to result from an uneven sampling of offset and azimuth as shown by the data distribution in Figure 6.6. There are no sharp contrasts in the isotropic AVO gradient; however, there are linear highs in the zero-offset reflection amplitude. The trends in the zero-offset amplitude, with a north west orientation, may represent linear features of either lithology or a contrast in physical properties of the layer. Amplitudes extracted from the Watrous horizon over these areas show anisotropy with a consistent north west orientation that is not associated with poor data quality or coverage. These anomalies represent anisotropy with a good fit to the simplified HTI model for vertical fractures. Observing these features in the stacked seismic image, they are associated with slight dome features in the Watrous and overlying Lower Gravelbourg horizon. The dome shapes are the result of differential timing of salt dissolution in layers beneath the reservoir. Salt dissolution creates additional accommodation space during deposition resulting in over-thickened stratigraphy. The observed structural features are produced when surrounding salt is dissolved at a later date. Anisotropy present in overlying layers is known to distort the AVO response from underlying layers (Xu, 2006). These anomalies in the Watrous are expected to bias results for the cap rock.

### **6.1.1. Summary of Watrous anisotropy anomalies**

Inversion results for the Watrous horizon show consistently low anisotropy over the majority of the study area with a few isolated anomalies. Masking areas of high uncertainty and low magnitude yields four residual anomalies. Anomalies 'A' and 'B' can be attributed to large gaps in azimuthal coverage due to the proximity of the survey edge. The remaining anomalies, 'C' and 'D', show legitimate amplitude anisotropy with a good fit to the simplified HTI model. The anisotropy corresponds to the location of salt dissolution features in the Watrous and Lower Gravelbourg horizons on the seismic section, Figure 6.8

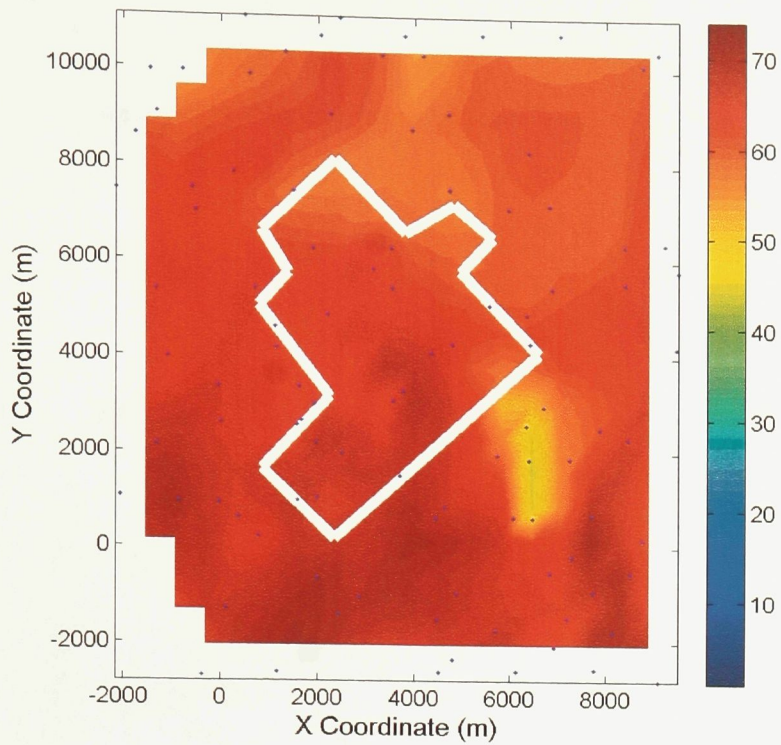


Figure 6.1. Watrous isopach thickness map. Thickness ranges from roughly 50m to 65m throughout the phase 1A area, outlined in white. Source data: true vertical depth well tops. Picks provided by PTRC Phase 1 (Whitaker, 2004).

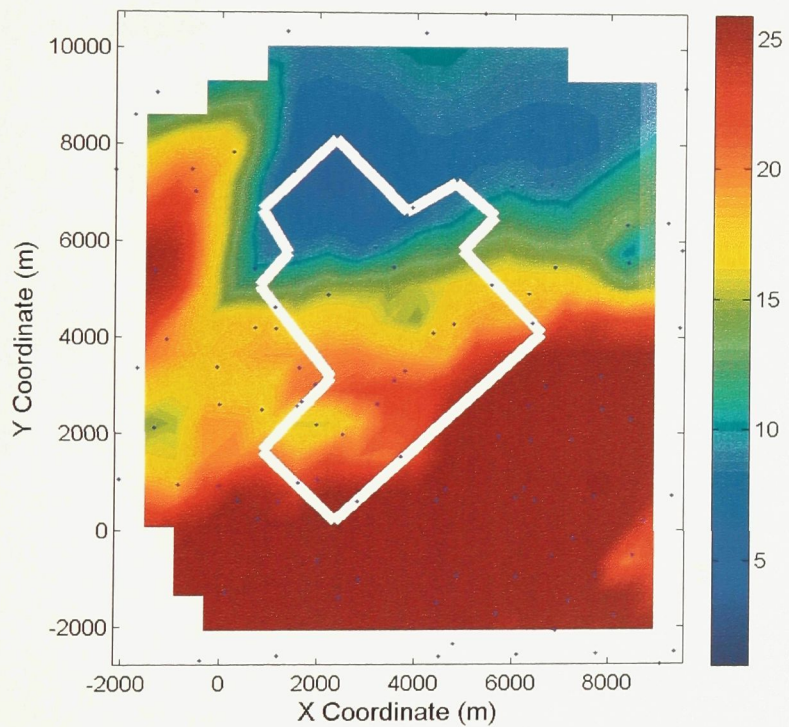


Figure 6.2. Combined Ratcliffe and Midale Evaporite isopach thickness map. Thickness ranges from roughly 25m in the south to 8m in the north. Source data: true vertical depth well tops. Picks provided by PTRC Phase 1 (Whitaker, 2004)

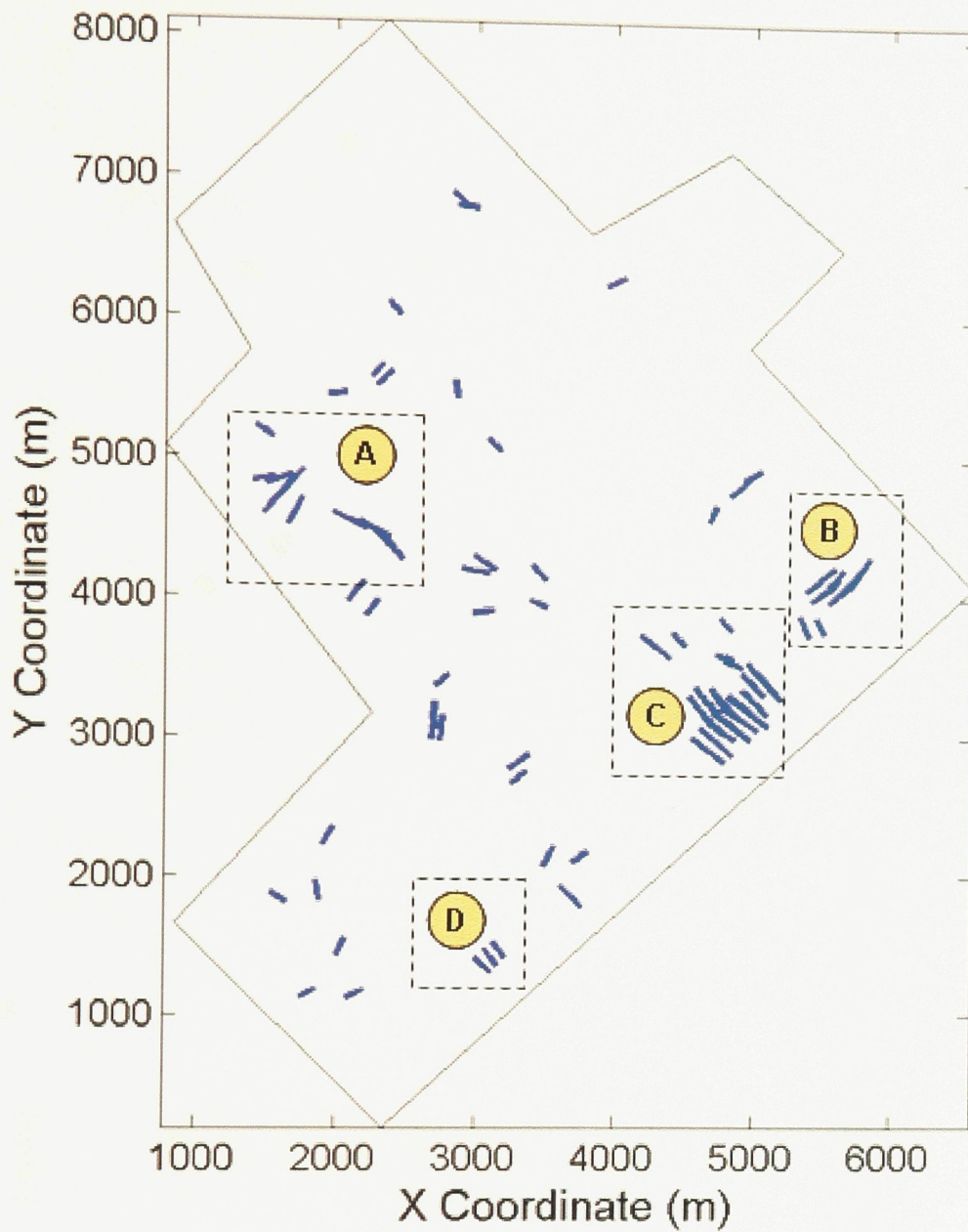


Figure 6.3. Wotrous horizon residual anisotropy anomalies. Anomalies are highlighted which show greater consistency in magnitude, orientation and spatial extent. Isolated anisotropy vectors are considered less reliable. Anomalies 'C' and 'D' represent valid amplitude anisotropy.

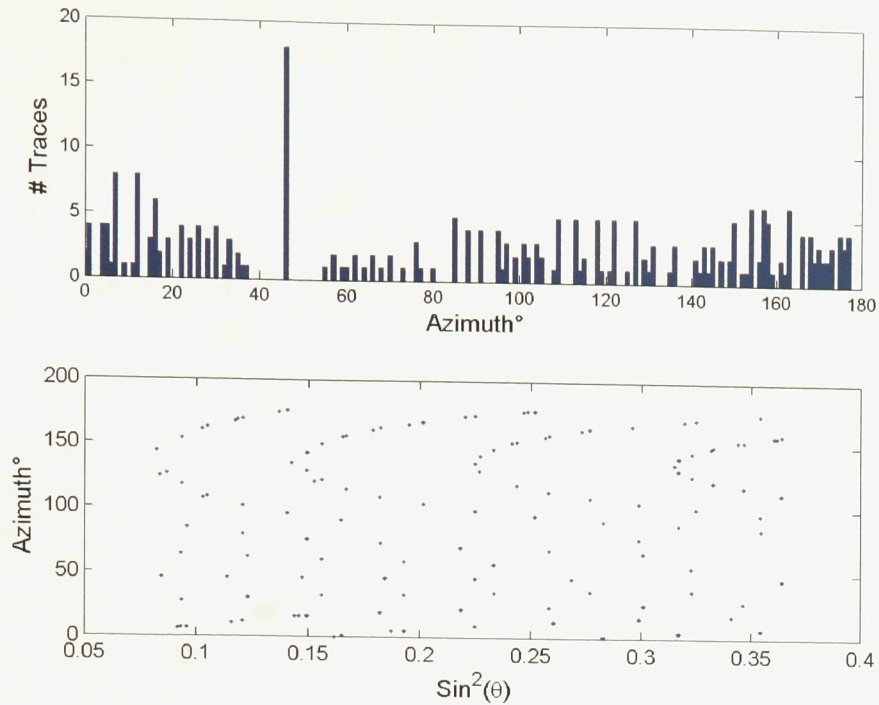


Figure 6.4. Offset and azimuth distribution for a sample point within the 'A' anomaly in Figure 6.3. Azimuthal coverage is consistent with the exception of the 35-80° range. Offset coverage is fairly even across all azimuths.

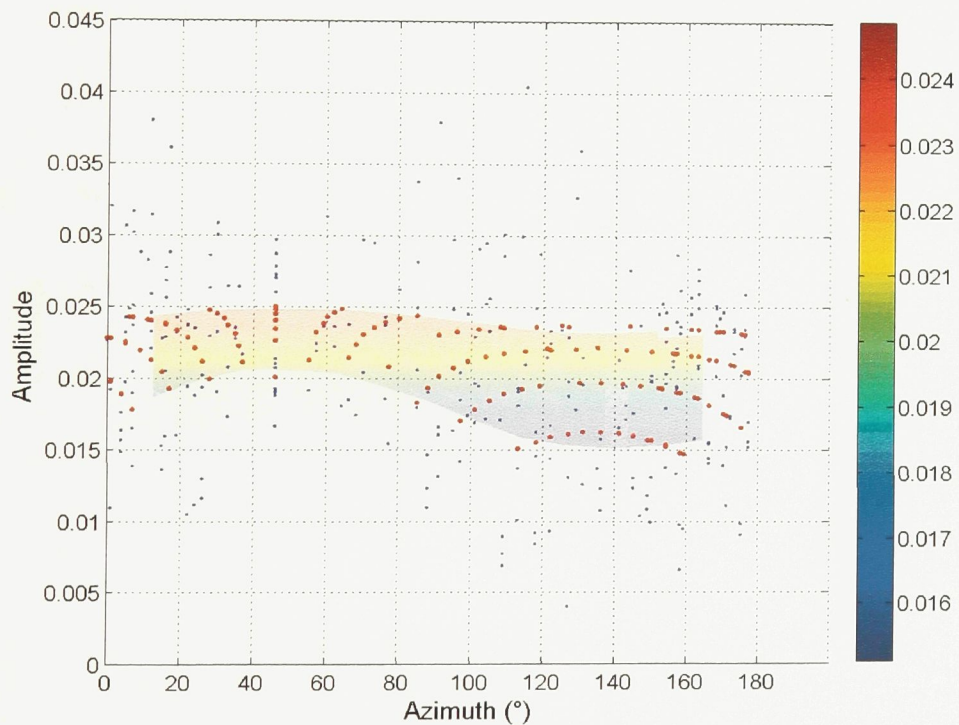


Figure 6.5. AVOA surface displayed in the amplitude – azimuth plane. Color shading corresponds to amplitude value. A strong azimuthal anisotropy is observed, however, this may be exaggerated due to an under-sampling of the 40-80° azimuth range. Red dots represent the AVOA surface fit to the data (blue dots)

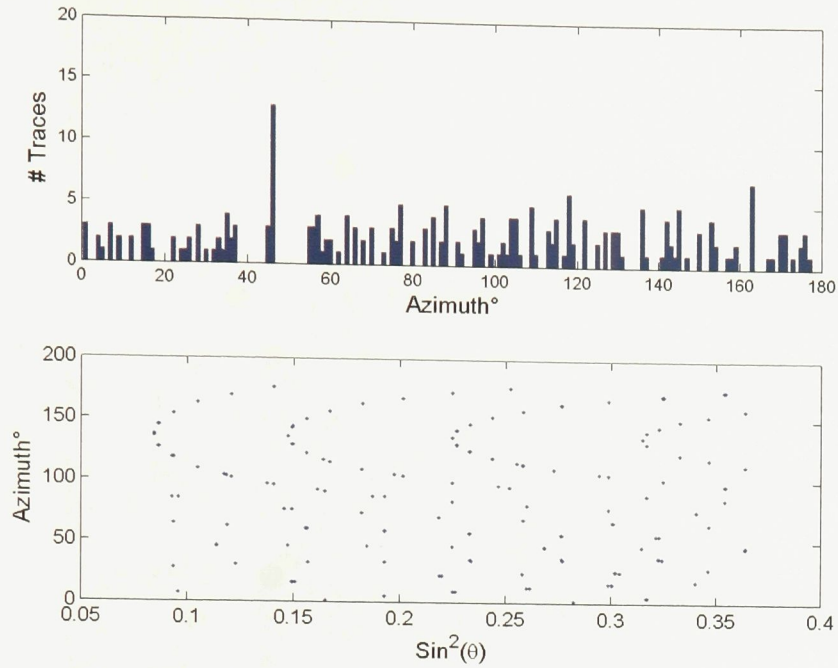


Figure 6.6. Offset and azimuth distribution for a sample point within the 'D' anomaly in Figure 6.3. Azimuthal coverage is consistent with the exception of the 35-55° range. Offset coverage is fairly even across all azimuths.

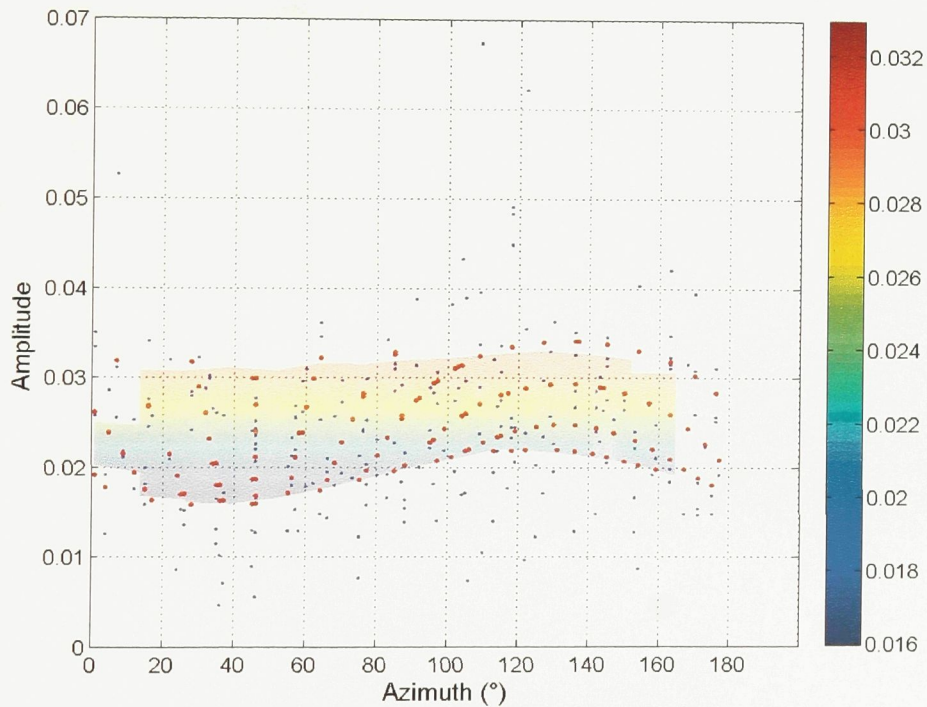


Figure 6.7. AVOA surface displayed in the amplitude – azimuth plane. Color shading corresponds to amplitude value. A strong azimuthal anisotropy is observed. Red dots represent the AVOA surface fit to the data (blue dots).

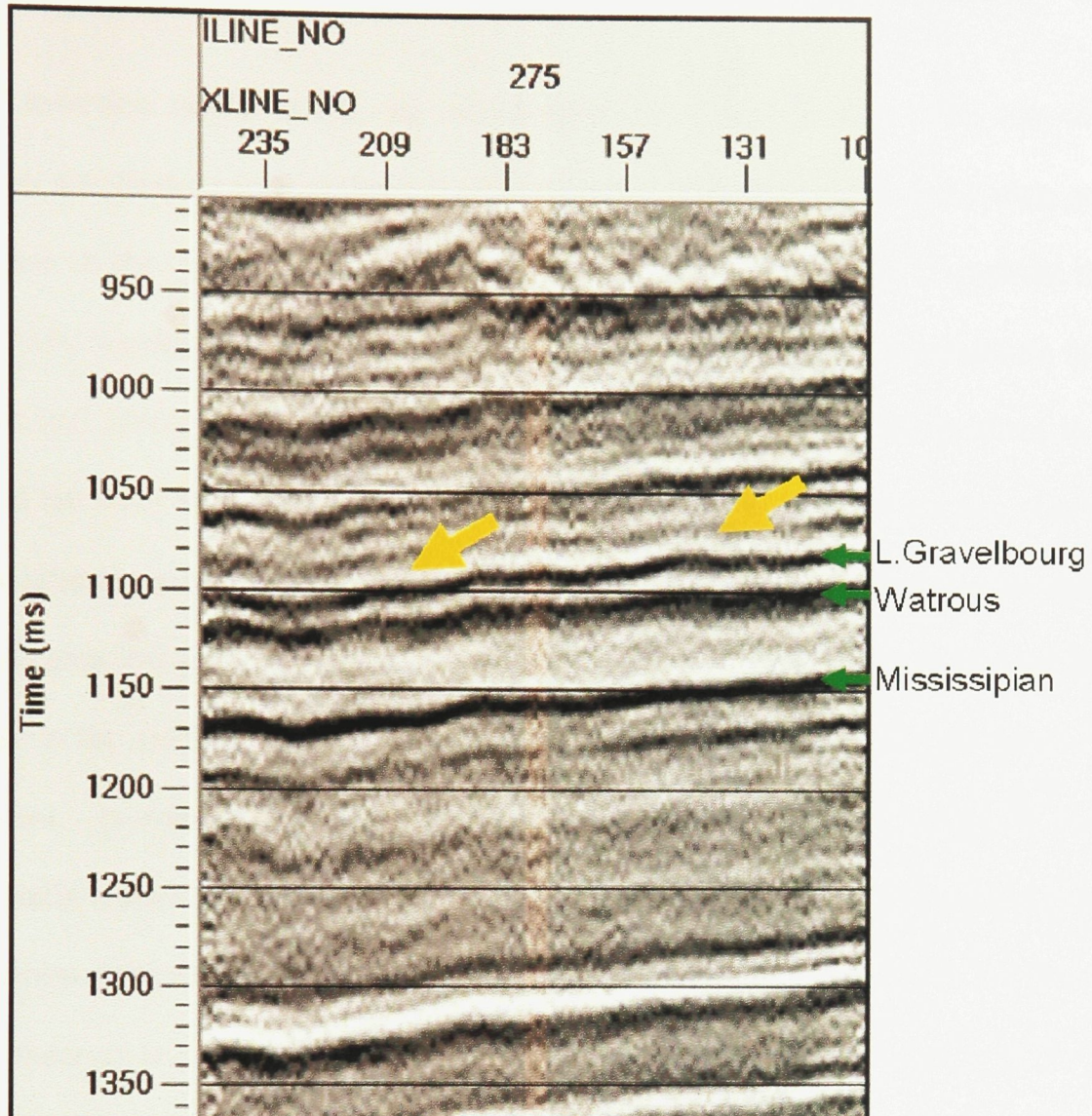


Figure 6.8. Stack image with arrows denoting the location of anomalies 'C' (right) and 'D' (left), Figure 6.3 and Figure 6.9. Slight dome features are observed in the Watrous and Lower Gravelbourg horizons. These structures result from salt dissolution below the reservoir. A high magnitude of anisotropy with north west orientation corresponds to these features. Anisotropy corresponding with the location of these anomalies is also observed at the cap rock, however, it may originate from the Watrous horizon or overlying layers.

## 6.2. Cap rock anisotropy

AVOA inversion results at the cap rock horizon are more variable. The zero-offset reflection amplitude map contains a region of higher amplitude to the south west and a low region in the central portions of the study area. The isotropic AVO gradient map, Figure 5.6b, is consistent over the majority of the study area with large exceptions in the northern and central portions of the study area. The sign of the AVO gradient in the center of the study area is reversed. Patches of reversed AVO gradient are also observed in the northern regions of the study area. The percent uncertainty is patchy throughout the study area, but generally lower in the southern regions. Similarly, model correlation is higher in the southern regions and patchy over the northern and central portions of the study area. Increased variability of the AVOA inversion results is attributed to the significantly reduced thickness of the combined cap rock interval when compared with the Watrous horizon. The combined Ratcliffe-Midale Evaporite isopach thickness is greatly reduced as it approaches the base of the sub-Mesozoic unconformity beyond the northern region of the Phase 1A area. The presence of multiple thin layers introduces additional uncertainty due to interference from multiples and thin bed tuning effects.

Several high magnitude anisotropy anomalies are present at the cap rock horizon. Anomalies along the edges are attributed to limited data availability. High magnitude areas with consistent orientation and within the central portions of the study area are of interest. Masking the results to remove points of low magnitude and higher uncertainty yields a map of residual anomalies. These anomalies are individually studied in order to gain confidence in their representation of anisotropy at the cap rock horizon.

The anomalies labelled 'A', 'B', in Figure 6.9 are isolated super-CMP gathers which pass the basic mask. These points do not show consistent spatial orientation and do not occur in clusters. They are surrounded by areas of low model correlation and increased normalized RMS error. Points near the periphery of the study area within anomaly 'A', contain gaps in azimuthal coverage which introduces uncertainty in the inversion results. These anomalies occur over areas where the combined cap rock interval is <15m thick. Modeling studies, Figure 4.4, have shown that amplitudes in the presence of multiple thin layers do not conform to the near-offset HTI model using processing techniques within the limits of this study. Additionally, anisotropy from the underlying reservoir will appear at the cap rock horizon when the total thickness is <15m. Points within anomaly B occur in an area of high fold coverage, however these traces are from long offsets beyond the range used in AVOA inversion. The limited number of near offsets is due to the presence of nearby infrastructure. This causes similar gaps in azimuthal coverage to those points on the periphery of the study area.

The anomalies, 'C' and 'D', are similar in magnitude, orientation and location to those in the overlying Watrous horizon. They contain a similarly high fold of 250-275 traces per near-offset limited super-CMP gather. These anomalies contain limited azimuthal coverage in the 40-60° range; however, this is typical of most points within the survey area due to the acquisition geometry. Uncertainty within these areas is low at less than 30% and model correlation is higher than average at 0.5-0.6. A strong anisotropy is present in the extracted amplitudes which does not appear to be the product of poor data quality or coverage. However, these anomalies will likely contain a downward propagation of amplitude anisotropy from the overlying Watrous. These anomalies may also be associated with salt dissolution structures observed in the seismic section Figure 6.8.

The 'E' anomaly, Figure 6.9, contains two distinct clusters along a north north[east trend with similar north east orientation. The combined area of the anomaly is roughly 480m x 1000m. Model correlation for these anomalies is higher ranging from 0.5-0.7 and uncertainty in the magnitude of anisotropy is less than 35%. The cap rock interval thickness from which the amplitudes are extracted is approximately 20m over the area 'E'. The zero-offset reflection amplitude is generally higher and more variable than was observed for the Watrous horizon. The isotropic AVO gradient varies between negative and positive values. These anomalies primarily occur where the isotropic AVO gradient approaches the zero crossing (Figure 5.6b). Data distribution for this anomaly is good, with a high fold of 285 traces and only a slight gap in the 35-55° azimuth range Figure

6.10, Figure 6.11. Extracted amplitudes show strong anisotropy with consistent orientation, and which does not appear to be a result of poor data coverage or quality. The variability in the zero-offset reflection amplitude and isotropic AVO gradient may influence the anisotropy of the amplitudes. The amplitude data for anomaly 'E' show a good fit to the HTI model with comparatively low uncertainty and a high magnitude of anisotropy. A salt dissolution structural high, which continues through the Watrous horizon, corresponds to the location of this anomaly, Figure 6.12. Anisotropy anomalies are observed in the overlying Watrous horizon for the same area; however, they are considerably lower in magnitude. The interval thickness of 20m still provides the possibility that anisotropy from the underlying reservoir may be observed at the cap rock horizon, Figure 4.4. The spatial extent and consistency in orientation are more in line with the expected response from a layer with anisotropic fabric. The presence of anisotropy in the cap rock horizon appears to be valid for the anomalies located in area 'E'.

Anomaly 'F', Figure 6.9, contains two clusters of residual anomalies in close proximity with north east orientation. The anomaly does not appear to be the result of limited offset or azimuth coverage. Model correlation and normalized RMS error indicate there is a greater discrepancy between the data and the simplified HTI model when compared with the 'E' anomaly. The 'F' anomaly contains a higher degree of uncertainty in the magnitude of anisotropy at greater than 35%. There are no corresponding high magnitude anomalies observed in the overlying Watrous for this area. The isotropic AVO gradient

shows a region of alternating sign from negative to positive coinciding with the area 'F'. This characteristic is observed in the amplitude-offset plane of the AVOA surface. Anomaly 'F' appears to represent a valid anisotropy in reflection amplitude at the cap rock horizon. However, the association with changing isotropic AVO gradient, comparatively lower model correlation and increased RMS error result in greater uncertainty than anomalies shown in 'E'. The area corresponds to the flanks of a structural high in the caprock and Watrous horizon produced by salt dissolution.

Anomaly 'G', Figure 6.9, shows consistent north east orientation and does not appear to be associated with any obvious features in the stacked section. Despite it's proximity to the survey edge, there are no significant offset or azimuth coverage gaps, Figure 6.14, Figure 6.15. No corresponding amplitude anomalies are observed in the overlying Watrous horizon. The isotropic AVO gradient changes sign and the zero-offset reflection amplitude is more variable over this area. Uncertainties in this area are higher than for anomalies 'E' and 'F' at greater than 40%. Anomaly 'G' shows a reasonable fit to the HTI model and represents valid anisotropy at the cap rock horizon.

### **6.2.1. Summary of cap rock anisotropy anomalies**

Increased variability in the magnitude of anisotropy at the cap rock horizon is observed throughout the study area when compared to the Watrous horizon. Several higher magnitude anomalies are present with consistent orientation over many super-CMP gathers. Masking areas of high uncertainty and low magnitude yields seven residual

anomalies. Anomalies 'A' and 'B' can be attributed to large gaps in azimuthal coverage due to the proximity of the survey edge. Anomalies 'C' and 'D' along the southern edge coincide with anisotropy present at the Watrous horizon and are likely affected by a downward propagation of that overlying anisotropy. Areas 'E', 'F' and 'G' show legitimate amplitude anisotropy with a good fit to the simplified HTI model. Results from the combined Ratcliffe, Midale Evaporite cap rock interval are more uncertain than those of the Watrous due to the presence of multiple thin layers and increased vertical heterogeneity in lithology. High magnitude anomalies 'E' and 'F' correspond to salt dissolution structures in the cap rock and overlying Watrous horizon.

### **6.3. Significance of cap rock anisotropy**

Assessment of residual anomalies finds at least five areas, two in the Watrous horizon and three in the cap rock horizon, with a high magnitude of anisotropy. Having shown that these anomalies represent valid anisotropy in the reflection horizons, they may be discussed in terms of geology and their impact on CO<sub>2</sub> monitoring and storage.

## 6.4. Sources of anisotropy

AVOA inversion is based on the HTI model of anisotropy which can result from a single aligned vertical fracture set, however, there are several potential causes of seismic anisotropy. Anisotropy at the target horizons may also be caused by one or more of the following: overlying layers, influence from the underlying layer in the case of thin beds, alignment of minerals or fabrics, faults and stress induced anisotropy.

If the response from the cap rock horizon was largely due to overlying layers, similar levels of anisotropy should also appear at the Watrous horizon. Comparing Figure 5.1 and Figure 5.5 this is not observed, the cap rock and Watrous horizons show considerably different levels of anisotropy. Modeling has shown that with decreasing cap rock interval thickness, higher levels of anisotropy from the underlying reservoir are observed. For layer thickness in excess of 20m, the magnitude of anisotropy of an anisotropic cap rock is more than double that of the isotropic case (Figure 4.4c,d). This suggests that if anisotropy from the underlying reservoir was observed throughout the study area, cap rock anisotropy would still appear as a high magnitude anomaly. Considering Figure 5.5, several distinct highs are observed. The combined cap rock interval is composed of evaporite, anhydrite and anhydritic dolostones (Whittaker, 2004). Studies of salt and salt-correlated anhydrite core samples from the Western Canadian Sedimentary Basin show anisotropy in S-wave velocities and reflection amplitudes from stress-induced crystal alignment (Sun, 1991). Numerical simulations find that lattice preferred orientation (LPO) developed during salt deformation can result in seismic anisotropy of up to 5% in P-wave velocity and 10% shear-wave splitting. However, modeling studies

of reflection amplitudes from a thick horizontal salt layer show less of an amplitude variation with azimuth effect (Raymer et. al., 2000). Given the composition of the cap rock interval, it will likely exhibit anisotropic properties which will affect the AVOA results. However, if the alignment of minerals or fabrics were the largest contributor of anisotropy at the cap rock horizon, a more uniform response would be expected. The presence of isolated highs, with spatially consistent orientation, suggests the cause of anisotropy is related to local properties of particular sites within the Phase 1-A area. The observed anisotropy is discontinuous over the field area and likely does not represent fault planes, although it may result from fracturing associated with faulting. A shear fault system is interpreted by Bunge, 2000 which crosses the width of the Phase 1A area; however, the faults could not be imaged directly with the available seismic data.

Injection and production operations at the Weyburn field over the last 50 years could have potentially induced fracturing above the reservoir. Microseismic monitoring in the Phase 1-A area has shown events to occur above the reservoir over horizontal production wells (Verdon, et al., 2010). Geomechanical modeling shows that, if the reservoir is more compliant than expected from core logs, stress transfer into layers above the reservoir may induce microseismicity (Verdon, et al., 2010).

## 6.5. Anisotropy and an indication of fracturing

The residual anisotropy anomalies may indicate areas of fracturing in the cap rock interval. If the observed anisotropy is fracture related, the dominant fracture orientation is north east which is sub-parallel to the direction of maximum horizontal stress and is in agreement with previous fracture studies at the Weyburn field (Figure 6.16). Anisotropy orientations from AVOA inversion are found to be roughly  $30^\circ$  and  $50^\circ$  north east,  $315^\circ$  north west and  $280^\circ$ . A study of 48 vertical cores and 3 formation microscanner (FMI) logs finds 76% of fractures strike  $50^\circ$  to  $60^\circ \pm 30^\circ$  (Fischer, 1994). A combination of oriented core logs and electrical micro imaging (EMI) logs from horizontal wells find prominent open fracture orientations of  $40^\circ \pm 5^\circ$ ,  $285^\circ \pm 7^\circ$  and  $328 \pm 11^\circ$  (Bunge, 2000). The north east trend in anomalies is sub parallel to the horizontal production wells, with consistent north east orientation (Figure 6.17). These anisotropy orientations also match those predicted by geomechanical modeling using a more compliant reservoir (Verdon, et al., 2010).

The isolated nature of the anisotropy anomalies may be explained by their correlation with salt dissolution structures. Salt dissolution from beneath the reservoir causes a sag in overlying stratigraphy which can result in fracturing. This effect may be enhanced on the flanks of structural highs which are interpreted as over-thickened layers resulting from the differential timing of salt dissolution. It has been suggested that salt dissolution may be responsible for much of the primary fracturing in carbonates of the Midale reservoir (Bunge, 2000). Fracturing may have also occurred in the overlying Midale Evaporite and Ratcliffe beds; however, a more malleable anhydrite composition would

allow these fractures to heal. Microseismicity from production and injection activities may result from reactivation of these pre-existing fractures.

## **6.6. Recommendations for future CO<sub>2</sub> monitoring**

If the anisotropy is due to fractures, they may provide pathways for upward migration of CO<sub>2</sub> and other reservoir fluids. However, geochemical monitoring and core samples have not shown evidence of this occurring (Qing, 2004). AVOA analysis reveals anisotropy anomalies in the cap rock interval; however, it cannot determine if they are connected or permeable. Time lapse seismic techniques have successfully shown amplitude and time difference anomalies related to CO<sub>2</sub> accumulation around the injection wells in the reservoir (White, 2009). The same techniques should be used to monitor for potential accumulation of CO<sub>2</sub>, or other reservoir fluids, in overlying layers.

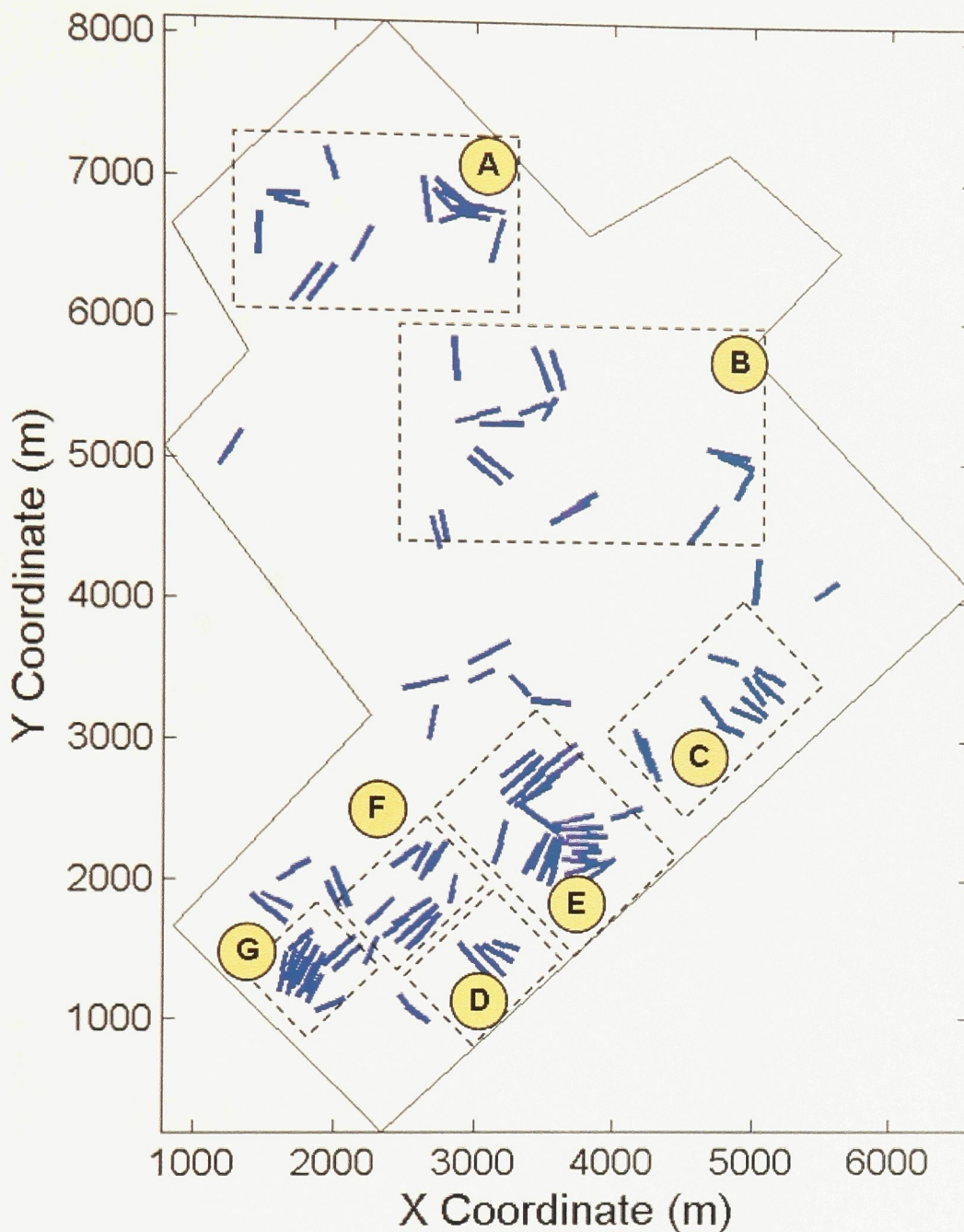


Figure 6.9. Cap rock residual anisotropy anomalies. Anomalies are highlighted which show greater consistency in magnitude, orientation and spatial extent. Isolated anisotropy vectors, 'A' and 'B' are considered less reliable. Anomalies 'E', 'F' and 'G' show valid amplitude anisotropy at the cap rock horizon. 'C' and 'D' also appear in the Watrous horizon.

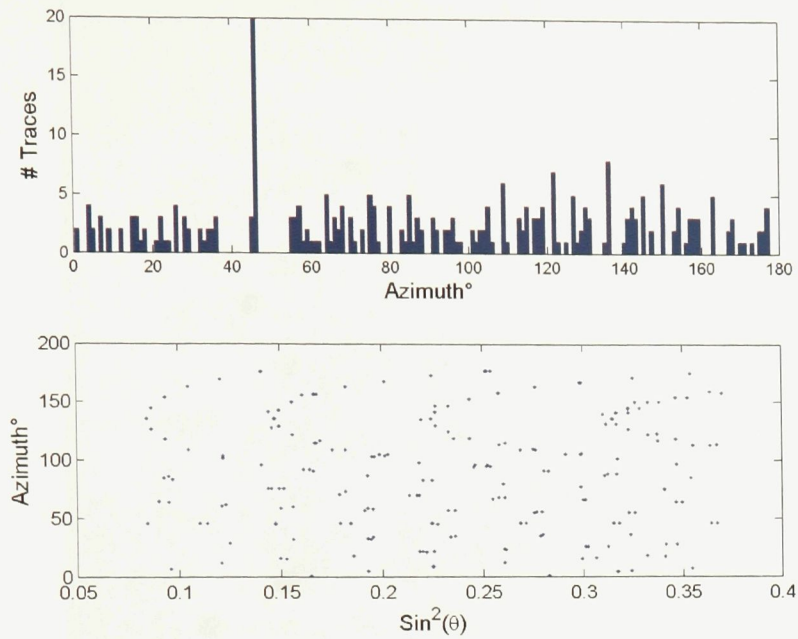


Figure 6.10. Offset and azimuth distribution for a sample point within the ‘E’ anomaly, Figure 6.9. Azimuthal coverage is consistent with the exception of the 35-55° range. Offset coverage is fairly even across all azimuths.

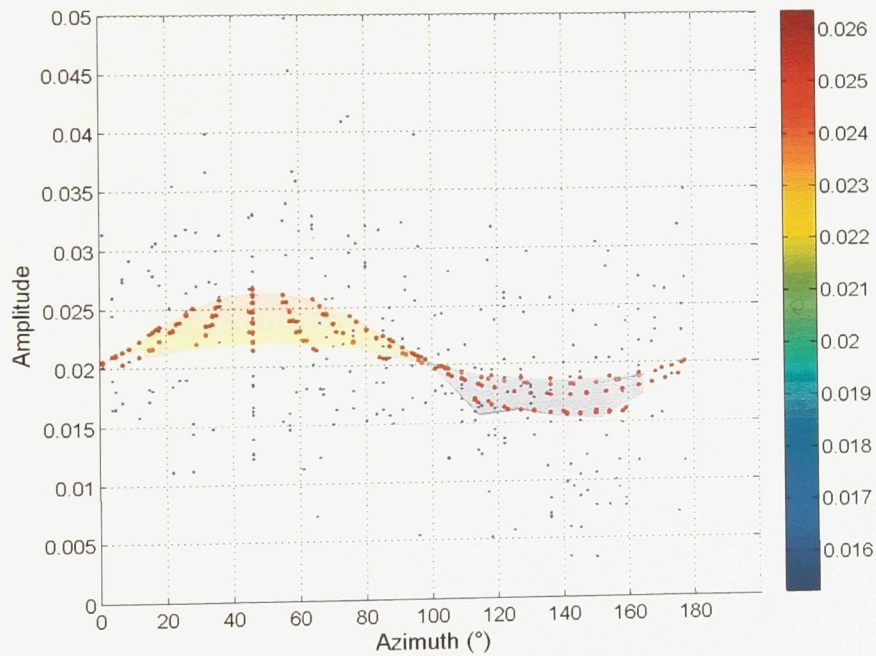


Figure 6.11. AVOA surface displayed in the amplitude – azimuth plane. Color shading corresponds to amplitude value. A strong azimuthal anisotropy is observed for the ‘E’ anomaly, Figure 6.9. Red dots represent the AVOA surface fit to the data (blue dots).

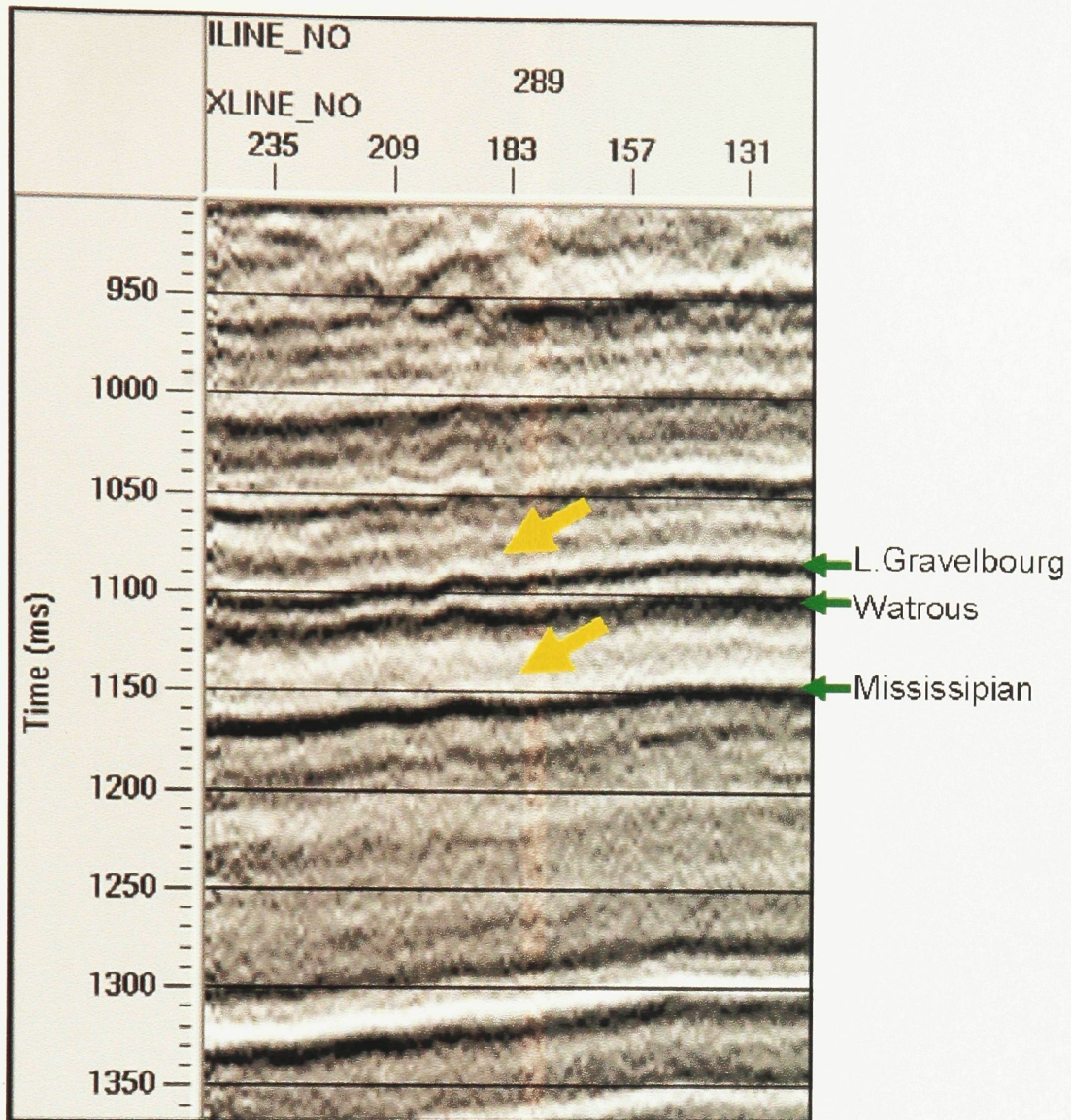


Figure 6.12. Stack image with arrows denoting the location of anomaly 'E', Figure 6.9. Salt dissolution structures are observed in the cap rock (Mississipian) horizon which extend upwards through the Watrous and Lower Gravelbourg horizons. A high magnitude of anisotropy with north east orientation corresponds to this feature, which extends from the southern edge of the survey area roughly 1km north. Anisotropy is also observed in the Watrous horizon at this location; however, its magnitude is greatly reduced in comparison to the cap rock.

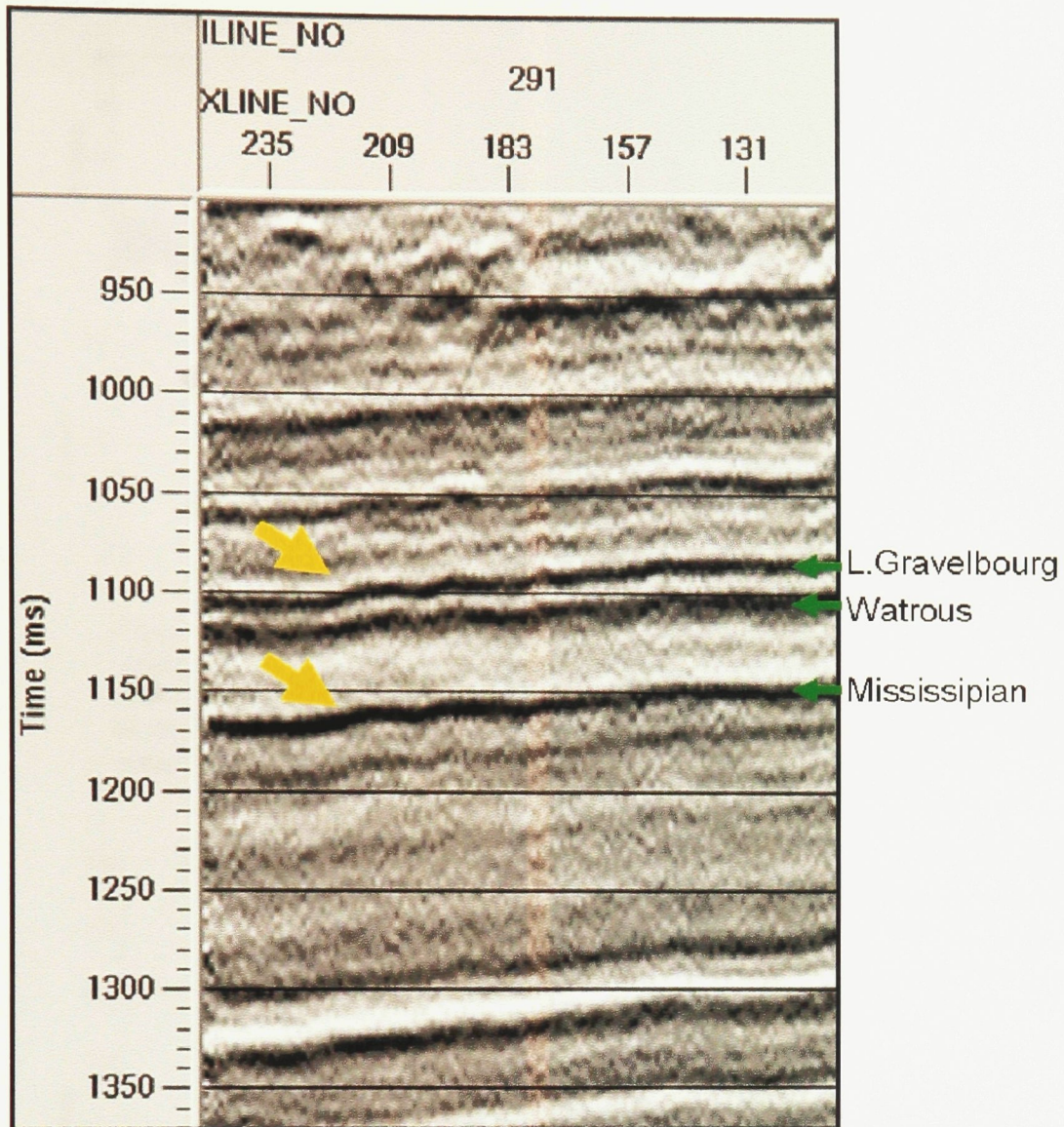


Figure 6.13. Stack image with arrows denoting the location of anomaly 'F', Figure 6.9. Salt dissolution structures are observed in the cap rock (Mississippian) horizon which extend upwards through the Watrous and Lower Gravelbourg horizons. A high magnitude of anisotropy corresponds to the flanks of this feature. Anisotropy is oriented to the north east.

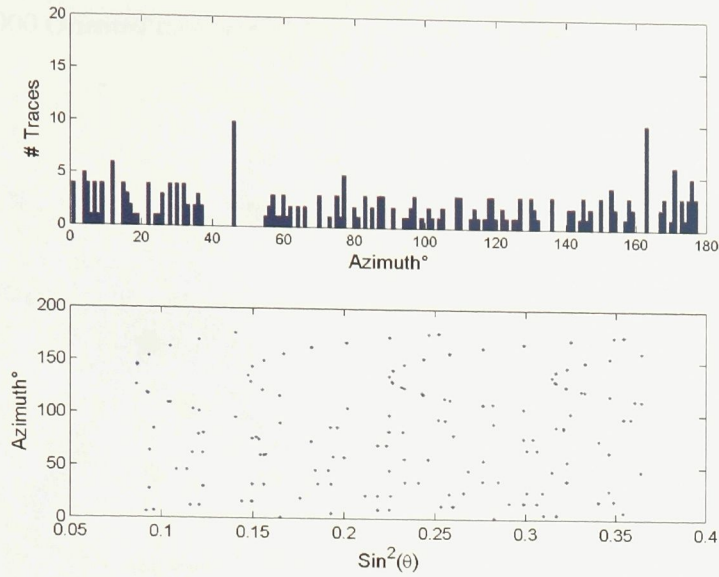


Figure 6.14. Offset and azimuth distribution for a sample point within the 'G' anomaly, Figure 6.9. Azimuthal coverage is consistent with the exception of the 35-55° range. Offset coverage is fairly even across all azimuths.

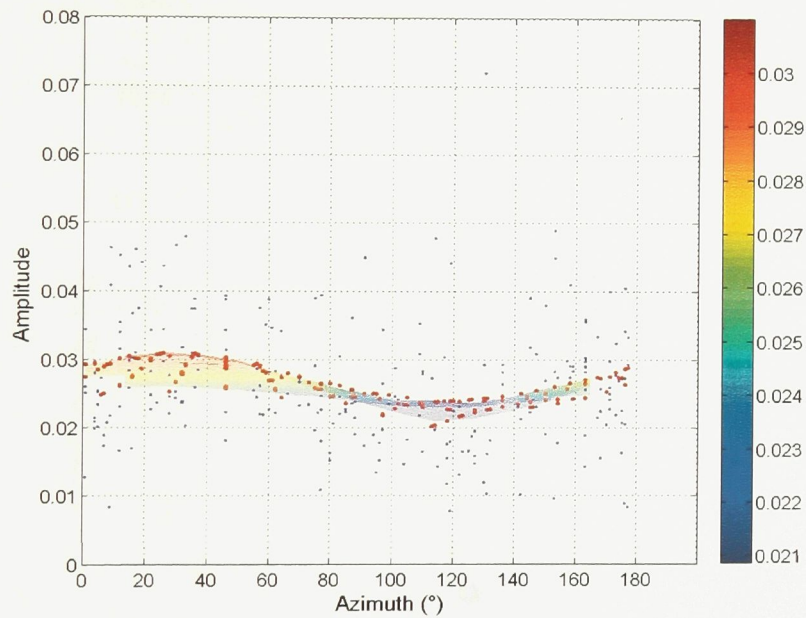
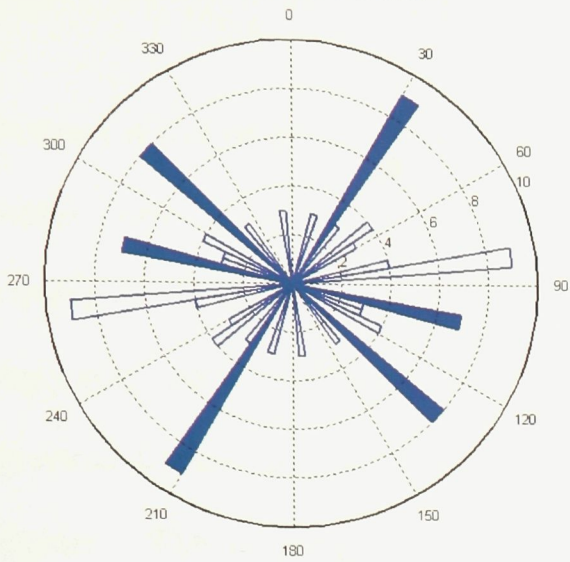


Figure 6.15. AVOA surface displayed in the amplitude – azimuth plane. Color shading corresponds to amplitude value. A strong azimuthal anisotropy is observed for the 'G' anomaly, Figure 6.9. Red dots represent the AVOA surface fit to the data (blue dots).

a) Bunge, 2000 Oriented core results



b) This study, AVOA anisotropy orientations

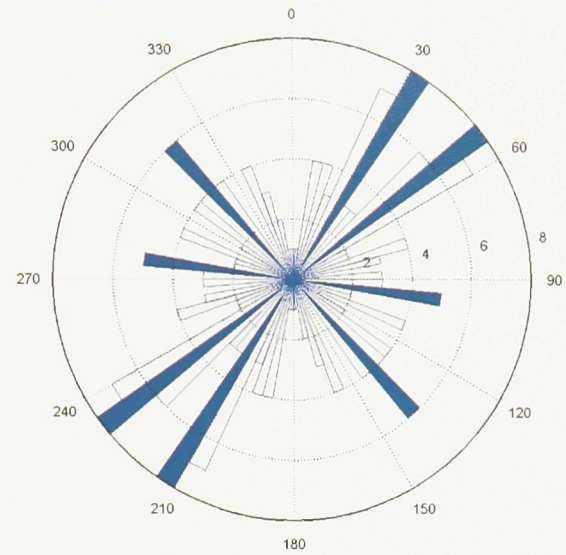


Figure 6.16. Comparison between a) Bunge, 2000 oriented core fracture orientations and b) AVOA inversion orientation of anisotropy. Bunge, 2000 notes that in a) open fracture directions are roughly  $30^\circ$ ,  $315^\circ$  and  $285^\circ$  while the healed fracture directions are  $80^\circ$ . AVOA inversion appears to be sensitive to similar open fracture orientations.

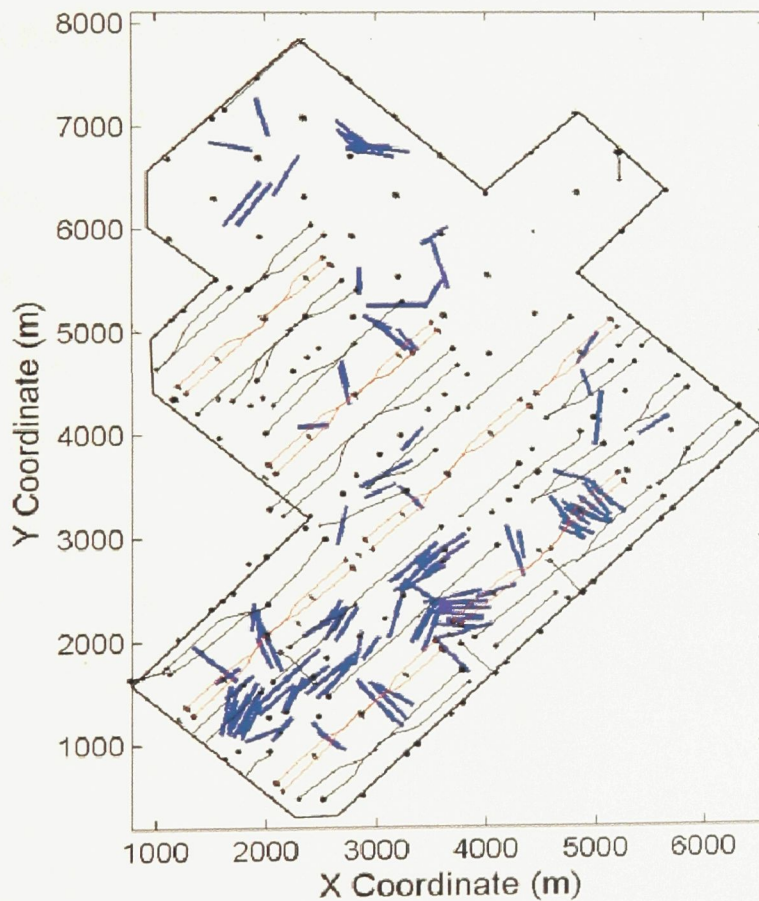


Figure 6.17. Anisotropy vectors with well trajectories overlain. Horizontal producers, black, horizontal injectors, red and anisotropy magnitude and orientations are shown as blue vectors.

## Chapter 7. Conclusion

---

Fracture detection through AVOA inversion has been successfully demonstrated for two sealing units of interest; the Watrous Member and underlying cap rock interval. Confidence in the inversion results is developed through methodical processing of the input data, robust assessment of the individual anomalies, modeling and comparison with previous fracture studies. Great care was taken to produce an accurate true amplitude dataset. The imaging stack was successfully reproduced using surface consistent processes and without spectral whitening.

Confidence in the azimuthal AVO inversion is gained through observing an absence of the acquisition geometry in the anisotropy maps, spatially consistent orientations and differences between horizons. These features indicate that any potential acquisition artifacts, such as source-receiver coupling issues, were adequately handled in the processing. Synthetics studies show that the 2001 3D survey geometry will not bias the orientation of anisotropy due to gaps in the azimuth or offset coverage and will correctly identify azimuthal variations in the presence of noise. Anisotropy maps of the cap rock and Watrous horizons display a clear difference in magnitude, orientation and distribution of anomalies. These results satisfy the constraints on successful azimuthal AVO inversion.

Generally, uncertainties are higher and model correlation is lower for the cap rock when compared with the Watrous. This is attributed to the reduced thickness and increased stratigraphic complexity of the combined cap rock interval. Modeling has shown that reflection amplitudes will not follow the simplified HTI model in the presence of multiple thin (<20m) anisotropic layers. The northern region of the study area is below 20m in thickness and shows unacceptable levels of uncertainty. Modeling has also shown that with decreasing cap rock interval thickness, higher levels of anisotropy from the underlying reservoir are observed. However, for layer thickness in excess of 20m, the magnitude of anisotropy of an anisotropic cap rock is more than double that of the isotropic case. This suggests that anisotropy in the cap rock will appear as magnitude anomalies and may be detected. The level of uncertainty in the magnitude of anisotropy does not allow for differentiation between gas and brine crack fill material.

The cap rock and Watrous horizon show significantly different anisotropy patterns. Two residual anomalies occur along the southern edge of the survey area at the Watrous horizon. The anisotropy shows a good fit to the vertical fracture model and corresponds to salt dissolution structures in the Watrous and overlying Lower Gravelbourg horizons. The cap rock horizon shows three significant residual anomalies. Two of the anomalies correspond to salt dissolution structures in the cap rock and overlying horizons. The third anomaly does not correspond with any significant features on the seismic image. The cap rock anisotropy anomalies show a good fit to the vertical fracture model and correlate well with previous fracture studies using well logs and core samples. Microseismic monitoring has detected events above the reservoir over the production wells.

Geomechanical modeling shows that stress transfer into the overburden is most likely to occur over production wells causing north east anisotropy orientations (Verdon, et al., 2010). AVOA inversion results correlate well with these geomechanical modeling predictions and microseismic observations. Anisotropy anomalies may be the result of salt dissolution related fracturing being reactivated by production activities. The majority of anomalies are located between injection wells and on trend with the production wells with a consistent north east orientation. The inferred fracture orientations are also sub-parallel to regional direction of maximum horizontal stress, which is north east.

Anisotropy observed at the cap rock and Watrous horizon may result from a combination of many sources. Seismic anisotropy analysis has detected multiple isolated areas of increased anisotropy which may be fracture related. Geochemical monitoring and core samples above the reservoir do not indicate an upward migration of CO<sub>2</sub> or reservoir fluids. Time lapse seismic techniques, such as amplitude and travel time difference maps, have successfully imaged CO<sub>2</sub> accumulations at the injection wells within the reservoir (White, 2009). These techniques should be used to monitor overlying layers for potential accumulations of CO<sub>2</sub> or other reservoir fluids.

## Chapter 8. References

---

- Aki, K. and Richards, P.G., 1980, *Quantitative seismology: theory and methods*, Freeman
- Al-Marzoug, A.M., F.A. Neves, J.J. Kim, E.L. Nebrija, 2006, P-wave anisotropy from azimuthal AVO and velocity estimates using 3D seismic data from Saudi Arabia, *Geophysics*, vol. 71, no. 2, E7-E11
- Al-Shuhail, A.A., 2007, Fracture-porosity inversion from P-wave AVOA data along 2D seismic lines: An example from the Austin Chalk of southeast Texas, *Geophysics*, vol. 72, no. 1, B1-B7
- Bakulin, A., V. Grechka, I. Tsvankin, 2000, Estimation of fracture parameters from reflection seismic data-Part I: HTI model due to a single fracture set, *Geophysics*, vol. 65, no. 6, November-December
- Bakulin, A., V. Grechka, I. Tsvankin, 1999, Estimation of fracture parameters of HTI media from surface P and PS data, *SEG Expanded Abstracts*
- Brown, L.T., 2002, Integration of rock physics and reservoir simulation for the interpretation of time-lapse seismic data at Weyburn field, Saskatchewan, *Colorado School of Mines*, M.Sc. Thesis
- Bunge, R.J., 2000, Midale reservoir fracture characterization using integrated well and seismic data, Weyburn field, Saskatchewan, *Colorado School of Mines*, M.Sc. Thesis
- Burrowes, O.G., 2001, Investigating CO<sub>2</sub> storage potential of carbonate rocks during tertiary recovery from a billion barrel oil field, Weyburn Saskatchewan: Part 2 – reservoir geology (IEA Weyburn CO<sub>2</sub> Monitoring and Storage Project): In: *Summary of Investigations 2004, Volume 1*, Saskatchewan Geological Survey Sask. Industry Resources, Misc. Rep. 2004-4.1
- Castagna, J.P., H.W. Swan, D.J. Foster, 1998, Framework for AVO gradient and intercept interpretation, *Geophysics*, vol. 63, no. 3, May-June, 1998
- Chapman, C.H., 1976, Exact and approximate generalized ray theory in vertically inhomogeneous media, *Geophysical Journal of the Royal Astronomical Society.*, 46, 201-233
- Chen, W., 1995, AVO in azimuthally anisotropic media fracture detection using P-wave data and a seismic study of naturally fractured tight gas reservoirs, *Ph.D. thesis, Stanford University*

- Cheng, C.H., 1993, Crack models for a transversely isotropic medium, *Journal of Geophysical Research*, vol. 98, no. B1, 675-684
- Chung, H.M., D.C. Lawton, 1995, Amplitude responses of thin beds: Sinusoidal approximation versus Ricker approximation, *Geophysics*, vol. 63, no. 1, January-February
- Crampin, S., 1978, Seismic wave propagation through a cracked solid: Polarization as a possible dilatancy diagnostic, *Geophysical Journal of the Royal Astronomical Society*, 53, 467-496
- Crampin, S., 1981, A review of wave motion in an anisotropic and cracked elastic media, *Wave Motion*, 3, 343-391
- Crampin, S., 1984, Effective anisotropic elastic constants for wave propagation through cracked solids, *Geophysical Journal of the Royal Astronomical Society*, 76, 135-145
- Crampin, S., 1987, Shear-wave polarizations: A plea for three-component recording, in S. Danbom and S. Domenico, eds., Shear wave exploration, *Society of Exploration Geophysicists, Geophysical Developments 1*, 227-251.
- Fischer, B.F., 1994, Fracture analysis: Midale Field, SE Saskatchewan: Shell Canada Limited, October, 1994
- Gray, D., G. Roberts, K. Head, 2002, Recent advances in determination of fracture strike and crack density from P-wave seismic data, *The Leading Edge*, 280-285, March
- Grechka, V., I. Tsvankin, 1999, 3-D moveout velocity analysis and parameter estimation for orthorhombic media, *Geophysics*, vol.64, no.3, 820-837
- Grechka, V., I. Tsvankin, 2000, Inversion of azimuthally dependent NMO velocity in transversely isotropic media with tilted axis of symmetry, *Geophysics*, vol. 65, no.1. 232-246
- Grechka, V., A. Bakulin, I. Tsvankin, 2003, Seismic characterization of vertical fractures described as general linear-slip interfaces, *Geophysical Prospecting*, 51, 117-129
- Guest, W.S., and Kendall, J-M., 1993, Modelling seismic waveforms in anisotropic inhomogeneous media using ray and maslov asymptotic theory: Applications to exploration seismology. In Lawton, D. C., editor, 5<sup>th</sup> *Int. Worksh. On Seismic Anisotropy*, Volume 29, pages 78-92. J. Can. Soc. Exploration Geophysicists
- Gupta, I. N., 1973a, Dilatancy and premonitory variations of P, S travel times, *Bulletin of the Seismological Society of America*, 63, 1157-1161

- Gupta, I. N., 1973b, Premonitory variations in S-wave velocity anisotropy before earthquakes in Nevada, *Science*, 182, 1129-1132
- Gupta, I. N., 1974, Premonitory seismic wave phenomena before earthquakes in Nevada, *Earth and Ocean Science*, Transactions of the American Geophysical Union, 55, 355
- Hall, S.A., and Kendall, J-M., 1997, Converted phase AVOA effects over multiple fracture sets: Application to ocean bottom surveys., In 67<sup>th</sup> *Annual International Meetings, Society of Exploration Geophysicists*, Expanded abstracts, 1195-1198
- Hall, S.A., 2000a, Rock fracture characterisation and seismic anisotropy: application to ocean bottom seismic data, *University of Leeds*, Ph.D. Thesis.
- Hall, S.A., J-M. Kendall, 2000b, Constraining the interpretation of AVOA for fracture characterisation, in *Anisotropy 2000: Fractures, converted waves and case studies, Society of Exploration Geophysicists*
- Hall, S. A., J.M. Kendall, 2003, Fracture characterization at Valhall: Application of P-wave amplitude variation with offset and azimuth (AVOA) analysis to a 3D ocean-bottom data set, *Geophysics*, vol. 68, no. 4, July-August
- Harwood, S., P.S. Rowbotham, I. Bush, P.R. Williamson, H. Houllevigue, J.M. Kendall, 1998, Uncertainties in the analysis of AVOA for determination of fracture orientation, *Revue de L'institute Francais, du Petrole*, vol. 53, no. 5, September-October, 1998
- Helbig, K., L. Thomsen, 2005, 75-plus years of anisotropy in exploration and reservoir seismics: A historical review of concepts and methods, *Geophysics*, vol. 70, no. 6, November-December, 2005
- Hudson, J.A., 1980, Attenuation of elastic waves in a cracked, fluid-saturated solid, *Cambridge Philosophical Society*, 88, 547
- Hudson, J.A., 1980, Overall properties of a cracked solid, *Cambridge Philosophical Society*, 88, 371-384
- Hudson, J.A., 1981, Wave speeds and attenuation of elastic waves in material containing cracks, *Geophysical Journal of the Royal Astronomical Society*, 64, 133-150
- Hudson, J.A., 1986, A higher order approximation to the wave propagation constants for a cracked solid, *Geophysical Journal of the Royal Astronomical Society*, 87, 265-274
- Jenner, E., 2002, Azimuthal AVO: Methodology and data examples, *The Leading Edge*, August

- Jenner, E., 2001, Azimuthal anisotropy of 3-D compressional wave seismic data, Weyburn field, Saskatchewan, Canada, *Colorado School of Mines*, Ph.D. Thesis
- Kent, D.M., P.L. Thomas, and T. Heck, 2004, Geological mapping of Mississippian strata in southeastern Saskatchewan, northwestern North Dakota and northeastern Montana (IEA Weyburn CO<sub>2</sub> Monitoring and Storage Project): In: *Summary of Investigations 2004, Volume 1*, Saskatchewan Geological Survey Sask. Industry Resources, Misc. Rep. 2004-4.1
- Lefeuvre, F., 1994, Fracture related anisotropy detection and analysis: And if the P-waves were enough?":64<sup>th</sup> Annual Meeting, *Society of Exploration Geophysicists*, Expanded Abstracts, 942-944.
- Luo, M. B.J. Evans, 2004, An amplitude-based multi-azimuth approach to mapping fracture using P-wave 3D seismic data, *Geophysics*, vol. 69, no. 3, May-June, 2004
- Lynn, H., Simon, K.M., Layman, M., Schneider, R., Bates, C. R., and Jones, M., 1995, Use of anisotropy in P-wave and S-wave data for fracture characterization in a naturally fractured gas reservoir, *The Leading Edge*, 15, 923-928.
- Mallick, S., and Frazer, L. N., 1991, Reflection/transmission coefficients and azimuthal anisotropy in marine seismic studies, *Geophysical Journal International*, 105, 241-252
- Mallick, S., Craft, K.L., Meister, L.J., and Chambers, R.E., 1998, Determination of the principal directions of azimuthal anisotropy from P-wave seismic data, *Geophysics*, 63, 692-706
- Maultzsch, S. Horne, S. Archer, H. Burkhardt, 2003, Effects of an anisotropic overburden on azimuthal amplitude analysis in horizontal transverse isotropic media, *Geophysical Prospecting*, 51, 61-74, 2003.
- Minsley, B.J., M. E. Willis, M. Krasovec, D.R. Burns, and M.N. Toksöz, 2004, Fracture detection using amplitude versus offset and azimuth analysis of a 3D P-wave seismic dataset and synthetic examples, *Massachusetts Institute of Technology*, Earth Resources Laboratory, May
- Nickel, E., and H. Qing, 2004, Geochemical and petrographic characterization of the unconformity-related seal in the Weyburn Midale Pool, southeastern Saskatchewan; In: *Summary of Investigations 2004, Volume 1*, Saskatchewan Geological Survey Sask. Industry Resources, Misc. Rep. 2004-4.1

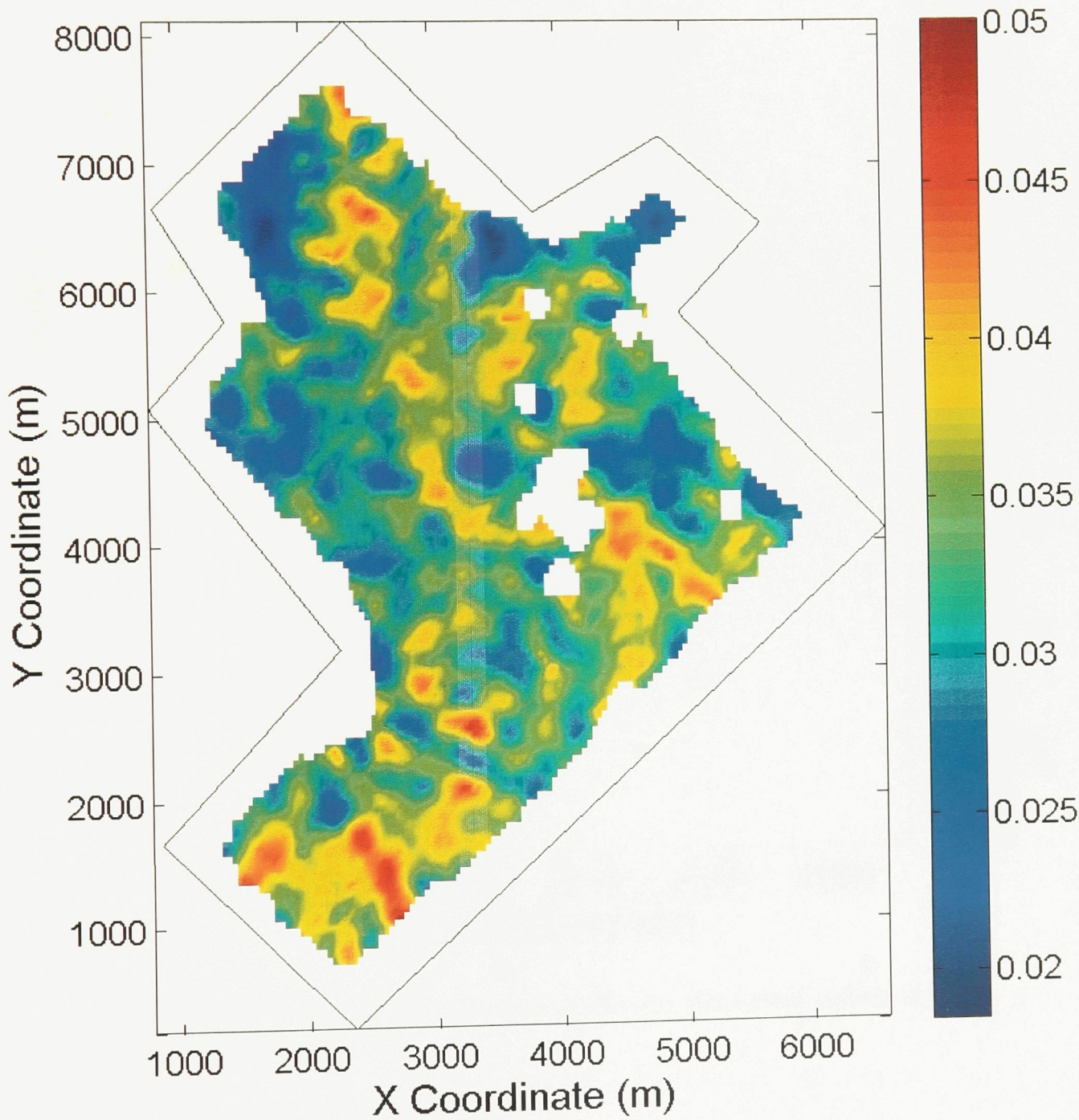
- Pendrigh, N.M., 2005, Geological and geophysical characterization of the Mississippian Midale reservoir, Weyburn Field, Saskatchewan; in Summary of Investigations 2005, Volume 1, Saskatchewan Geological Survey, Sask. Industry Resources, Misc. Rep. 2005-4.1
- Pérez, M.A., R.L. Gibson, M.N. Toksöz, 1999, Detection of fracture orientation using azimuthal variation of P-wave AVO responses, *Geophysics*, vol. 64, no. 4, July-August
- Qing, H., 2004, Isotopic geochemistry of anhydrites from Midale, Frobisher and Watrous strata: implications for communication of Mississippian reservoirs with Watrous Formation. Internal report, IEA GHG Weyburn CO<sub>2</sub> Monitoring and Storage Project, 5p.
- Raymen, D.G., A. Tommas, J.M. Kendall, 2000, Predicting the seismic implications of salt anisotropy using numerical simulations of halite deformation, *Geophysics*, vol. 65, no. 4, July-August
- Rüger, A., and Tsvankin, I., 1995, Azimuthal variation of AVO response for fractured reservoirs: 65<sup>th</sup> Ann. International Meeting, *Society of Exploration Geophysicists*, Expanded Abstracts, 1103-1106.
- Rüger, A., 1997, P-wave reflection coefficients for transversely isotropic models with vertical and horizontal axis of symmetry, *Geophysics*, vol. 62, no. 3
- Rüger, A., I. Tsvankin, 1997, Using AVO for fracture detection: Analytic basis and practical solutions, *The Leading Edge*, October
- Rüger, A., 1998, Variation of P-wave reflectivity with offset and azimuth in anisotropic media, *Geophysics*, vol. 63, no. 3, May-June
- Rüger, A., 2002, Reflection coefficients and azimuthal AVO analysis in anisotropic media, *Society of Exploration Geophysicist - Geophysical Monograph Series*, no.10
- Rutherford, S.R., R.H. Williams, 1989, Amplitude-versus-offset variations in gas sands, *Geophysics*, vol. 54, no. 6, June
- Sabinin, V., T. Chichinina, 2008, AVOA technique for fracture characterization: resolving ambiguity, *Geofisica Internacional*, vol. 47, no. 1
- Sayers, C. M., and Rickett, J.E., 1997, Azimuthal variation in AVO response from fractured gas sands, *Geophysical Prospecting*, 45, 165-182

- Sayers, C.M., 1998, Misalignment of the orientation of fractures and the principal axes for P and S waves in rocks containing multiple non-orthogonal fracture sets, *Geophysical Journal International*, 133, 459-466
- Schoenberg, M., F. Muir, 1989, A calculus for finely layered anisotropic media, *Geophysics*, vol 54, no 5
- Schoenberg, M., C.M. Sayers, 1995, Seismic anisotropy of fractured rock, *Geophysics*, vol 60, no.1, 204-211
- Sen, M.K., F.D. Lane, 2007, Anomalous reflection amplitudes from fractured reservoirs – failure of AVOA, *The Leading Edge*, September
- Sheriff, R.E., L.P. Geldart, 1995, Exploration seismology 2<sup>nd</sup> ed., *Cambridge University Press*
- Shuey, R.T., 1985, A simplification of the Zoeppritz equations, *Geophysics*, vol. 50, no. 4, 609-614
- Sinha, S., and R. Ramkhelawan, 2008, P-wave azimuthal anisotropy from a full-wave seismic field trial in Wamsutter, Annual International Meeting, *Society of Exploration Geophysicists*, Expanded Abstracts
- Soroka, W.L., T.J. Fitch, K.H.V. Sickle, P.D. North., 2002, Successful production application of 3-D amplitude variation with offset: The lessons learned, *Geophysics*, vol. 67, no. 2, March-April
- Strahilevitz, R., and Gardner, G. H. F., 1995, Fracture detection using P-wave AVO: 65<sup>th</sup> Annual International Meeting, *Society of exploration Geophysicists*, Expanded Abstracts, 723-724.
- Sun, Z., R.J. Brown, D.C. Lawton, 1991, Seismic anisotropy and salt detection: A physical modelling study, *CREWES*, Research Reports, 32
- Thomsen, L., 1986, Weak elastic anisotropy, *Geophysics*, vol. 51, no. 10. 1954-1966
- Tsvankin, I., ,1997, Anisotropic parameters and P-wave velocity for orthorhombic media, *Geophysics*, vol. 62, no. 4, July-August
- Verdon, J.V., J-M. Kendall, D.J. White, D.A. Angus, 2010, Linking microseismic event observations with geomechanical models to minimise the risks of storing CO<sub>2</sub> in geological formations, *EPSL* ,July, in review.
- Ursenbach, C.P., R.R. Stewart, 2008, Two-term AVO inversion: Equivalences and new methods, *Geophysics*, vol. 73, no. 6, November-December

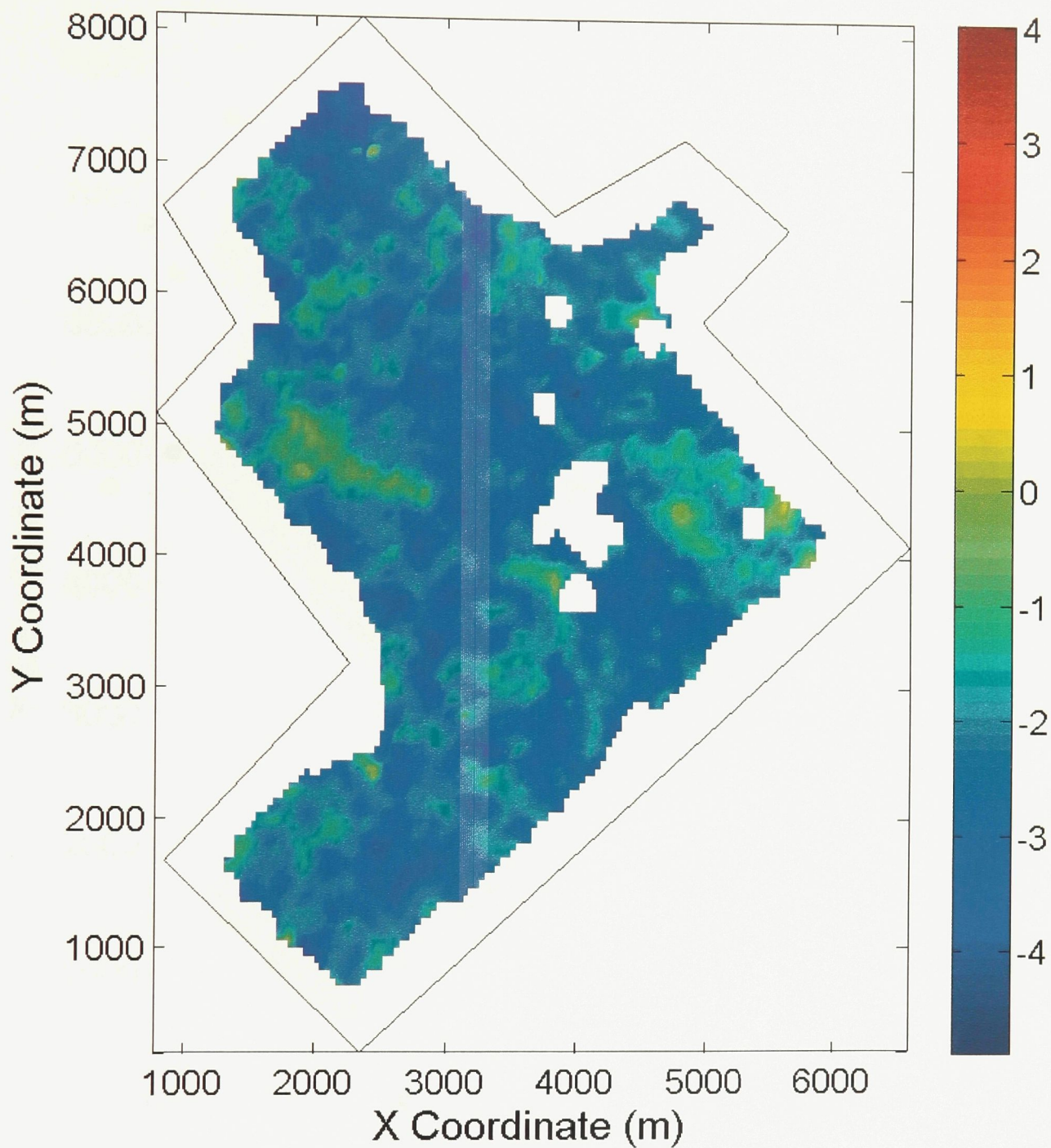
- White, D.J., G. Burrowes, T. Davis, Z. Hajnal, K. Hirsche, I. Hutcheon, E. Majer, B. Rostron and S. Whittaker, 2004, Greenhouse gas sequestration in abandoned oil reservoirs: The International Energy Agency Weyburn pilot project, *GSA Today*, 14, 4-10.
- White, D.J., 2009, Monitoring CO<sub>2</sub> storage during EOR at the Weyburn-Midale Field, *The Leading Edge*, 838-842, July
- Whittaker, S., D. White, D. Law, R. Chalaturnyk, 2004, IEA GHG Weybrn CO<sub>2</sub> monitoring and storage project, summary report, 2000-2004, Eds. M. Wilson, M. Monea, *Petroleum Technology Research Center*
- Xu, X., I. Tsvankin, 2006, A case study of azimuthal AVO analysis with anisotropic spreading correction, *The Leading Edge*, December
- Yilmaz, Ö., 2001, *Seismic data analysis: processing, inversion, and interpretation of seismic data*, Society of Exploration Geophysicists, Investigations in Geophysics

## Appendix A

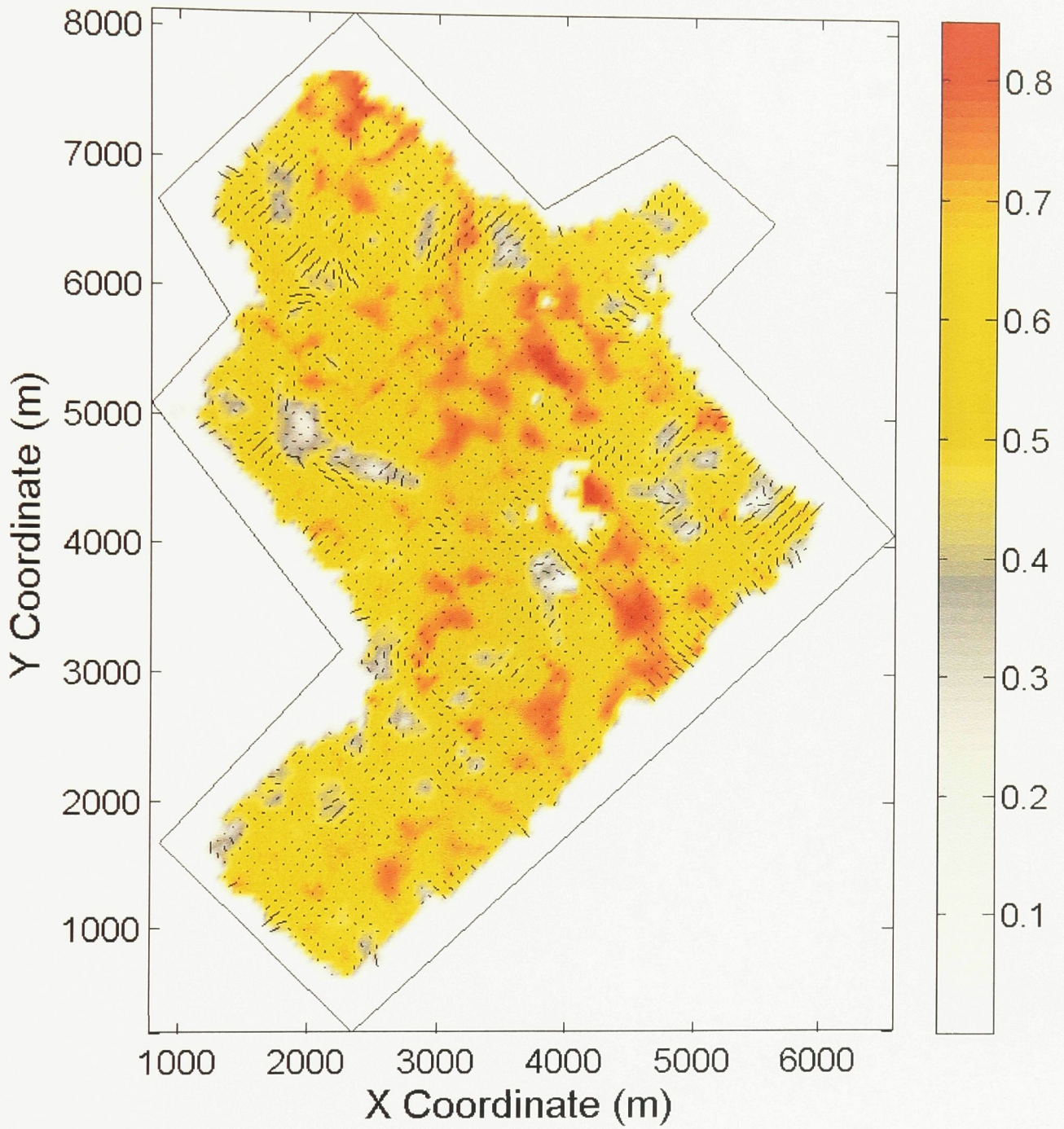
Horizon attribute maps from AVOA surface fitting inversion.



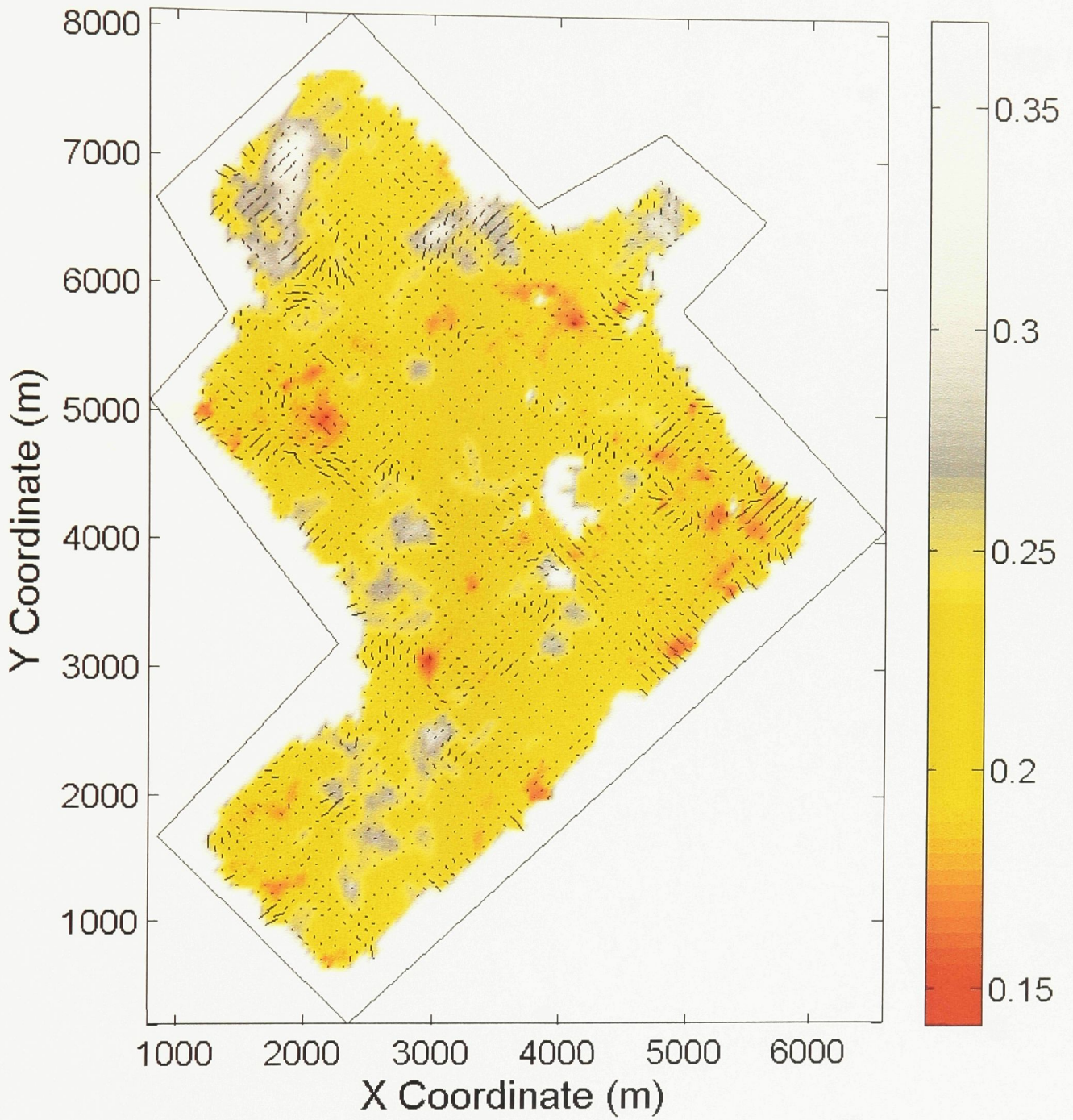
Watrous horizon zero-offset reflection amplitude map.



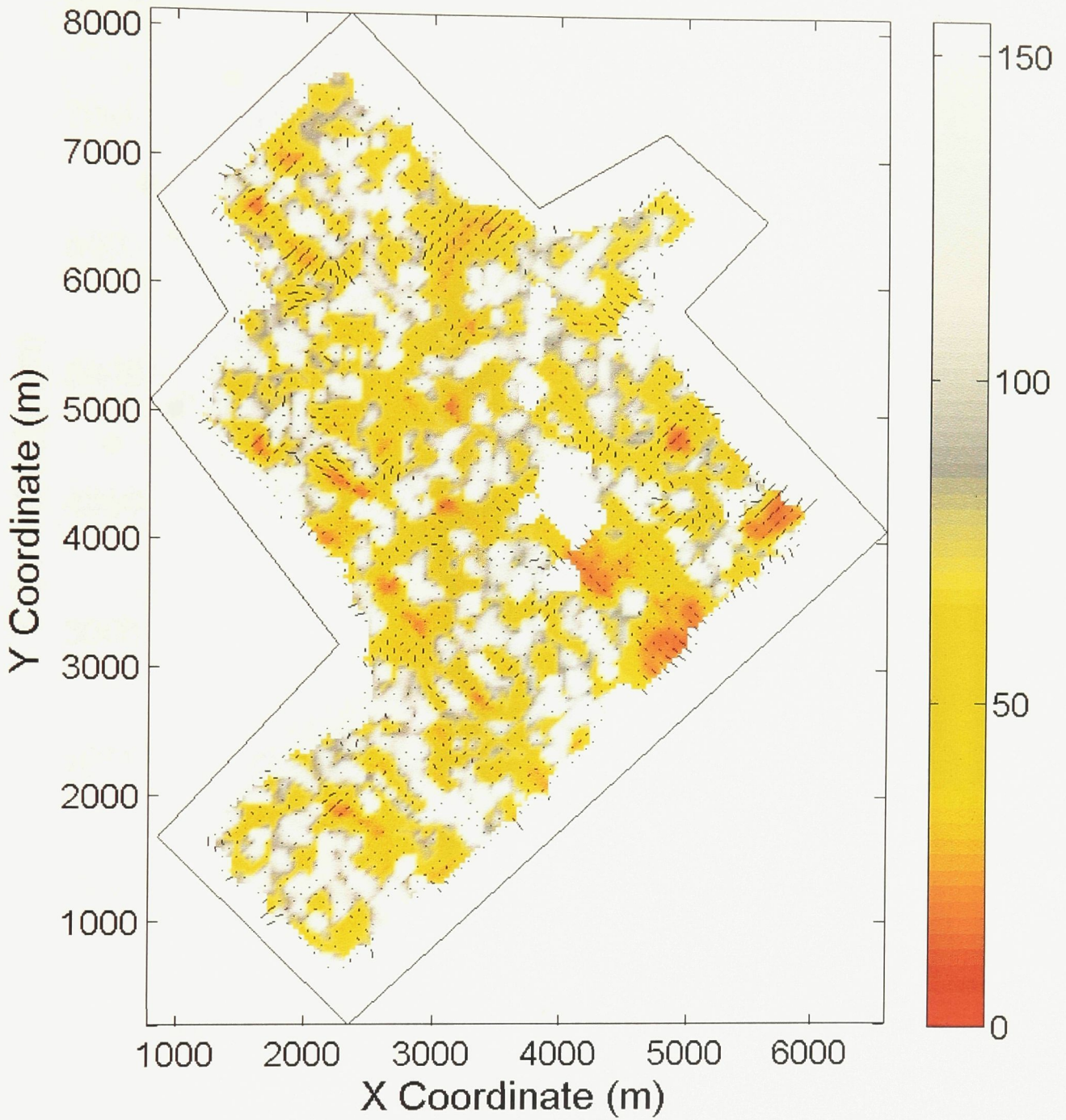
Watrous horizon AVO gradient normalized by zero-offset reflection amplitude map.



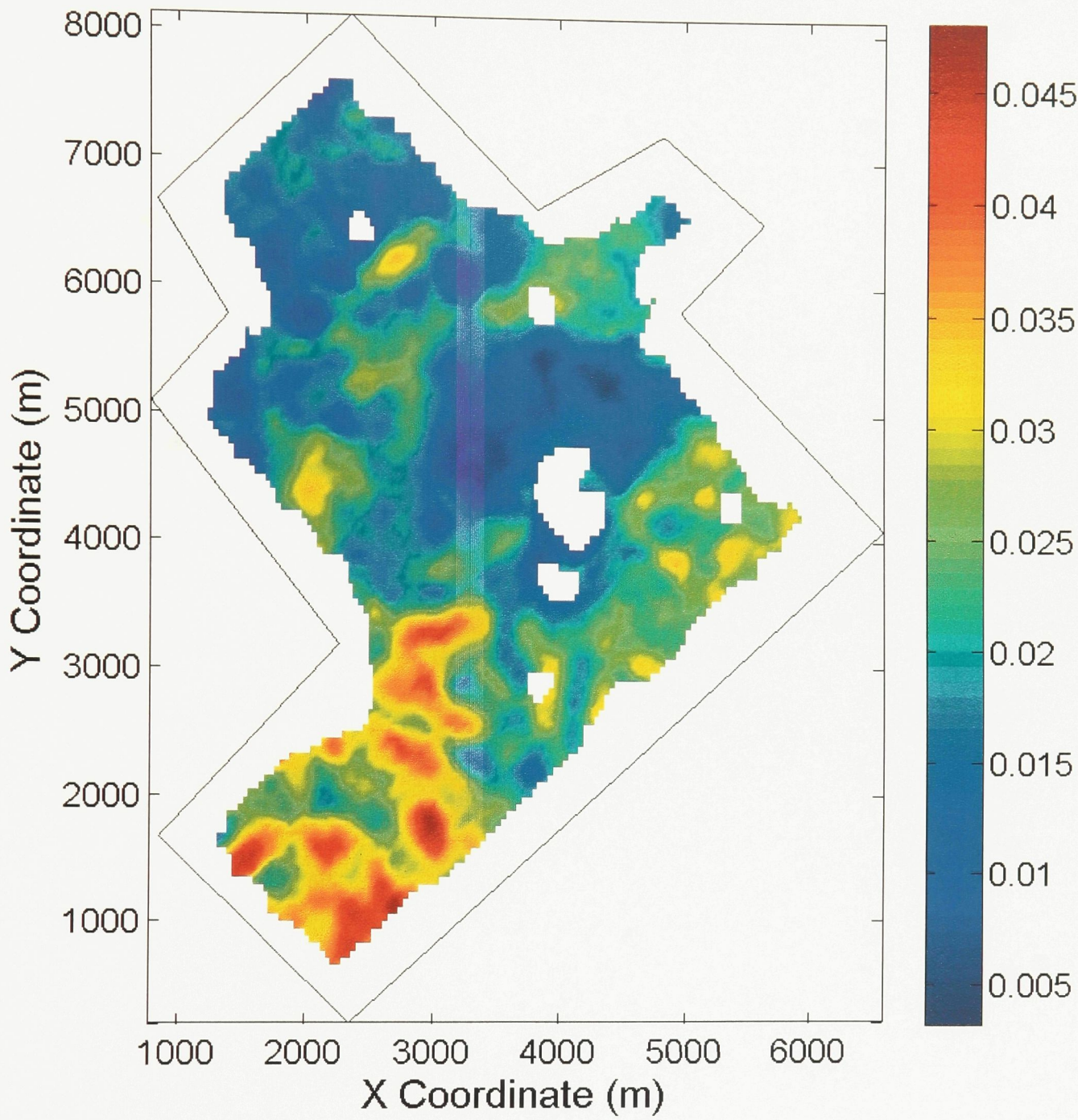
Watrous horizon HTI model correlation map.



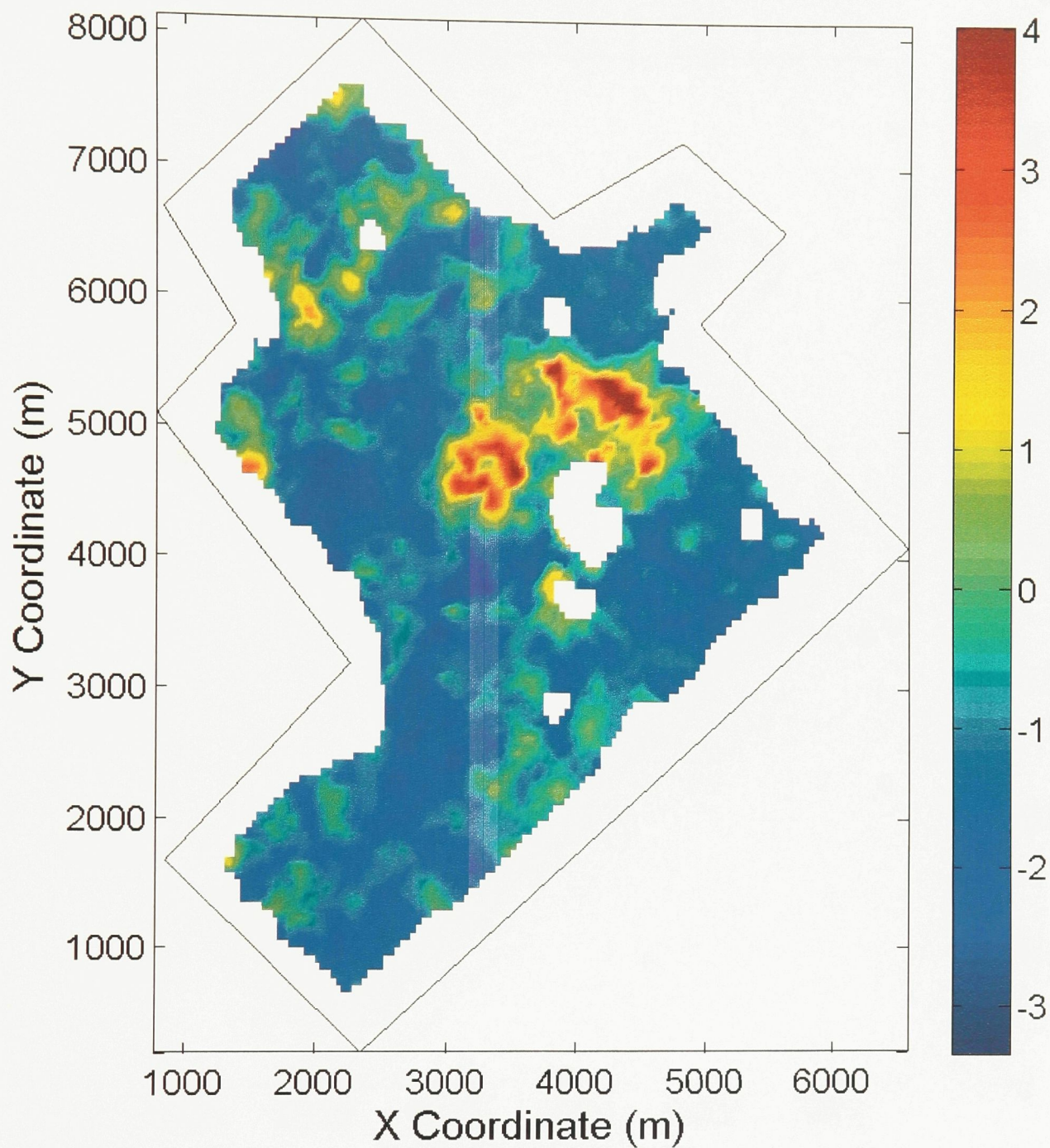
Watrous horizon normalized RMS difference.



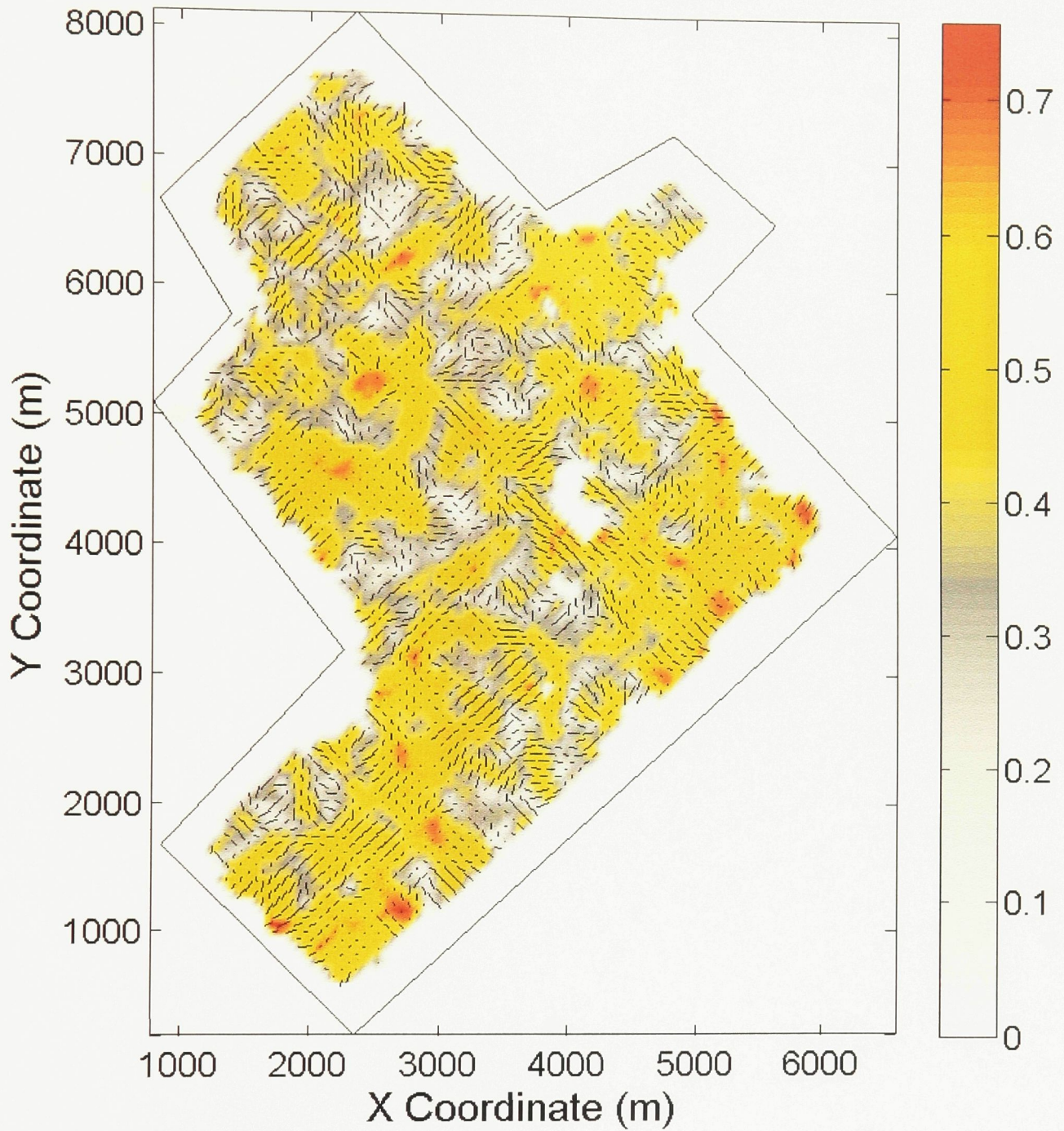
Watrous horizon % uncertainty in magnitude of anisotropy.



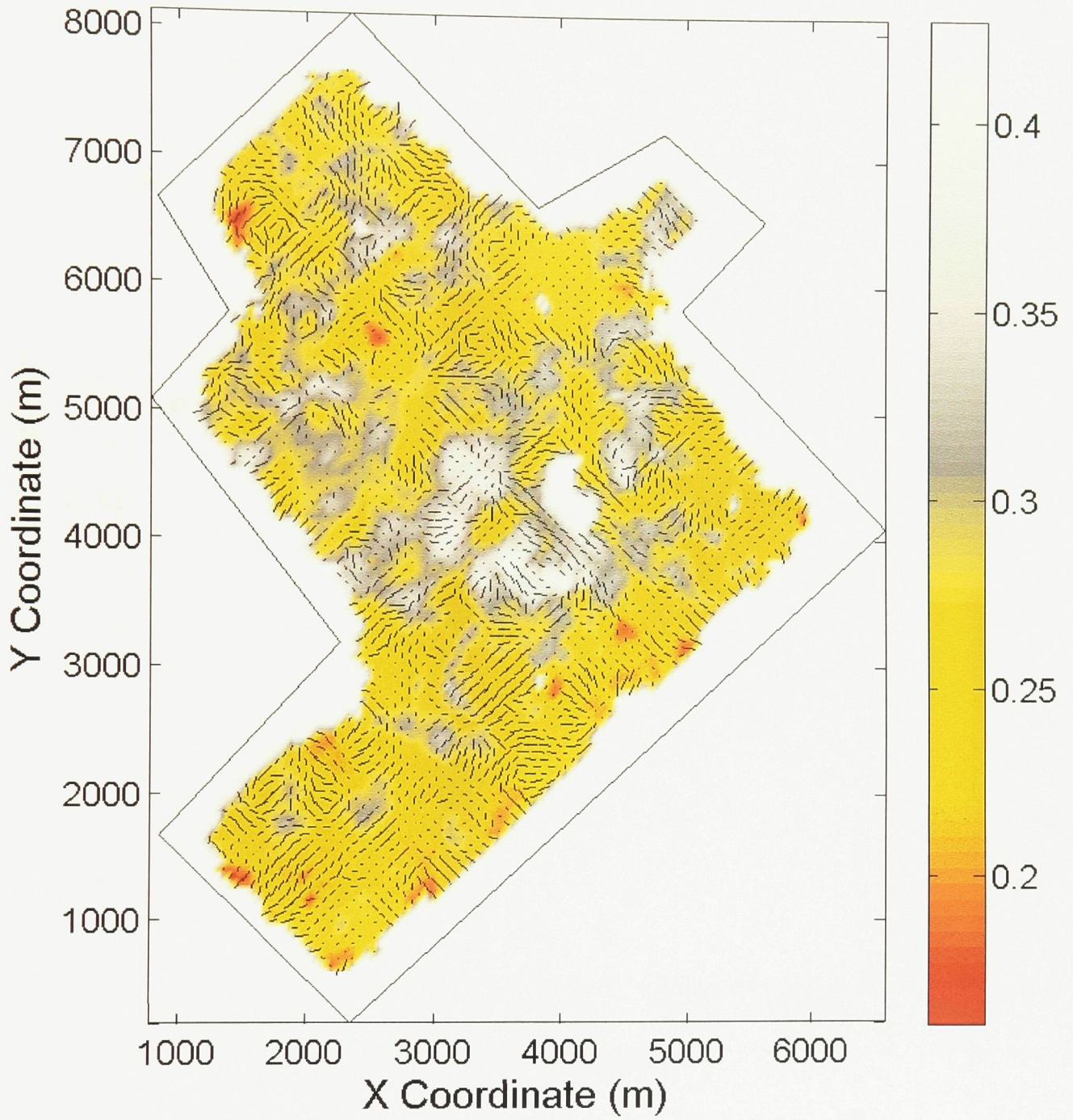
Cap rock horizon zero-offset reflection amplitude map.



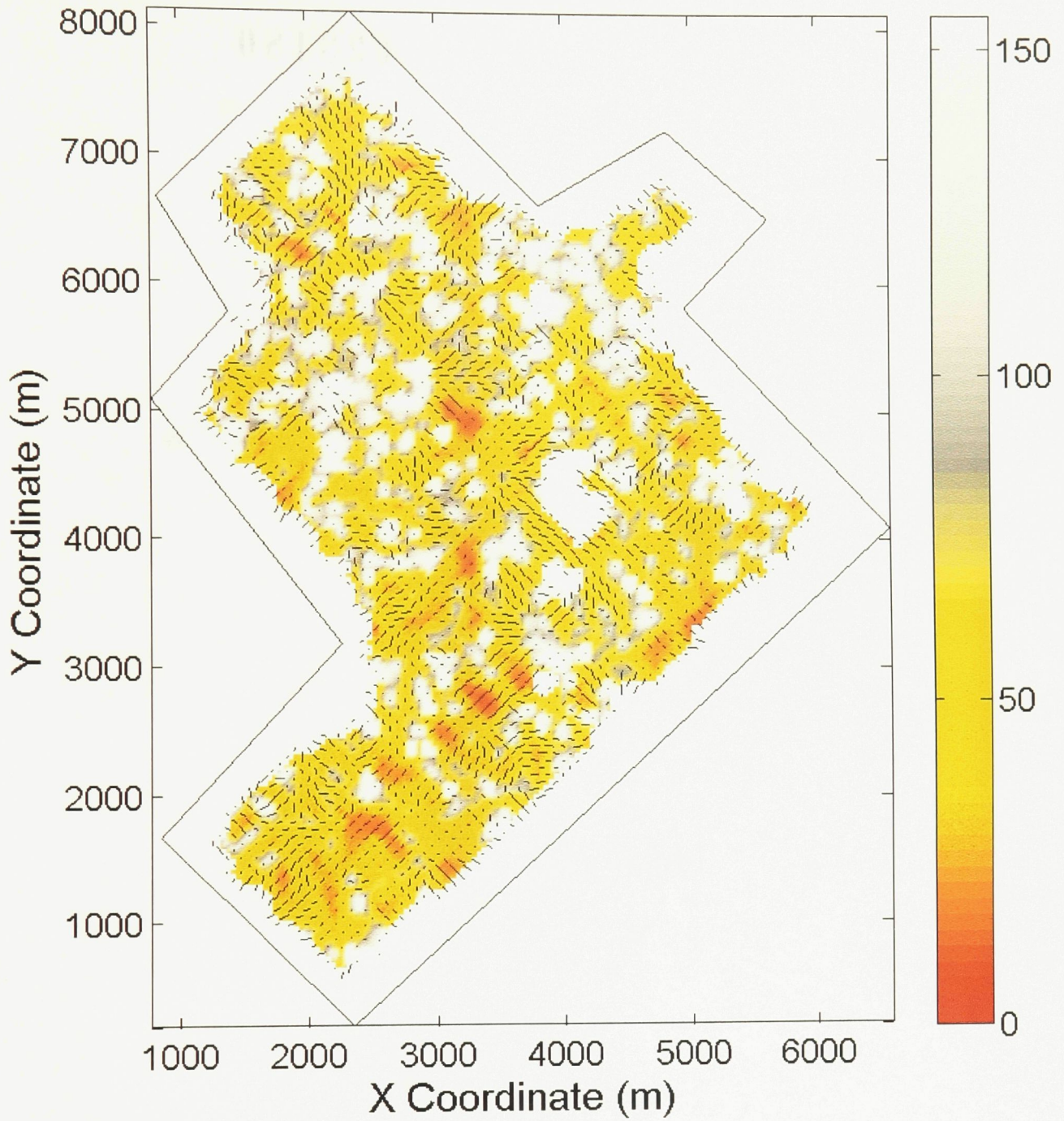
Cap rock horizon AVO gradient normalized by zero-offset reflection amplitude map.



Cap rock horizon HTI model correlation map.



Cap rock horizon normalized RMS difference map.



Cap rock horizon % uncertainty in magnitude of anisotropy.